Università degli Studi di Padova

DIPARTIMENTO DI FISICA E ASTRONOMIA GALILEO GALILEI
Corso di Laurea Magistrale in Astronomia

Tesi di laurea magistrale

Physics and Kinematics of the Extended Narrow Line Region of Three AGN

Laureando
Enrico Congiu

Relatore
Dott. Stefano Ciroi

Correlatore
Dott.ssa Valentina Cracco

Anno Accademico 2014/2015

Abstract

Active Galactic Nuclei (AGN) are among the most luminous objects of the whole universe and they have been intensively studied, in the last decades, because they are characterized by many interesting astrophysical phenomena. One of their most extended and puzzling structures is the *Extended Narrow Line Region* (ENLR), a region made of highly ionized gas, which is present up to distances of about some kiloparsecs from the galactic nucleus. When this structure shows a conical or bi-conical shape, with the apex of each cone pointing to the active nucleus, it is called *ionization cone*. The ionization cones are an essential proof of the Unified Model which was presented for the first time by Antonucci (1993). This model predicts that the ionizing radiation, produced by the active nucleus, is emitted anisotropically because of the presence of a dusty torus which surrounds the nucleus itself and allows the photons to exit only around its axis direction. There are some questions, that have not been answered yet about the ENLR and, above all, about the gas origin. The hypothesis are various: the gas could be part of the galaxy interstellar medium (ISM) which is ionized by the AGN emission, a second hypothesis is that the gas could be expelled by the nucleus itself thanks to the jets, otherwise it could have fallen inside the galaxy because of gravitational interactions with other galaxies.

The main purpose of this work is to analyse the physical and kinematic properties of the ENLR gas in three nearby AGN, by using medium resolution echelle spectra in order to resolve the gas emission at different velocities. Another aim of the study is to verify if the method applied here can be adopted, in an efficient way, also in a larger sample. The chosen objects for this work are three Seyfert 2 galaxies: IC5063, NGC5643 and NGC7212. They have different morphological type: IC5063 is a lenticular galaxy, NGC5643 is a spiral galaxy and NGC7212 is a spiral galaxy in strong interaction with other two similar objects. However, they were selected for our study because in each galaxy was observed an ENLR (Colina, Sparks, and Macchetto 1991, Morris et al. 1985, Schmitt et al. 2003).

In chapter 1, I will describe the Unified Model and the ionization cones, including the actual theories about the ENLR gas origin. Then, in chapter 2, I will describe the sample, the instrument used to acquire the data and the observations. In this chapter, I will also describe the data reduction process. The next chapter will include all of those post-reduction passages I did before the data analysis, which I will present in chapter 4. Finally, in chapter 5 the results I obtained for each galaxy will be discussed, while in the last chapter I will show the final conclusions.

Abstract

I *nuclei galattici attivi* (AGN) sono alcuni tra gli oggetti più luminosi dell'universo e sono stati studiati intensamente, negli ultimi decenni, perché sono caratterizzati da molti fenomeni astrofisici interessanti. Una delle strutture più estese di questi oggetti è la cosiddetta *extended narrow line region* (ENLR), una regione di gas altamente ionizzato che si estende fino a distanze dell'ordine dei kiloparsec dal nucleo della galassia. In alcuni casi questa struttura assume una formula conica o bi-conica, con l'apice di ciascun cono che punta verso il nucleo attivo, e viene chiamata *cono di ionizzazione*. I coni di ionizzazione sono una fondamentale conferma del Modello Unificato presentato per la prima volta in Antonucci (1993). Questo modello prevede che la radiazione ionizzante, prodotta dal nucleo attivo, venga emessa in maniera anisotropa a causa della presenza di un toro di polveri che circonda il nucleo stesso e permette la fuoriuscita dei fotoni solo lungo la direzione definita dal suo asse. Ci sono diverse questioni che non sono state ancora risolte riguardo all'ENLR, una tra tutte l'origine del gas. Le ipotesi sono diverse: il gas potrebbe essere parte del mezzo interstellare (ISM) della galassia che viene ionizzato dalla radiazione emessa dall'AGN, oppure potrebbe provenire dall'interno del nucleo attivo ed essere espulso attraverso i jet, una terza ipotesi è che il gas sia giunto all'interno della galassia attiva in seguito a interazioni gravitazionali con altri oggetti.

L'obiettivo principale di questo lavoro è di analizzare le proprietà fisiche e cinematiche del gas dell'ENLR in tre AGN vicini, utilizzando degli spettri echelle a media risoluzione in modo da risolvere l'emissione del gas a diverse velocità. Un altro obiettivo sarà verificare se il metodo utilizzato per l'analisi può essere applicato, in modo efficace, ad una ampio campione di oggetti. Le galassie scelte per lo studio sono tre Seyfert di tipo 2: IC5063, NGC5643 e NGC7212. Le galassie sono di diverso tipo morfologico, in quanto IC5063 è lenticolare, NGC5643 è una tipica spirale e NGC7212 è una spirale in forte interazione con altri due oggetti simili. In ogni caso è stata osservata in ciascuna galassia un ENLR più o meno estesa (Colina, Sparks, and Macchetto 1991, Morris et al. 1985, Schmitt et al. 2003), e questo è il motivo per cui sono state scelte per questo lavoro.

Nel capitolo 1 verranno descritte le caratteristiche principali del Modello Unificato e dei coni di ionizzazione, comprese le attuali teorie per l'origine del gas che li compone. Quindi, nel capitolo 2, saranno presentate le galassie scelte, gli strumenti utilizzati per le osservazioni e infine verranno descritte le osservazioni stesse. Nella seconda parte di questo capitolo verranno presentati tutti i passaggi della riduzione dei dati. Il capitolo 3, invece, comprenderà tutti i processi di post-riduzione dei dati che sono stati eseguiti, oltre alla normale riduzione, prima di passare all'analisi che sarà descritta nel capitolo 4. Per concludere, nel capitolo 5 saranno riportati i risultati ottenuti per ciascuna galassia, mentre nell'ultimo capitolo verranno esposte le conclusioni.

Contents

Chapter 1

Active Galactic Nuclei

An active nucleus is a particular type of galactic nucleus whose peculiarity is a strong emission in a wide range of wavelengths, which cannot be caused by stellar emission. Actually, the name AGN is used to identify a large variety of phenomena whose principal feature is to emit a strong bolometric luminosity ($L_{bol} \sim 10^{42} - 10^{47}\,\mathrm{ergs}^{-1}$) within a very small region (from $\sim 10^{-5}$ to $\sim 200\,\mathrm{pc}$), but they have different spectral characteristics. However, they are all called AGN because Antonucci (1993) proposed a model which can explain all their features as the effects of the accretion of a nuclear Supermassive Black Hole (SMBH), with a mass $M_{SMBH} > 10^6\,\mathrm{M}_\odot$, seen by different inclinations of lines of sight. A galaxy which hosts an AGN in its nucleus is called active galaxy, but, often, the term AGN is used to refer to the galaxy itself and not only to its nucleus.

1.1 AGN Classification

There are different kinds of AGN and it is possible to classify them according to their characteristics. The main subdivision depends on the features of the radio emission. Where an AGN presents a strong emission at radio wavelengths, it is classified as *radio-loud*, while if the radio emission is weak it is classified as *radio-quiet*. The parameter which consents to separate the two classes of object is the ratio between the radio flux density at $\lambda = 6\,\mathrm{cm}$ and the optical flux density (Kellermann et al. 1989). Radio-quite objects have R ranging between 0.1 and 1, while radio-loud AGN have R ranging between 10 and 1000 (Kellermann et al. 1989). The radio-loud class can be further divided in quasars, blazars and radio galaxies, while the radio-quiet objects are: QSOs, Seyfert galaxies and LINERs.

Quasars are among the most luminous AGNs of the universe. Their name is a contraction of *quasi-stellar radio source* and their principal feature is a strong emission in the radio band, which is produced by an optical point-like source. They have an optical spectrum characterized by a non-thermal continuum with strong high-ionization emission lines. Similar objects are the QSOs (*Quasi Stellar Objects*). They have the same properties of quasars but they do not have their typical radio spectrum. Lately the name QSO is no longer used and now we distinguish between radio-loud and radio-quiet quasars.

Seyfert galaxies are a class of AGNs discovered by Carl Seyfert in the first half of the twentieth century. They have a spectrum similar to that of QSOs, but with

lower luminosity. Seyfert 1 galaxies and QSOs have, in particular, the same spectral properties and it is difficult to separate bright Seyfert galaxies from faint QSOs.

Blazars and radio galaxies are AGNs that have strong emission in the radio band. The radio emission of the latter comes from one or two diffused regions that cannot be easily associated to some structures in other bands of the electromagnetic spectrum, the radio lobes. Few galaxies show emission coming from a very narrow and collimated structure that starts in the nucleus of the galaxy and reaches the radio emission regions. These structures are called jets. Some radio galaxies have an optical spectrum similar to that of Seyfert galaxies. In this case they are called Broad Lines Radio Galaxies or Narrow Line Radio Galaxies according to the width of the permitted emission lines. On the contrary, blazars are characterized by a very strong radio emission coming from a small region of the nucleus. Their emission is also highly variable at all wavelengths. Historically, they can be divided into two classes of objects based on the features of the optical spectrum: BL Lacertae and OVV (Optically Violently Variable quasars).

The last type of AGN is the LINERs class. LINERs, acronym for Low-Ionization Nuclear Emission-Line Regions, are galaxies that present strong, but narrow, low-ionization emission lines. They are very common in the nearby Universe: Heckman (1980) and Ho, Filippenko, and Sargent (1997) found out that almost one third of the galaxies in the nearby universe are LINERs.

1.2 The Unified Model

The combination of all classes of AGNs is described by the so-called Unified Model (Antonucci and Miller 1985, Antonucci 1993). This model explains the features of all AGNs as the result of a quite simple structure which can be seen under different inclination of lines of sight (Fig. 1.1). The components of an AGN are:

- *Supermassive black hole* (SMBH): it is the central engine of the AGN and can have masses between $10^6 - 10^9\,\mathrm{M}_\odot$;
- *Accretion disk*: it is a disk composed by gas and dust gravitating around the central black hole at typical distances of the order of $r \sim 10^{-3}\,\mathrm{pc}$;
- *Broad Line Region* (BLR): it is a region that surrounds the SMBH and the accretion disk ($r \sim 0.01 - 0.1\,\mathrm{pc}$) characterized by the presence of highly ionized gas clouds, with density around $N_e \sim 10^9 - 10^{12}\,\mathrm{cm}^{-3}$, whose spectra present only permitted lines with Full Width at Half Maximum (FWHM) $\sim 10^4\,\mathrm{kms}^{-1}$, because the density is too high to produce forbidden lines;
- *Dusty torus*: it is a structure, composed by dust and molecular gas, placed beyond the BLR at about $r \sim 1 - 100\,\mathrm{pc}$ from the central SMBH. Dust and molecular gas are optically thick and can obscure the emission of the central region, if the line of sight is about perpendicular to the torus axis;
- *Narrow Line Region* (NLR): it is a region similar to the BLR but with lower density ($N_e \sim 10^2 - 10^4\,\mathrm{cm}^{-3}$) and at a distance from the center of $r \sim 10^2 - 10^3\,\mathrm{pc}$. The spectrum is characterized by forbidden and permitted lines with typical FWHM$\leq 10^3\,\mathrm{kms}^{-1}$, the strongest optical forbidden lines are [O III]$\lambda\lambda 4959, 5007$;

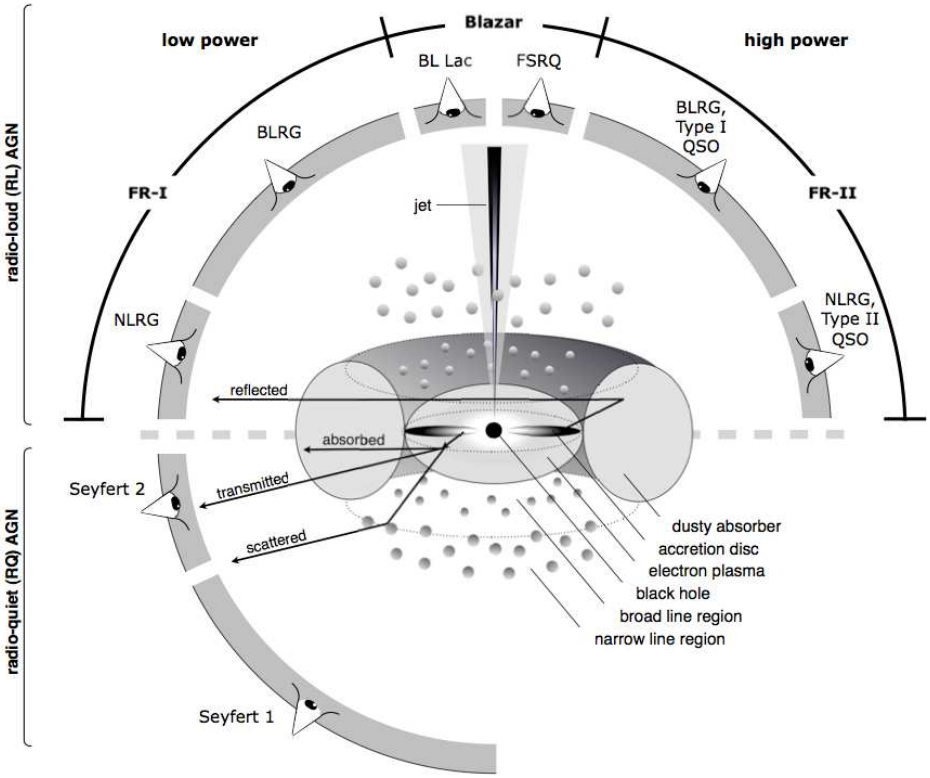

Figure 1.1: The Unified Model of the AGNs (Beckmann and Shrader 2012). The different AGNs are the same object seen from different lines of sight.

- *Jets*: they are jets of charged particles, moving with relativistic speed, emitted by the nucleus.

Keeping these structures in mind, it is possible to understand why the Unified Model can explain all the different classes of AGN previously described (Fig. 1.1). If the AGN is seen face on, or if the line of sight is in such a way that it is possible to observe the central region of the nucleus, it is classified as a Type 1 AGN. Some examples of Type 1 AGNs are Sefert 1 galaxies and radio-quiet quasars. On the contrary, if the AGN is seen edge on, the dusty torus blocks all the radiation coming from the inner region, so it is possible to observe only the NLR spectrum. These objects are classified as Type 2 AGNs (Seyfert 2 galaxies). Radio-loud galaxies are AGNs that have a couple of relativistic jets which emit synchrotron radiation. In this case the analogous of Seyfert 1, Seyfert 2 galaxies and radio-quiet quasars are Broad Line Radio Galaxies (BLRGs), Narrow Line Radio Galaxies (NLRGs) and radio-loud quasars, or blazars, respectively.

1.3 Ionization Cones

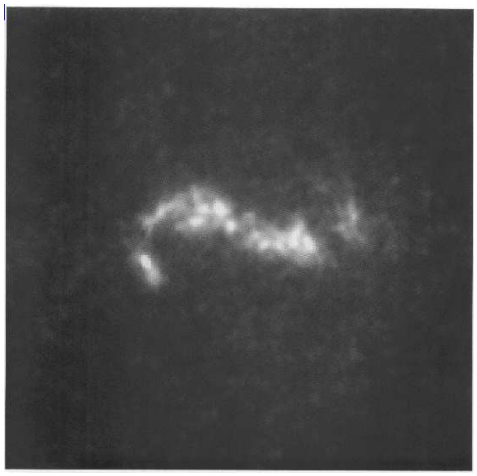

Figure 1.2: An example of ionization cones. HST observation with the F501N filter, centered on the [O III]λ5007 emission line, of the Seyfert 2 Mrk 3. (Capetti et al. 1995)

In the last 25 years, it has been found that some Seyfert galaxies show an extended region of highly ionized gas, which can even be as large as $15 - 20\,\mathrm{kpc}$ (Mulchaey, Wilson, and Tsvetanov 1996, Schmitt et al. 2003), with similar features of those of the NLR. This structure is called Extended Narrow Line Region (ENLR). Detailed studies in near active galaxies revealed that most of the ENLR have a conical or bi-conical shape, whose apexes point to the AGN at the center of the observed galaxy. In these cases, they can also be called *ionization cones*. In general, the emission of the ENLR is produced by the gas of the host galaxy that is excited and ionized by the continuum emission coming from the nucleus. As already mentioned, the Unified Model (Antonucci 1993) predicts that the dusty torus can absorb part of the radiation coming from the inner region of the AGN and this produces an anisotropic ionizing field with conical shape. The existence of the ionization cones confirms the prediction, proving the validity of the Unified Model (Wilson and Tsvetanov 1994).

The studied ionization cones are both single and double cones, with opening angles between 40° and 100°. When only single cones are observed it is possible that another cone is present in the opposite side of the galaxy and that it cannot be observed because the interstellar dust absorbs all of its radiation. Furthermore, since when the two cones are observed they are perfectly aligned, we can infer that the intrinsic shape of these structures is the bi-conical one.

From the Unified Model, assuming a spherical distribution of gas around the AGN, we can expect that the ionization cones can be observed only in Seyfert 2 galaxies. On the other hand, in Seyfert 1 galaxies, it is expected to be observed a halo of ionized gas surrounding the AGN, because the line of sight is inside the ionized cone. The presence of ionization cones in intermediate-type Seyfert galaxies can questioning the assumption of the thick dusty torus collimating the radiation (e. g. the case of NGC4151, studied by Evans et al. (1993)). In this kind of galaxy it is expected a structure which is halfway between ionization cones and a halo. If also in these cases well defined ionization cones are observed, the presence of other collimation mechanisms must be supposed (Evans et al. 1993). For example, a disk-like BLR can collimate the emission of radiation instead of the dusty torus. Consequently the opening angle cannot be determined only by the dimension of the dusty torus, but it is influenced also by the collimation mechanisms at work and by the distribution of matter and gas outside the AGN.

The presence of the ENLR also means that the NLR cannot absorb all the ionizing radiation coming from the inner part of the AGN, but some of it must escape in order to ionize the gas (Evans et al. 1993). Different works proved that the ionization cones are well aligned with the radio emission axis (Unger et al. 1987) and with the jets, if present (Wilson and Tsvetanov 1994). Wilson and Tsvetanov (1994) speculated that radio emission and ionization cones are collimated by the same structures and also that the presence of jets is fundamental for the formation of the ionization cones. The strong emission of particles forming the jets is probably able to clear a path in the NLR, lowering its density and allowing the radiation to escape and ionize the outer gas. Furthermore, other works (Wilson and Willis 1980, Whittle 1985, Whittle 1992) proved that the luminosity of the [O III] lines is correlated with the luminosity of the radio spectrum on kiloparsec scale and that the kinematics of the gas is influenced by the radio jets (Baldwin, Wilson, and Whittle 1987). Some papers also suggested that the source of ionizing photons are the radio jets itself (e. g. Bicknell et al. 1998). Observation on small scale with the Very Long Baseline Interferometer (VLBI) in the radio band (Harrison et al. 1986) and with Hubble Space Telescope (HST) with filters centered on the [O III]λ5007 line (Evans et al. 1993) confirmed that radio jets form at distance $< 2\,\mathrm{pc}$ from the center of the AGN and that the ionization cones form at distance $< 20\,\mathrm{pc}$, so the origins of the two phenomena could be the same.

1.4 Origins of the Gas

To date, the number of AGNs in which a bright ENLR was detected is poor. There can be different reasons, but the most relevant are two. The first thing to notice is that this kind of NLR can be easily observed only in nearby objects, because of the extended and diffuse nature of the structure itself and its low luminosity, compared to that of the nuclear region, so there might be a selection effect at work. The other

possible reason is that there is not enough gas to be excited. In different papers of the last 20 years, it was suggested that the gas can originate from merging between two or more galaxies, where one of them must be a gas rich galaxy. Some examples of AGN in which merging is believed to have formed the ENLR are: NGC5252 (Morse et al. 1998), Mrk 3 (Di Mille 2007), NGC4388 (Ciroi et al. 2003), Mrk 315 (Ciroi et al. 2005), 4C 37.43 (Fu and Stockton 2007), NGC7212 (Cracco et al. 2011). Despite all of these studies the origin of the ionized gas is still an open problem, so it is interesting to more deeply analyse the gas properties.

The starting point is to notice that the NLR and the ENLR are not identical. The NLR has broader ($10^3\,\mathrm{kms}^{-1}$) and brighter emission lines, because they originate in regions near the galactic nucleus. On the other hand, the further ENLR is characterised by narrower and fainter [O III] emission lines (Unger et al. 1987). Unger et al. (1987) stated also that the ENLR show a more orderly velocity field than that of the NLR, which make it possible to distinguish the two regions kinematically. The ENLR is also different from the usual star formation region, because the gas ionization degree in the first structure is higher than that of the H II region gas (Wilson 1988). Another important ENLR feature is that the gas is organized in structures like clouds and filaments which complicate the study of the region (Capetti et al. 1995). Usually, gas clouds can be classified as *radiation-bounded* or *matter-bounded*. The first ones are region bounded by radiation. They show all the different ionization states and there can be matter beyond their limits. Limits exist because all the ionizing photons are absorbed by the gas. Matter-bounded clouds, on the other hand, are clouds with a well defined volume, often without a ionization stratification. Well defined ionization cones with sharp bounds are clear examples of radiation-bounded clouds (Tadhunter and Tsvetanov 1989).

The first step in studying the gas is to measure the temperature and the electron density through emission lines ratios. The ratio between [O III]$\lambda\lambda$4959, 5007 and [O III]λ4363 is very sensitive to the gas temperature, while [S II]λ6717/[S II]λ6731 is one of the best electron density marker. The expected values are $1 - 2 \cdot 10^4\,\mathrm{K}$ for the temperature, if the ionization mechanism is photoionization, and $10^2 - 10^4\,\mathrm{cm}^{-3}$ for the density of the NLR.

Another important gas feature is the metallicity. This value is very important to investigate the gas origin. If the gas comes from regions belonging to the galaxy it is expected to show supersolar metallicity, because it had the time to be processed by stars which produce all of the elements heavier than hydrogen and helium. On the other hand, gas coming from the extragalactic medium is expected to show subsolar values of metallicity, because it had not the time needed to be enriched with heavy elements. There is a third option: the gas comes from the extragalactic medium but had enough time to be partially processed by recent episodes of star formation, which could be started because of the gas movements when falling into the accretion disk. In this case the metal abundance could be modified but it is possible to distinguish between this gas and the one from the galaxy because they have different metallicity values. The metallicity measurement is quite problematic in this kind of regions because in general there is not a sufficient knowledge of the ionizing source, therefore it is impossible to select reliable metallicity indicators in these conditions. The metal abundances measured up to now were all obtained from the extrapolation of the radial metallicity profile in the galaxy nucleus. Only in recent times there have been some attempts to

find new metallicity indicators for AGN, at least for some of them (Groves, Heckman, and Kauffmann 2006). The typical values are from 2 to 5 times the solar metallicity in Seyfert 2 galaxies and in LINERs (Storchi Bergmann and Pastoriza 1989, Storchi-Bergmann and Pastoriza 1990, Komossa and Schulz 1997). Groves, Heckman, and Kauffmann (2006) only found 40 AGN over a sample of $\sim$ 23000 Seyfert 2 galaxies with subsolar metallicity, so it is possible to affirm that most of AGNs have supersolar metallicity.

The gas origin affects also the kinematics of the ENLR ionized gas. If the ENLR gas has an inner origin, it will probably have a regular kinematics, similar to that of the hosting bulge. On the other hand, if it has an outer origin or it is expelled from the active nucleus it could show a complex kinematics, with clouds and filaments that radially move at different velocities. This kind of kinematics is observed in galaxies as: Mrk 3 (Di Mille 2007), NGC4388 (Veilleux, Bland-Hawthorn, and Cecil 1999, Ciroi et al. 2005), Mrk 533 (Smirnova et al. 2007). The analysis of the emission lines profiles shows asymmetries in the most prominent lines ([O III], Hβ) proving the presence of this complex kinematics.

The last kind of analysis that is possible to carry out is focused on the ionizing source. Comparing some ratios between the brightest emission line of the spectra it is possible to create the so-called *diagnostic diagrams* (Baldwin, Phillips, and Terlevich 1981, Veilleux and Osterbrock 1987) which make it possible to understand if the ionizing source is a thermal continuum, a non-thermal one or shock-waves. Useful lines ratios often involve a forbidden line (for example [O III]λ5007) and a hydrogen Balmer line. These lines are close in wavelengths, in order to reduce the reddening effect.

Chapter 2

Observations and Data Reduction

The purpose of this work is to carry on the study of the ENLR in nearby AGN started by Cracco et al. (2011) and Bisigello (2012), increasing the sample of studied galaxies. As seen before, the ENLR is composed by gaseous structures, like clouds and filaments, which can have different physical and kinematics properties (such as temperature, density, velocity). The most evident feature is the clouds velocity. Every cloud produces a spectrum with a Doppler shift that depends on the radial velocity of the cloud itself. When all of the spectra produced by the single clouds sum up and generate the data acquired by a normal long-slit spectrograph, the profile of the emission lines can show features as asymmetry and multiple peaks. In order to separate the components coming from the different structures, we need spectra acquired with instruments which can provide a sufficient resolution. A good instrument is a medium resolution ($R \sim 10000$) echelle spectrograph. High or very high resolutions are not recommended because the exposure time increases with the dispersion (at equal light collecting power of the telescope) and also the different velocity components could be intrinsically large so, even increasing the resolution, it is not possible to separate the components beyond a limit.

The galaxies chosen for this work are: IC5063, NGC5643 and NGC7212. I studied these galaxies combining the technique developed by Ozaki (2009) with that used by Bisigello (2012). The Ozaki's method consists in separating emission lines (Hβ, [O III]$\lambda\lambda$5007, 4959, [O I]λ6300, [Fe VII]λ6087) in low velocity bins, and then studying their fluxes. The Bisigello's one consists in trying to separate the components by fitting every single emission lines ([O II]λ3727, [O III]λ4363, Hβ, [O III]$\lambda\lambda$4959, 5007, [O I]λ6300,[O I]λ6363, [N II]$\lambda\lambda$6548, 6584, [S II]$\lambda\lambda$6717, 6731) with the same number of Gaussians, in order to measure quantities like temperature and density from emission lines ratios, assuming that each Gaussian represents the same component in each mesured line. In this work I am going to measure the emission lines ratios such as in Bisigello (2012) but using the approach of Ozaki (2009). I will use these measurements to produce diagnostic diagrams (Baldwin, Phillips, and Terlevich 1981) to investigate the ionization mechanism and also to measure, if possible, other gas properties.

2.1 The Sample

2.1.1 IC5063

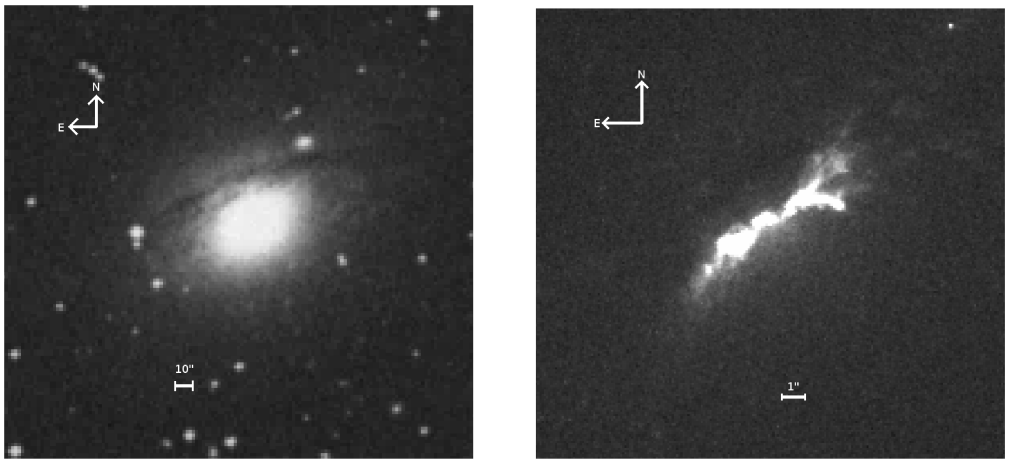

Figure 2.1: Images of the Seyfert galaxy IC5063. (a) IC5063 from DSSI, (b) image of the ENLR of IC5063 taken with the FR533N filter of HST.

Table 2.1: Principal IC5063 data taken from NED.

RA (J2000)	$20^{h}\ 52^{m}\ 02^{s}$
Dec (J2000)	$-57^{d}\ 04^{m}\ 08^{s}$
Redshift	0.01135
B magnitude	12.89
Morfology	S0

IC5063 (Fig. 2.1) is a lenticular galaxy classified as a Seyfert 2 galaxy (Morganti et al. 2007). Tab. 2.1 lists some of the principal data about the galaxy as reported by NASA/IPAC Extragalactic Database (NED)[1]. One of its main features is the existence of a complex system of dust lanes. It also shows a strong IR emission (Hough et al. 1987) and a very broad component of Hα (Inglis et al. 1993) in polarized light, which can be explained as a trace of the obscured BLR.

The galaxy presents three radio emission regions aligned with the dust lanes: the central one is a non-resolved nuclear emission region, the remaining two are resolved radio jets. Morganti et al. (2007) studied these radio emission regions, measuring the position angle (PA) of the jets axis and looking for signs of ionized gas around the regions. They measured PA$\sim 117°$ and found a very extended region of ionized gas emitting lines like Hα and [O III]$\lambda\lambda$4959, 5007. These emission lines can be measured to a distance of about $15 - 16$ arcsec ($3.5 - 3.8$ kpc[2]) from the nucleus in a direction close

[1]The NASA/IPAC Extragalactic Database (NED) is operated by the Jet Propulsion Laboratory, California Institute of Technology, under contract with the National Aeronautics and Space Administration.

[2]From now on the distances will be measured with $H_0 = 70\,\mathrm{kms}^{-1}\mathrm{Mpc}^{-1}$

to the one identified by the jets axis. The ENLR was already found by Colina, Sparks, and Macchetto (1991). They discovered a very extended region of ionized gas with a peculiar X shape, with the orientation of its axis in agreement with Morganti et al. (2007) and an opening angle of about 50°. They also supposed that the ENLR is the result of a quite recent merging between an elliptical galaxy and a small gas-rich spiral galaxy. Both the neutral and the ionized gas of the ENLR gas show signs of a quite fast outflow, with velocity of about 600 $\mathrm{km s^{-1}}$. The last one seems to be interacting with the radio emitting regions of the jets. The existence of the outflows was confirmed by Tadhunter et al. (2014), who justified their presence with the acceleration of gas by shocks.

2.1.2 NGC5643

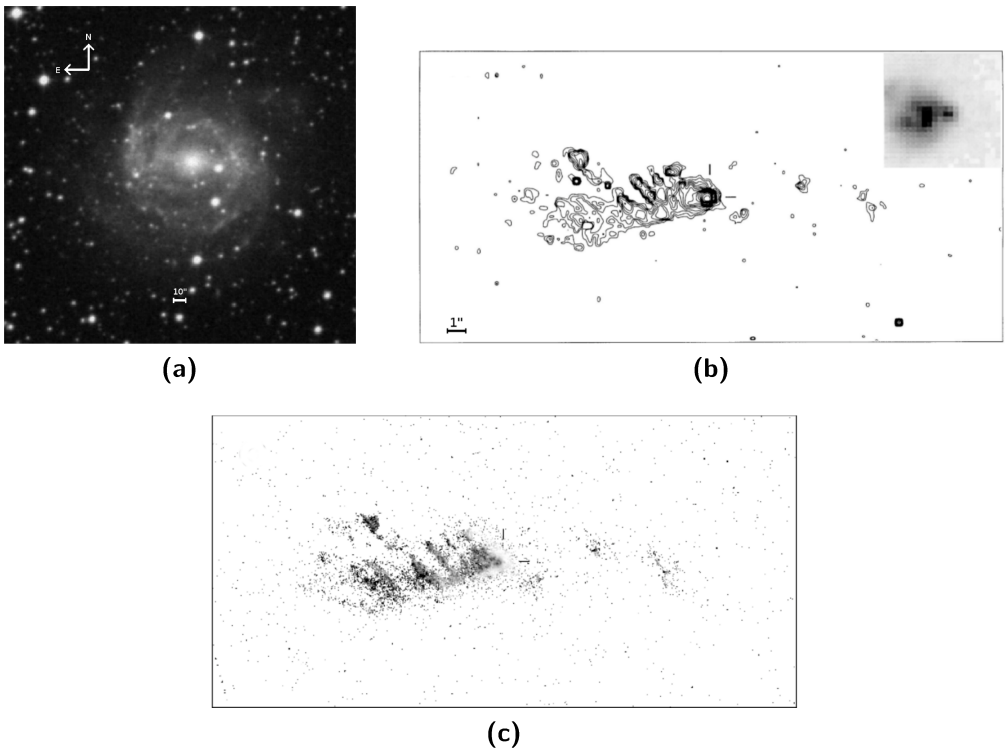

Figure 2.2: Images of the Seyfert galaxy NGC5643. (a) NGC5643 from DSSII-red, (b) [O III] contours of the ENLR of NGC5643 from Simpson et al. (1997), (c) excitation map ([O III]/Hα) by the same paper. The darker points correspond to higher [O III]/Hα ratios.

Table 2.2: Principal NGC5643 data taken from NED.

RA (J2000)	$14^{\mathrm{h}}\ 32^{\mathrm{m}}\ 40.7^{\mathrm{s}}$
Dec (J2000)	$-44^{\mathrm{d}}\ 10^{\mathrm{m}}\ 28^{\mathrm{s}}$
Redshift	0.004
B magnitude	10.74
Morfology	SABc

NGC5643 (Fig. 2.2) is a late-type barred spiral galaxy, classified as a Seyfert 2 galaxy (Schmitt, Storchi-Bergmann, and Baldwin 1994, Simpson et al. 1997). Some of its main data are presented in Tab. 2.2, as reported by NED. The ENLR of this object was already discovered in the early 90's and it clearly showed the shape of an ionization cone with an axis coincident with the jets one (Morris et al. 1985, Schmitt, Storchi-Bergmann, and Baldwin 1994), at PA= 87° ± 3°. The radio jets and the ENLR are elongated in the direction of the galaxy bar, up to a distance of about 14 arcsec (1.2 kpc) as reported by Morris et al. (1985). They also supposed that the bar influences the motion of the gas in a significant way. A flow of gas through the bar toward the nucleus could form a compact disk with the axis parallel to the one of the bar. This disk would then allow the ionizing photons and the radio plasma to escape preferentially along this axis.

Later, Simpson et al. (1997) showed that the ENLR could have a bit different shape. They found a halo of [O III] and Hα emission centered on the nucleus with a 1 arcsec radius and an extranuclear emission extended only on one side of the galaxy. The [O III]/Hα excitation map revealed that the ionized gas is distributed in a V-shaped structure (PA= 84°, aperture angle= 58°), the typical shape of ionization cones. In addition, the apex of the cone showed a drop of the [O III]/Hα ratio, which could be related to the reddening produced by a strong absorption. On the opposite side of the nucleus it is possible to see two knots of high-excitation gas, which are within the boundaries of a putative second cone. These facts lead to think that another ionization cone likely exists on the opposite side of the galaxy, completely absorbed by the dust of the Interstellar Medium (ISM).

2.1.3 NGC7212

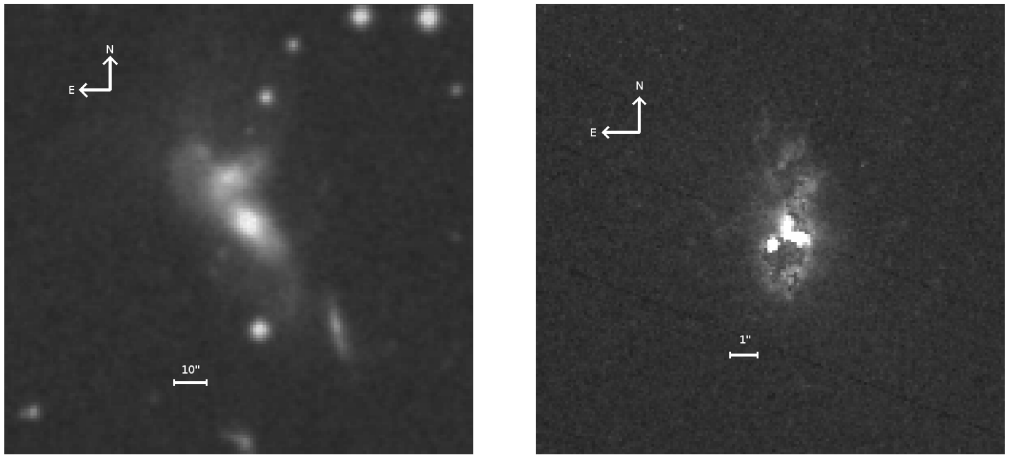

Figure 2.3: Images of NGC7212. (a) NGC7212 from DSSII-red, (b) image of NGC7212 taken with the FR533N filter of the Hubble Space Telescope.

NGC7212 (Fig. 2.3) is the third studied galaxy in this work and some of its data are reported in Tab. 2.3. It is a spiral galaxy, belonging to a system composed by three interacting objects, and classified as Seyfert 2 by Wasilewski (1981). One of the first

Table 2.3: Principal NGC7212 data taken from NED.

RA (J2000)	$22^h\ 07^m\ 01^s$
Dec (J2000)	$10^d\ 13^m\ 52^s$
Redshift	0.026632
B magnitude[1]	14.78
Morfology	Sab

[1]Muñoz Marı/n et al. 2007

papers about the NLR of NGC7212 was published by Tran (1995) who studied some Seyfert 2 galaxies in polarized light and found an elongated NLR in NGC7212, with an axis at PA= 170°, aligned with a jet-like structure of highly ionized gas. Then, Falcke, Wilson, and Simpson (1998) discovered the presence of a diffused and extended NLR also in non-polarized light, in a compatible direction with the previously found jet-like structure, but without the well defined shape typical of ionization cones. They also discovered that the jet and the ENLR seemed to be in interaction between each other.

The existence of the ionization cones was finally confirmed by Cracco et al. (2011). This structure extends from the nucleus to about $3 - 4$ kpc in both direction and it is almost aligned with the minor optical axis of the galaxy (PA= 150°). Cracco et al. (2011) also studied the kinematics and physical properties of the gas. They found that [N II]/Hα and [S II]/Hα ratios are quite high, especially in the interaction region between NGC7212 and one of the other galaxies of the triplet. This might suggest that the ionization mechanism of the gas is a combination of photoionization from a non-thermal continuum and shocks. Another feature of the gas emission is a certain degree of asymmetry in the emission lines of the spectra, sign of the presence of radial motions of the gas inside the cone. These properties, together with a very likely sub-solar metallicity of the ENLR, can suggest that the gas has an external origin, probably due to the interaction with the other galaxies.

2.2 Instrumentation

As previously said, to carry out this kind of analysis, spectra with high enough resolution are needed. An echelle spectrograph is specially developed in order to produce high resolution spectra, thanks to the presence of two dispersive elements inside the instrument. The first element is a blazed grating with few lines for millimeter, but large blaze angle, which allows to move the light intensity maximum from the zeroth to higher diffraction orders, and therefore to produce an high resolution spectrum. This spectrum passes through the second dispersive element, usually a low dispersion prism or a grism, rotated in a way that the direction of its dispersion is perpendicular to the one of the previous grating. In this way, it is possible to separate the interference orders. With this configuration we can obtain very high resolution (R$\geq$ 100000). On the other hand, a huge amount of light is needed to acquire spectra with a sufficient signal-to-noise ratio (S/N) at such a high resolution. In fact, echelle spectrographs are typically used to study stars, because galaxies are too faint to obtain good spectra in a fair amount of time. However, today it is possible to observe galaxies using large telescopes, which

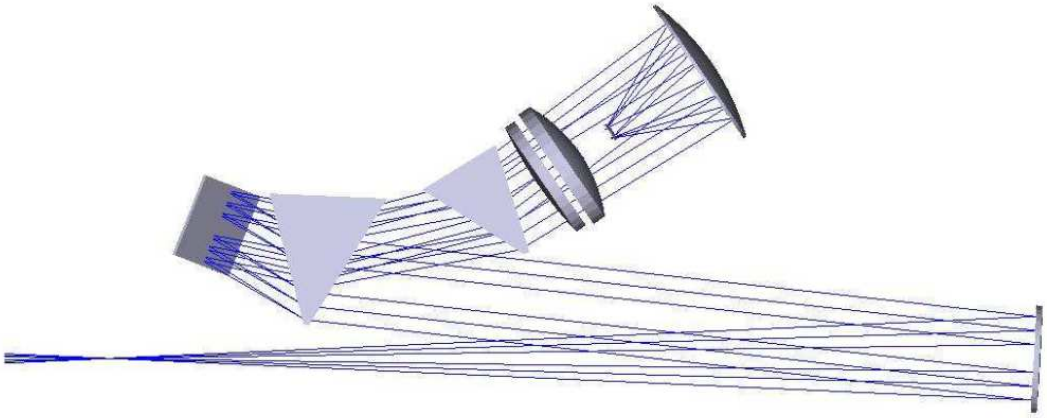

Figure 2.4: Optical scheme of the MagE spectrograph (Marshall et al. 2008). The light enters inside the instrument in the bottom-left side of the image and it is collimated by an off-axis parabolic mirror. Then the beam passes through a first cross-dispersing prism and reaches the reflecting grating. Finally it proceeds through a second cross-dispersing prism before entering the camera.

Table 2.4: Principal features of MagE spectrograph (Marshall et al. 2008).

Spectral range	$3100 - 10000\,\text{Å}$
Resolution	8100 (slit width = 0.5 arcsec)
Slits width	0.5, 0.7, 0.85, 1.0, 1.2, 1.5, 2.0, 5.0 arcsec
Slits lenght	10 arcsec
CCD size	2048x1024 px
Pixels size	13.5 µm
Spatial scale	$0.3\,\text{arcsecpx}^{-1}$

can collect the needed light in a relative short time, and instruments with a resolution sufficient to have a good sampling of the emission lines but in a relatively short time.

The data used for this work were acquired with the MagE spectrograph (Magellan echellette spectrograph). It is a medium resolution echelle spectrograph in the visible band, optimized for a high efficiency in the blue region of the spectrum. Eight different slits are available for the observations, each of them is 10 arcsec long, and a grism giving a resolution R $\simeq$ 8000 (combined with the 0.5 arcsec slit). MagE is installed at the Nasmyth focus of the Clay telescope, one of the two instruments that form the Magellan telescope (the other is named Baade), situated on an isolated peak in the Atacama desert (Cerro Manqui), Chile, at the Las Campanas Observatory.

The observatory is managed by a collaboration between Carnagie Institute of Washington, University of Arizona, Harvard University, University of Michigan and Massachusetts Institute of Technology. The two telescopes have a gregorian configuration with three possible focuses: two f/11 Nasmyth and one f/15 Cassegrain. They are situated at a distance of 60 m and between them there are 3 small auxiliary f/11 telescopes. It is possible to correct part of the atmospheric dispersion with an Atmospheric Dispersion Corrector (ADC) in order to increase the corrected field of view in wide field observations with the f/11 focuses. The principal features of MagE and Clay

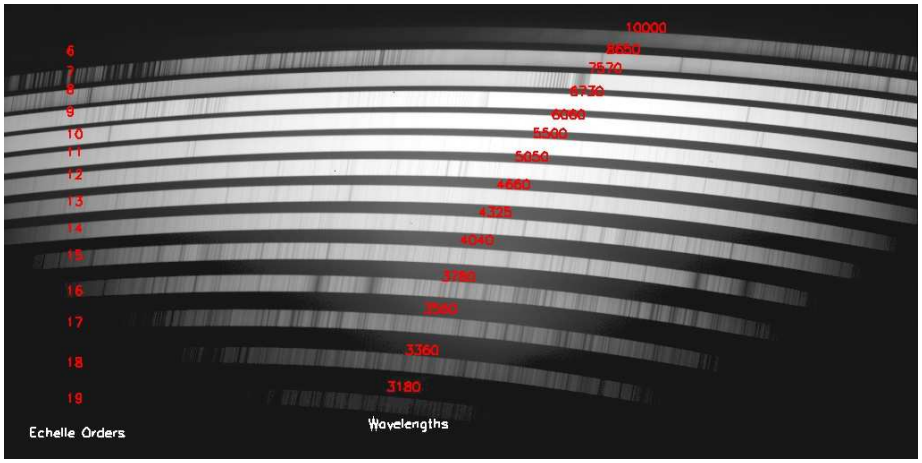

Figure 2.5: Solar spectrum acquired with MagE (Marshall et al. 2008). In the image you the order numbers and their central wavelengths are reported.

Table 2.5: Principal features of the Clay telescope

Primary mirror diameter	6502.4 mm
Focal lenght	8128.0 mm
Shape	paraboloid
Configuration	gregorian
Focal ratio (Nasmyth)	f/11
Focal ratio (Cassegrain)	f/15
Field of view	6 arcmin
Field of view (with ADC)	24 arcmin

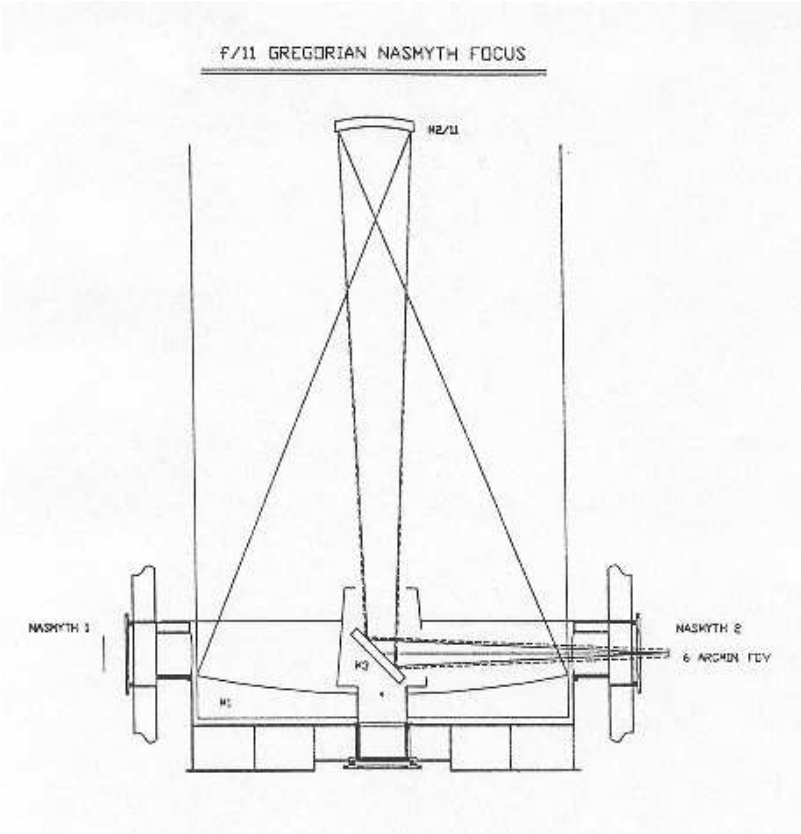

Figure 2.6: Optical scheme of one of the telescope of the Magellan in the f/11 Narrow Field Configuration. It is possible to see the primary parabolic mirror and the Gregorian secondary. The tertiary mirror rotates to select the different instruments mounted at the Nasmyth focuses. In Wide Field Configuration the ADC is inserted immediatley after the tertiary mirror. The primary mirror uses active controls to correct the low-order aberration in the optical system. In addition, the secondary mirror has a tip-tilt mechanism for fast guiding.

Table 2.6: Observation features.

	IC5063	NGC5643	NGC7212
N° of exposure	2	5	5
Total exposure time (s)	2400	6000	6000
Position angle (deg)	123	296	344

telescope are presented in Tables 2.4 and 2.5 and the optical schemes of MagE and Clay telescope in Figs. 2.4 and 2.6. Finally in Fig. 2.5 the solar spectrum acquired with the MagE spectrograph is shown with the order numbers and the central wavelength for each order.

2.3 Observations

The observations were made during the nights of May 29th and 30th, 2010. As already said, the instrument used was MagE with the 0.5 arcsec slit, which allows to reach the highest possible resolution. With this configuration the spectrograph resolution is R $\sim$ 8000 (Marshall et al. 2008). All the galaxies were observed with multiple exposures of 1200 s each and in Tab. 2.6 there are some information about the observations. Additional images were also acquired to perform data reduction. In order to carry out the wavelength calibration, every two acquisitions of the galaxy spectrum, a spectrum of a Thorium-Argon (Th-Ar) calibration lamp was obtained as well. To subtract the contribution of the night sky, a spectrum of a sky region without any light source was also acquired for each galaxy. The exposure time for this kind of image was the same of the science images. This step was necessary because the light of the galaxies extend well beyond the small length of the slit, so it is not possible to estimate the sky contribution without this kind of images. In order to perform the flux calibration, some standard stars were observed.

2.4 Data Reduction

There are some differences between echelle data and standard long-slit spectra which make the two data reduction processes different. The main distinctive features of an echelle spectra are two: the object spectrum is arranged in a certain number of orders and each order is curved (Fig. 2.7). For these reasons, automatic data reduction pipelines are often developed and they are able to extract and calibrate the spectra in the best possible way. There are two available pipelines especially developed for MagE: MagE pipeline[3] and MagE Spectral Extractor (MASE) (Bochanski et al. 2009). The main problem with these pipelines is that they are optimized to reduce point-like source spectra, for which the spatial information does not count. In this work the spatial information is very important, therefore it was not possible to take advantage from these pre-built softwares and I decided to make all the reduction with IRAF (*Image Reduction and Analisys Facilities*). The order followed for data reduction was:

[3]http://code.obs.carnegiescience.edu/mage-pipeline

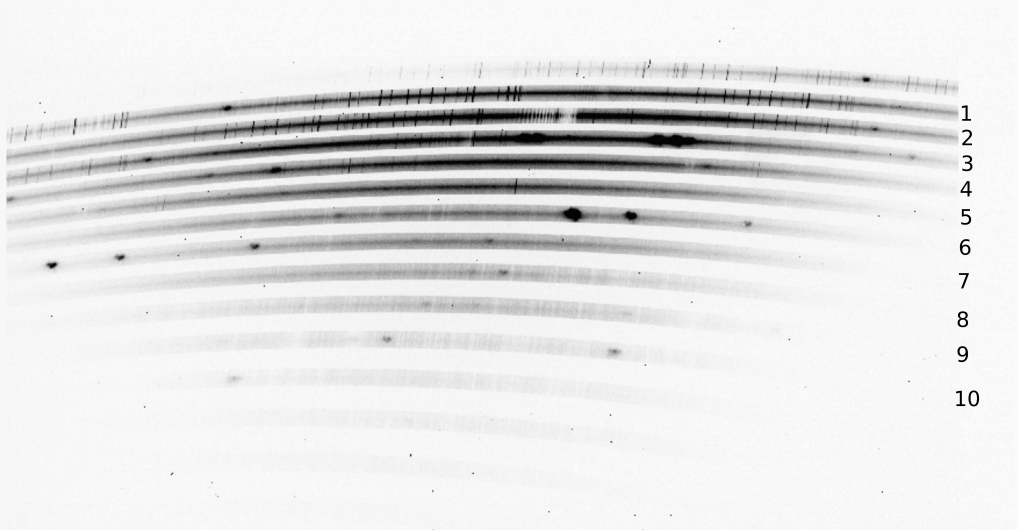

Figure 2.7: Inverted colours spectrum of one of the observed galaxies. On the right there are the order number of the extracted spectra analysed later on. The white strip on top of the image is the overscan region.

- bias subtraction,
- order extraction,
- wavelength calibration,
- flat field correction,
- sky subtraction,
- flux calibration,
- exposure combination.

2.4.1 Bias Subtraction

The first operation consists in subtracting the bias from all of the images that will be used in the following reduction: objects, lamps, flat-field frames and standard stars. Bias is a value added to every pixel of the image when reading the CCD, in order to avoid negative values of the counts because of statistical errors. The main problem here was to measure the correct bias value. Since I had not bias images (images with 0 s exposure time and with the shutter closed) at my disposal, I used the overscan region (Fig. 2.7) to measure the bias value. The overscan region is a small image section, artificially created and read by the electronics, that can be used as a normal bias image. After I measured this value I subtracted it to the images, then I cut away the overscan region.

2.4.2 Order Extraction

The second step in the reduction process was to extract, from the images, the spectra of the dispersion orders (hereafter apertures), which were then reduced one by one

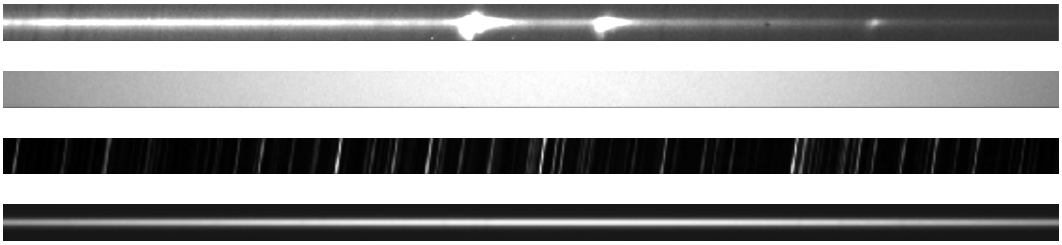

Figure 2.8: From top to bottom: section of the aperture number 6 spectrum of one of the observed object, a flat field, a lamp, a standard star. In the first image it is possible to notice from left to right the [O III] forbidden lines at 5007 and 4959 Å and Hβ at 4861 Å.

as normal long-slit spectra. I extracted ten apertures, identified with numbers from 1 to 10 starting from the upper part of the images (Fig. 2.7). The task used for the extraction was `apall`, which allows, with the `strip` option, to extract and straighten out an image strip. The software needs a reference spectrum with a bright and well defined continuum, for example a standard star spectrum. Moreover it was mandatory to decide a priori the width of the apertures, which had to be constant, because at the end of the reduction I added all of the apertures of each galaxy to obtain a single high-resolution "long-slit" spectrum. This was possible with a flat-field image whose order were evenly illuminated. Then, the software was able to extract each aperture of all the images (objects, flat-field frames, standard stars and lamps) at the same time. In Fig. 2.8 there are some examples of the extracted apertures.

2.4.3 Wavelength Calibration

The following step was the wavelength calibration of the images. For this purpose, different spectra of a Th-Ar lamp were acquired during the observations. The Th-Ar lamp is one of the most diffused calibration lamp for high resolution observations, because it shows a lot of well defined lines arranged on the whole spectral range.

I carried out the calibration in a standard way: with the `identify` task I identified the principal emission lines in the central pixel line of each lamp, than with `reidentify` the identification was applied to the entire frame, trying to keep the error similar to the one of `identify`. Then, with `fitcoord` I created the two-dimensional solution, which transforms the dispersion coordinate from pixels to Angstrom, and I applied it to all the images with the `transform` task. At the end of this process all the scientific images, the sky and standard stars spectra and the flat-field frames were wavelength calibrated. In Fig. 2.9 there is the section of the aperture 6 spectrum of NGC5643 with the Hβ and [O III]$\lambda\lambda$4959, 5007 lines. It is easy to notice, that before the calibration the wavelength increased from right to left and the lines were slightly tilted from left to right. This tilt comes from the fact that the original order was curved, so when the software extracted the apertures the lines came out tilted. The calibration inverts the wavelength increasing direction and straightens out the spectral lines.

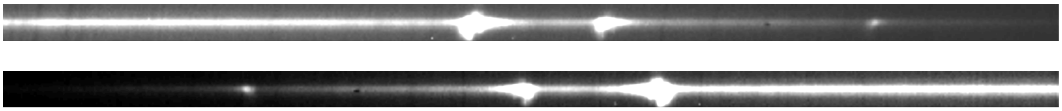

Figure 2.9: NGC5643 aperture 6 spectrum before (top) and after (bottom) the wavelength calibration. The bright emission lines in the first image are, from left to right, [O III]λ5007, [O III]λ4959 and Hβ. After the calibration the wavelength increases from left to right, therefore the lines order is inverted.

Figure 2.10: A typical MagE flat-field frame in inverted colours.

2.4.4 Flat-Field Correction

The following step in the data reduction process is the flat-field correction. A flat-field is an image, acquired with the same instrumental set-up of the scientific images and used to correct small sensitivity differences between the CCD pixels.

In spectroscopy, flat-field frames are obtained in two different ways: using a dedicated lamp inside the instrument or a lamp outside the telescope, whose light illuminates a screen inside the dome. Both lamps must have a strong continuum spectrum without any emission or absorption lines. They are usually acquired before or after the observations.

The actual flat-field correction consists in dividing the images by a normalized average flat-field, often called *master flat*, obtained combining all of the acquired flat-field images. I created a normalized flat-field from each aperture with the `response` task, then I averaged all the obtained frames, in order to achieve the master flat. At the end of the process I made the correction for all the images.

2.4.5 Sky Subtraction

The next step is the sky subtraction. The night sky has not a fixed luminosity, but it can change because of different factors, such as light pollution, observed wavelengths, moon phase. When an object is observed from the ground, its spectrum will be superimposed on the sky spectrum, which will often be a non negligible component of the image. Therefore, in order to study the object spectrum, the sky must be subtracted

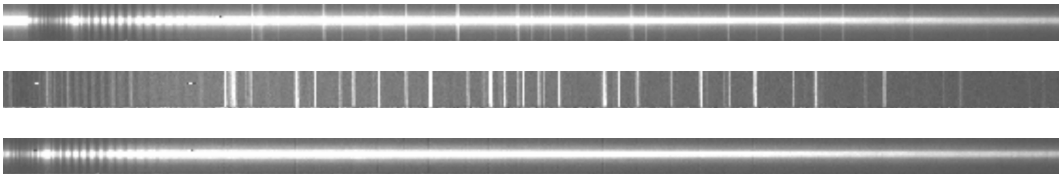

Figure 2.11: From top to bottom the three sky subtraction phases: NGC5643 aperture 2 spectrum, sky spectrum in the same aperture, final spectrum.

from the science images before the analysis.

An optical sky spectrum is made by two components: the continuum, which is present at all wavelengths, and different emission and absorption lines grouped in the green and red regions of the spectrum. Sky emission lines can be useful to verify the wavelength calibration accuracy but they must be removed before data analysis.

In order to subtract the sky contribution from the images, I used the sky spectra obtained during the observations. For each galaxy almost one sky spectrum was acquired, with the same set-up and exposure time used for the corresponding object. Theoretically I had to simply subtract the sky spectrum from the object one but, in reality, the two spectra were not acquired simultaneously and the sky can be strongly variable, so I had to multiply sky spectra for a constant factor in order to match, in the best possible way, the emission lines fluxes in both images. I did this only for the first four or five apertures, where there were emission lines. For the other apertures I simply subtracted the sky spectrum, because it was not possible to estimate the correct multiplying factor. Because of the variability, it is quite difficult to do a perfect subtraction, in fact there could be some residuals, as seen in Fig. 2.11 (c).

I did this reduction step only for the objects spectra. Standards spectra do not need this correction, because exposure times are too short for the sky to rise in these spectra and it is possible to subtract it during the extraction of the one-dimensional spectrum with the `apall` task, if needed.

2.4.6 Flux Calibration

At this point the images are almost ready for the analysis, but fluxes are still measured in ADU (*Analog to Digital Unit*) while the physical units are $\mathrm{erg cm^{-2} s^{-1} \AA^{-1}}$. The conversion between these two units was done with the standard star. A standard star is a star which has tabulated flux measurements at different wavelength bins. Comparing the observed and the tabulated spectra it is possible to create a function, called *sensitivity function*, which allows to calibrate the other images. The sensitivity function, built in this way, also corrects the images for the response of the system atmosphere-telescope-CCD to the various wavelengths. During the nights, different standard stars were observed; they were equivalent in term of air mass, so I calibrated the objects with the only one observed both nights: HR5501 (Fig. 2.12 (a), (c)). First, with the `apall` task, I extracted the one-dimensional spectrum, then `standard` compares the observed and tabulated spectrum (Fig. 2.12 (b)) because the flux measurements are defined only in small bins. The last step is building the sensitivity function with `sensfunc` (Fig. 2.13) which will be applied by `calibrate` to the galaxies spectra. It is very important to select the whole star flux when extracting the 1D spectrum. In

Table 2.7: HR5501 data from *ESO standard stars catalogue* (2015).

Name	RA (hh:mm:ss)	Dec (dd:mm:ss)	Mag (V)	B-V	Spectral type
HR5501	14:45:30.25	00:43:02.7	5.68	−0.02	B9.5V

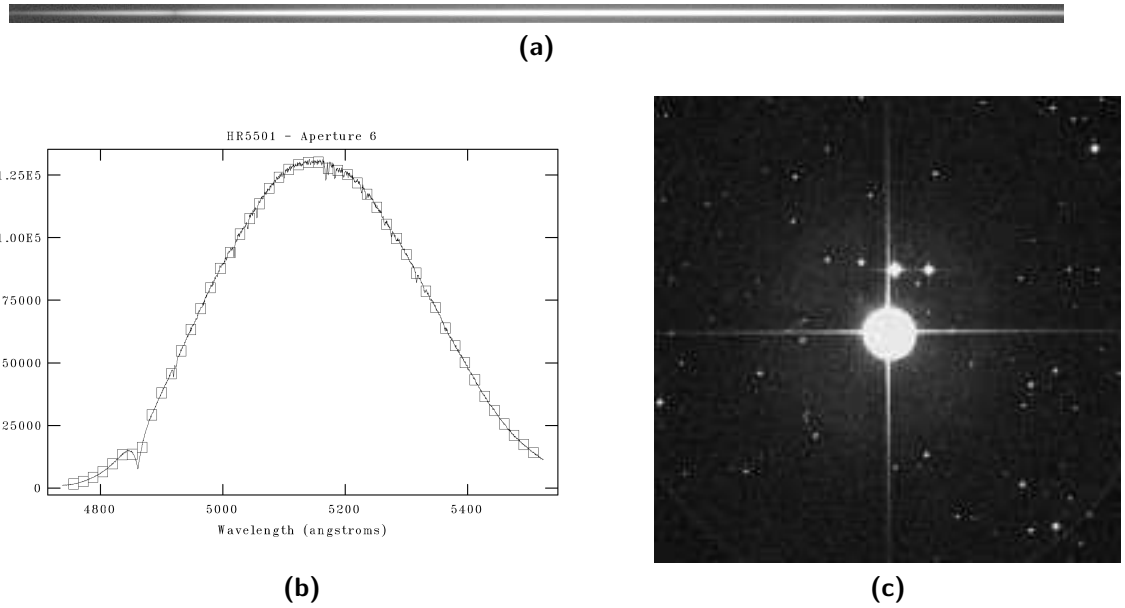

Figure 2.12: (a) HR5501 aperture 6 spectrum, (b) plot of the previous spectrum with the wavelength bins, (c) HR5501 (*ESO standard stars catalogue* 2015).

Fig. 2.14 there is the aperture 6 spectrum of one of the galaxies before and after the flux calibration.

2.4.7 Exposures Combination

The last step is combining the single exposures of each aperture for each galaxy, in order to obtain a single spectrum for each galaxy aperture. The combination has two purposes: the first is to increase the S/N ratio, the second is to remove all those small flaws called cosmic rays. Cosmic rays are energetic particles, not related with astronomical sources, which impact on the CCD creating narrow and well defined signal peaks randomly distributed on the whole image. Their number increases with the exposure time.

The best way to combine three or more spectra is to average them, rejecting too high or too low values compared to the average. However, my spectra, show too much flux difference between each other to be averaged so I preferred to sum up the exposures after I checked the perfect frames alignment. With this method the S/N ratio increases, but it does not remove the cosmic rays. To check the alignment of the images I used the `xregister` task, which compares the frames to the reference one and it calculate the possible shift. Once obtained the shift `imshift` allows to move the images of the right quantity to get the best alignment. After that I manually removed the cosmic rays with `imedit` (Fig. 2.15).

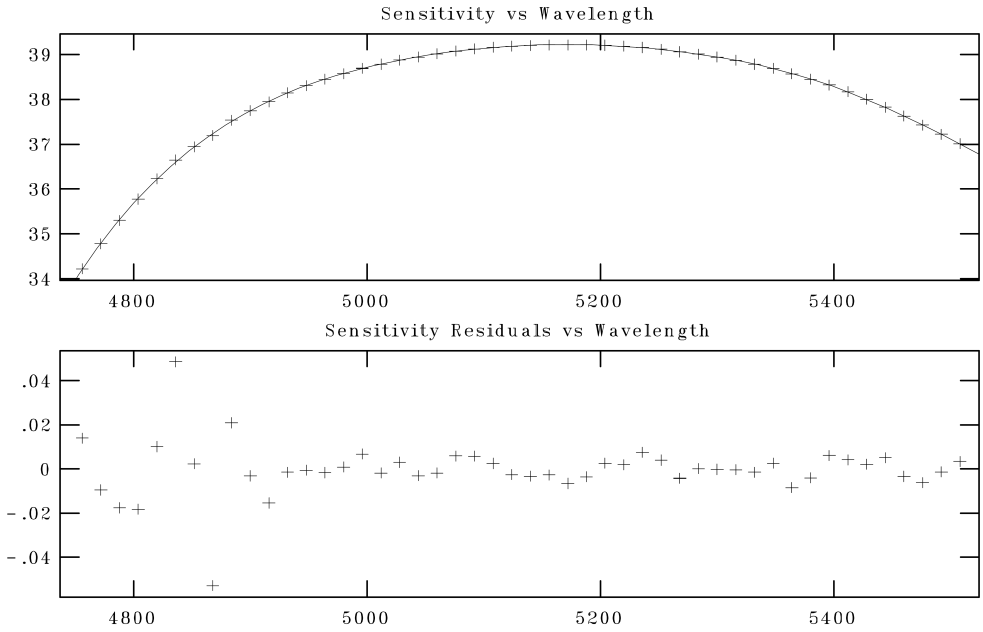

Figure 2.13: The top plot shows the final sensitivity function vs wavelength compared with the measured points, while in the bottom graphic there are the residuals as a function of the wavelength between the function and the measured points.

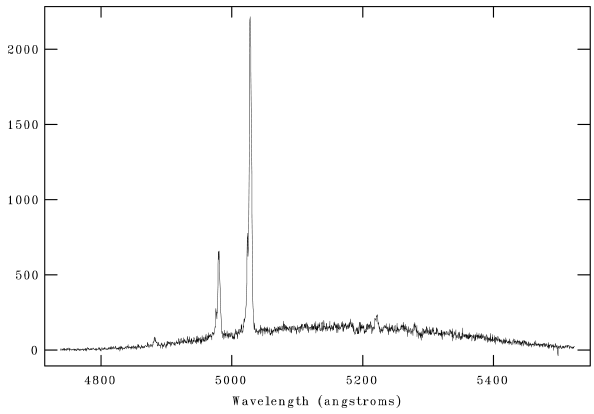

(a)

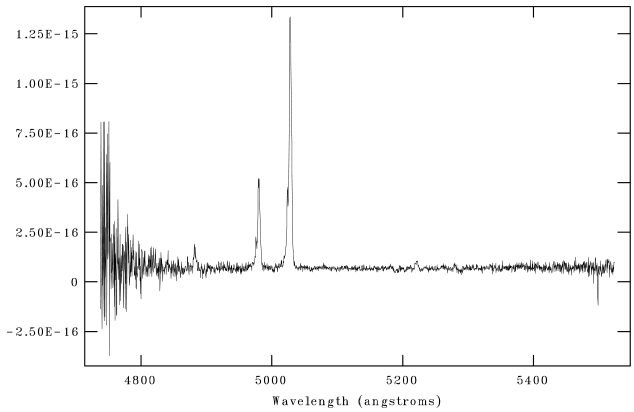

(b)

Figure 2.14: NGC5643 aperture 6 spectrum before (a) and after (b) flux calibration. The noise at the sides of the plot is due to the low sensibility at the extremes of the wavelength range, as shown in Fig. 2.13.

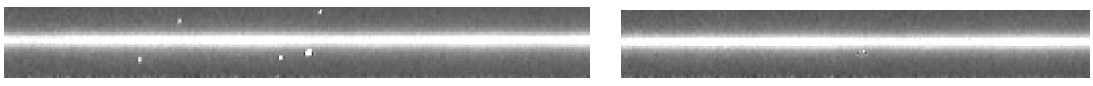

(a) **(b)**

Figure 2.15: The same spectrum section befor (a) and after (b) the cosmic ray removal.

Chapter 3

Data Preparation

The purpose of this work is to compare the profile of some of the brightest emission lines in the optical spectrum, in order to measure important physical parameters of the moving gas clouds as a function of their velocity. I will separate the spectrum of each galaxy in small regions and study the gas clouds in these regions. To this aim I need to extract a single one-dimensional spectrum which includes the entire wavelength range, for each considered region. Therefore, I am going to join all the aperture spectra, which must be perfectly aligned, otherwise the extracted 1D spectra would not correspond to the same region in all wavelength range and the following analysis will be completely wrong.

3.1 Straightening and Alignement

The first important point consists in making sure that the extracted 1D spectrum of a region includes all and only the emission of that region. The steps I need to carry out are two: the straightening of the spectra in the single aperture and the alignment of the different apertures spectra. First, I used again the `identify` task, this time along the spatial axis, to select in each galaxy the central peak, which I expect to be the nuclear emission. Then, `reidentify` automatically traces its position along the dispersion axis. Finally, `fitcoord` creates the function to be applied by `transform` to the different images in order to straighten them out.

Once straightened the spectra it is possible to align them, following the same process I used when I combined the spectra of the same aperture. With `xregister`, I measured the amount of shift of each frame with respect to a reference image, then I moved them with `imshift`, paying attention not to cut some useful regions. In Fig. 3.1, it is shown the difference between the original image and the processed one.

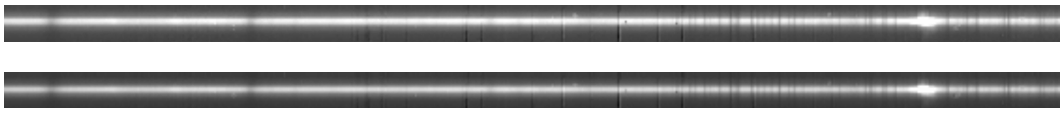

Figure 3.1: The aperture 1 spectrum of NGC5643 before (top) and after (bottom) the straightening and shift.

Table 3.1: Projected distances of the regions from the nucleus of the galaxy. I considered the emission peak near the center of the images as the nucleus of the galaxy and I measured the distances from this point to the middle point of each region. To calculate the distance of the galaxy from the redshift I used $H_0 = 70\,\mathrm{kms}^{-1}\mathrm{Mpc}^{-1}$.

	IC5063	NGC5643	NGC7212		IC5063	NGC5643	NGC7212
z[1]	0.01135	0.00399	0.02663	D (Mpc)	48.6	17.1	114.1
N2 (arcsec)	3.90	3.90	4.50	N2 (pc)	919	323	2489
N1 (arcsec)	2.55	2.70	3.00	N1 (pc)	601	224	1660
N0 (arcsec)	1.65	1.50	1.80	N0 (pc)	389	124	996
CN (arcsec)	0.60	0.45	0.60	CN (pc)	141	37	332
CS (arcsec)	0.60	0.45	0.60	CS (pc)	141	37	332
S0 (arcsec)	1.80	1.50	1.80	S0 (pc)	424	124	996
S1 (arcsec)	3.00	2.70	3.00	S1 (pc)	707	249	1660
S2 (arcsec)	4.50	3.90	4.50	S2 (pc)	1060	323	2489
S3 (arcsec)	-	5.10	-	S3 (pc)	-	423	-

[1] from NED

3.2 One-Dimensional Spectra

It is now possible to extract the 1D spectra from the two-dimensional ones. The first thing I had to do was to decide how to divide the galaxies in regions. It is essential to have a good, but not excessive, galaxy sampling. If I divided the galaxies in too many regions, some of the obtained spectra could be very noisy and impossible to use. I made the division object by object, considering Hα emission line and using `ds9` software to create some intensity contours in order to highlight its characteristics. In Fig. 3.2, it is possible to see the division steps, in Fig. 3.3 there is the complete division of the galaxies and in Fig. 3.4 there are the images of the slit, divided in regions, superimosed to the galaxies. Every Hα line shows some peculiar features so I divided the galaxies trying to have a good sampling of them. I decided to call the chosen regions following their arrangement from top to bottom of the images. I also divided the nuclear emission in two regions called *CN* and *CS*. In Tab. 3.1 I reported the distances of each region from the galaxy nucleus, measured in arcseconds and parsecs.

To extract the 1D spectra I used the `blkavg` task, which allows to sum or average image sections. In this case, I summed up the image section in order to obtain a 1D spectrum for each aperture region. At this point, I checked every single spectrum in order to see if they could be joined in the right way. When I saw relevant differences in flux I rescaled one of the images to match them perfectly. In this phase I also removed the noisy side of each 1D spectrum, but keeping a small wavelength interval in which each spectrum can be superimposed to the next ones. In this way they can be joined more smoothly. If the superimposed regions included strong emission lines I chose to remove one of them because I did not want to risk to alter the lines profile.

After that, I used the `scombine` task to connect all the spectra, getting the final 1D spectrum. The last step of this phase was to remove all of the small flaws due to sky subtraction and cosmic ray removal, which were not previously located. An example of the complete spectrum of the CN region of IC5063 is shown in Fig. 3.5.

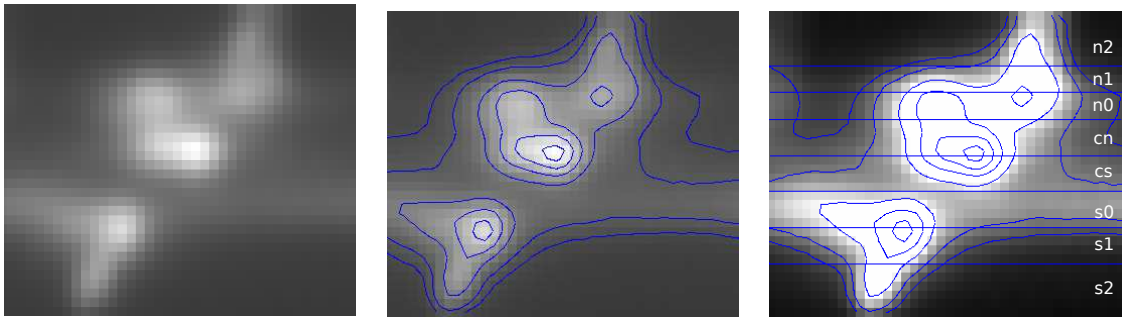

(a) (b) (c)

Figure 3.2: (a) IC5063 Hα emission line. It is possible to see that it is characterized by different peaks at various distances from the nucleus. (b) The same image with luminosity contours to highlight its features. (c) Regions subdivision.

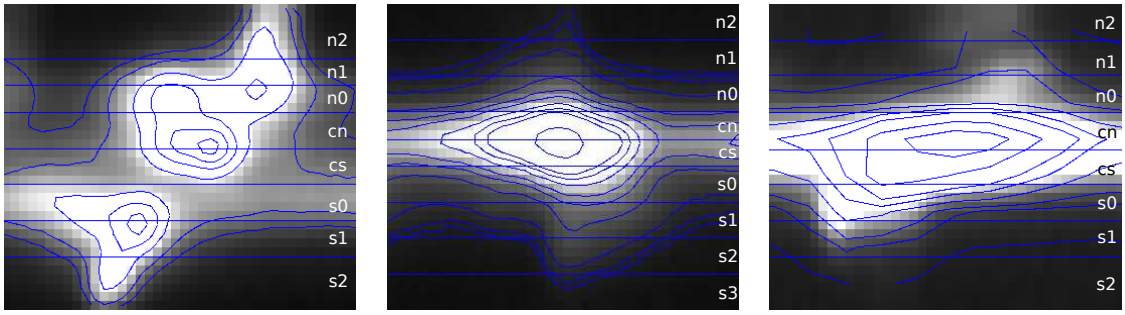

(a) (b) (c)

Figure 3.3: Images of the Hα emission line with contours and regions: (a) IC5063, (b) NGC5643, (c) NGC7212.

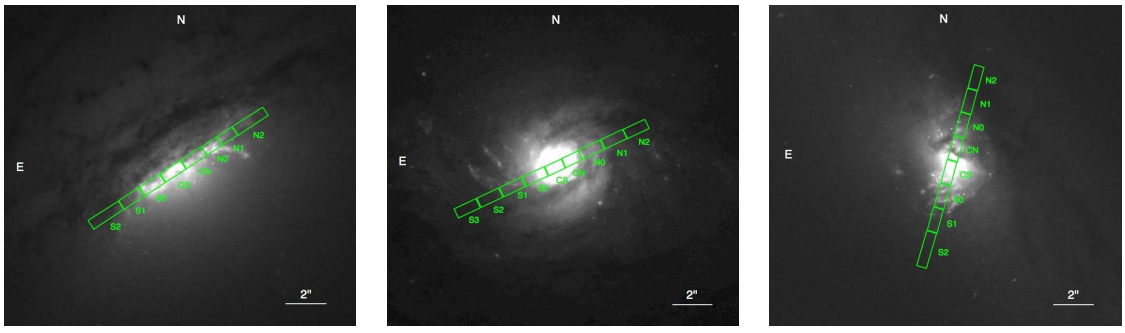

(a) (b) (c)

Figure 3.4: Images of the galaxies with the slit and the regions superimposed: (a) IC5063, (b) NGC5643, (c) NGC7212.

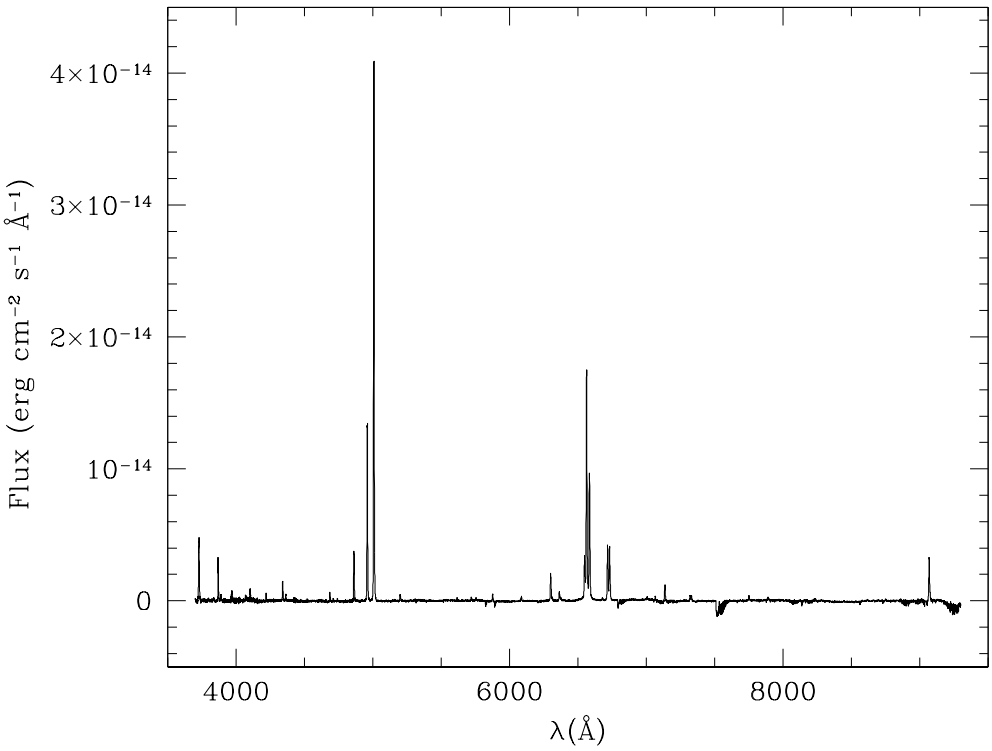

Figure 3.5: Complete spectrum of IC5063 CN region.

Table 3.2: V band absorption as reported on NED website.

Galaxy	IC5063	NGC5643	NGC7212
$A(V)$ (mag)	0.165	0.452	0.195

3.3 Subtraction of the Stellar Continuum

The subtraction of the stellar continuum probably is the most difficult step of this post-reduction process. One of the best methods to obtain a very reliable fit of the galaxy stellar continuum is to use STARLIGHT [1] (Cid Fernandes et al. 2005, Mateus et al. 2006, Cid Fernandes et al. 2007). STARLIGHT is a software developed to study the continuum emission in the SDSS (Sloan Digital Sky Survey) galaxy catalogue, and it can recreate the stellar continuum of a galaxy, starting from a sample of synthetic spectra. It can also give as output some of the main features of the galaxy stellar component: age and metallicity of the stellar populations present in the synthetic spectrum, stellar velocity and velocity dispersion and internal extinction.

As input, STARLIGHT needs spectra prepared in the following way. They have to be text files corrected for Galactic exctinction, they must be shifted to rest-frame wavelengths and they also must have a $1\,\text{Å}\,\text{px}^{-1}$ dispersion.

First, I corrected the spectra for Galactic extinction by means of the `deredden` task, which needs as input the spectra and the V band absorption (A(V)) (Tab. 3.2). I found the value for each galaxy, based on the papers by Schlegel, Finkbeiner, and Davis (1998) and Schlafly and Finkbeiner (2011), on NED website[2].

Then the galaxies spectra had to be shifted to rest-frame wavelengths. It is not easy to do very accurate redshift measures on these objects because the emission lines could be very broad and they can show multiple peaks, making it quite difficult to locate the center of the lines. For this reason, I tried to use some of the deepest stellar absorption lines as the Mg I triplet (λ5167, λ5177, λ5184) and the Na I doublet (λ5889, λ5895). In NGC7212 and in the most external regions of the other galaxies, I was forced to use Hβ or [O III]λ5007 emission lines, because the stellar continuum was too noisy to detect the absorption lines. The obtained value of the velocities are shown in Tab. 3.3. The measurements precision is only moderately relevant, because STARLIGHT will again calculate the velocity, but only if it is included in a $\pm 500\,\text{kms}^{-1}$ bin around $0\,\text{kms}^{-1}$ (Tab. 3.4). The software fine tuning is very important because I wanted to remove the velocity component due to galaxy rotation in order to study other kind of motions. In fact, at the end of subtraction, I will also correct the spectra for STARLIGHT velocities. The `newredshift` task easily allows to do the redshift corrections.

After that, I used the `dispcor` task to modify the spectra dispersion to a value of $1\,\text{Å}\,\text{px}^{-1}$ and `wspectext` to convert the images in text files.

Now the spectra are ready, but STARLIGHT needs some other files in order to work properly. The first thing to do is looking at the spectra for all those wavelength ranges which must not be considered when STARLIGHT will fit the stellar continuum, such as sky absorption lines, strong emission lines etc. I had to write in a text file the

[1] The STARLIGHT project is supported by the Brazilian agencies CNPq, CAPES and FAPESP and by the France-Brazil CAPES/Cofecub program.

[2] https://ned.ipac.caltech.edu/

Table 3.3: Recessional velocity (kms^{-1}) measured from emission or absorption lines.

Region	IC5063	NGC5643	NGC7212
S3	-	1235	-
S2	3347	1203	7788
S1	3359	1183	7711
S0	3367	1175	7737
CS	3364	1171	7916
CN	3421	1183	7988
N0	3417	1197	8052
N1	3442	1201	8114
N2	3445	1214	8074

Table 3.4: Velocity residuals (in kms^{-1}) measured from absorption lines and stellar continuum by STARLIGHT.

Regione	IC5063	NGC5643	NGC7212
S3	-	−48.56	-
S2	−25.0	−4.5	−211.4
S1	−75.3	10.1	169.3
S0	−56.3	16.5	132.9
CS	−36.5	17.3	−1.0
CN	−61.9	14.6	4.8
N0	−23.5	10.2	−9.5
N1	−46.9	6.9	−67.7
N2	−42.4	8.6	−21.5

spectral regions to be masked. Other important files are the configuration file and the `base` file. The first one contains a lot of information which could be modified. I mainly used it to decide how many iterations should have been done. The second file contains name and some data about the synthetic spectra which must be used by the software to fit the galaxies spectra. Between all of these spectra, STARLIGHT chooses by itself the needed ones. I used a `base` file with 45 spectra with age from 10^6 to $1.3\text{x}10^{13}$ yr and three metallicity: solar, sub-solar, super-solar. The last thing I had to prepare was another configuration file where I put the paths of the different configuration files, the wavelength range to be studied, the normalization wavelength, velocity and velocity dispersion guess, and the internal extinction law to be used by STARLIGHT to measure the internal exctinction of the galaxy stellar component.

The final output is a file that contains a short summary of the most important input data followed by:

- normalization value of the spectrum,
- average χ^2 and the percentage deviation of the synthetic spectrum from the observed one,
- measured velocity and velocity dispersion,
- list of the used stellar populations with a measurement of how much they contribute in the synthetic spectrum;
- input and syntetic spectrum with errors.

In Fig. 3.6 there is an example of the fitted spectra.

The synthetic spectra must now be converted again in `fits` files and they must be prepared to the subtraction. Basically I had to transform the txt files in `fits` images with `rspectext` and I brought back the dispersion to the original value. Then I finally subtracted the continuum to the spectra with `sarith`. At this point, it is possible to fine tune the redshift correction with the velocity measured by STARLIGHT.

In some cases, mainly in the external regions of the galaxies, the fitted spectrum was too different from the original one. When this happened, I tried to increase the stellar populations used to fit the data, from 45 to 130. If the output spectrum was still not good, I manually fitted the continuum with `splot`, using STARLIGHT only to measure the velocity.

3.4 Deblending

The Hα line, the [S II]$\lambda\lambda$6717, 6731 doublet and the [N II]$\lambda\lambda$6548, 6584 doublet are fundamental lines in studying the ionized gas. In the studied spectra, these lines are very broad and in most of the cases Hα and [N II]$\lambda\lambda$6548, 6584 are partially blended together and the same happens for the [S II] doublet. Hα is used in the diagnostic diagrams and to estimate the extinction, while the other doublets are needed to measure the density ([S II]) and for other diagnostic diagrams. Therefore, it is very important to deblend those lines. To separate Hα from the [N II] doublet, I followed the method suggested by Schirmer et al. (2013). They assumed that if Hα and Hβ are produced by the very same

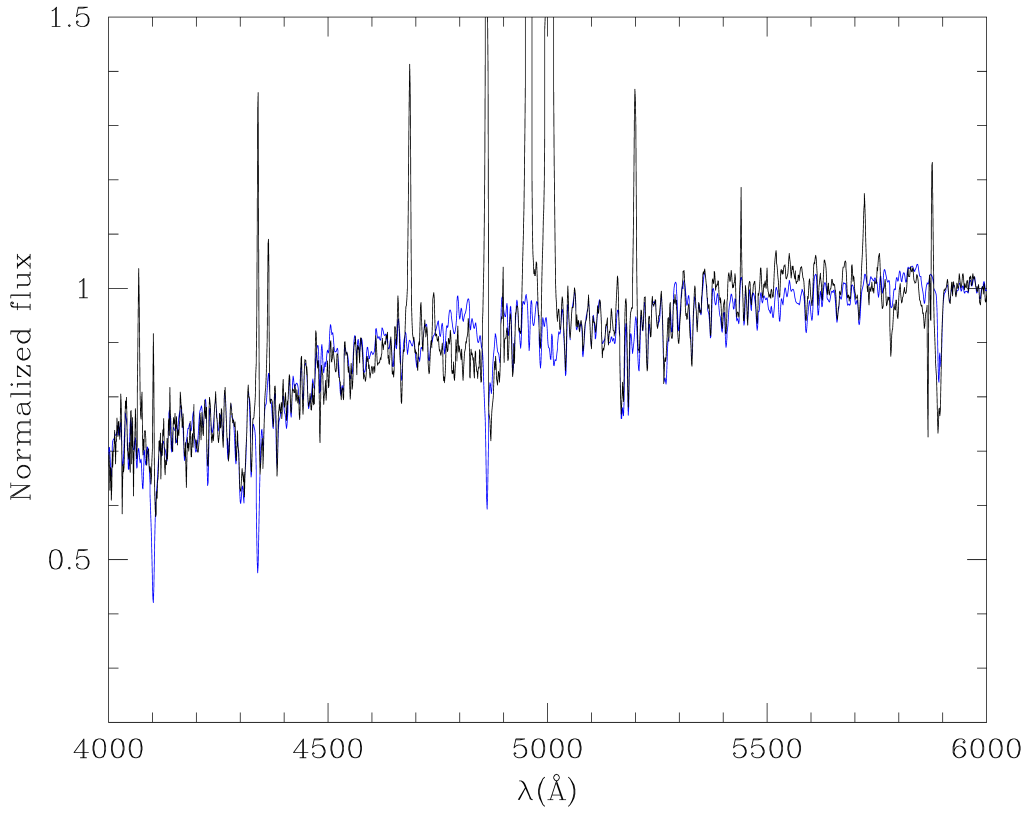

Figure 3.6: NGC5643 spectrum between 4100 and 6000 Å. The black spectrum is the original one, the blue spectrum is the model created by STARLIGHT. Both spectra are still normalized.

gas, they must have the same profile, except for extinction effects. Therefore, they took Hβ, multiplied it for a costant factor in order to match the Hα intensity peak, then they subtracted the multiplied Hβ from the Hα+[N II] group, obtaining an image with the only [N II] doublet. Subtracting the doublet from the original image they obtained also the Hα line. Schirmer et al. (2013) applied this process directly to the two-dimensional spectra, while I am working now with one-dimensional spectra. For this reason, I had to adjust the process for my purposes. I started shifting Hβ to the Hα wavelength, then I used the `ngaussfit` task to fit the line profile in the best way trying to use the less Gaussians as possible (Fig. 3.7 (a)) and modifying the values of the central intensity, the full width at half maximum (FWHM) and the central wavelength. Once I found the right solution, I used it to fit the Hα profile as well, keeping all the parameters fixed, except for the central intensity (Fig. 3.7 (b)). At this point the `function` task allows to transform the `ngaussfit` output in a `fits` image containing the model, which I subtracted to the original spectra, obtaining the [N II] doublet without the Hα line. There may be some residuals after the subtraction because of the different noise in the two lines. Besides, there could be some other residual structures due to small differences in the profiles of the two lines, because of the various extinction value which can affect the radiation coming from different clouds. I removed the residuals from the [N II] image, then I subtracted it from the original spectrum, in order to obtain the final Hα profile.

After that, I deblended the [S II] doublet. Here the question is more complex, because there is not any bright and isolated emission line which can be used as in the previous case ([O I]λ6300 is too weak and [O II]λ3727 is too noisy). Therefore, I tried to fit both lines together, using the same number of Gaussian functions. I paid attention to accurately fit the intersection region, trying to keep their profile similar. Once I found the best parameters combination, I continued in the same way as before: I created an image with one of the two fitted profiles, I subtracted it from the original spectrum, I removed the residuals from the obtained image and, again, I subtracted it to the original one. I finally obtained two files with the deblended [S II] lines. This deblending method is less reliable than the previous one, because there is not a line that can be used as a reference.

While I was deblending the [S II] doublet I noticed that it had an unusual shape in most of NGC7212 regions. It showed a profile with a lot of peaks and valleys (Fig. 3.9 (a)), which were not present in any other line neither in the same region, nor in the whole galaxy. Moreover, on the left side of the lines there was a small "hole", similar to the one produced by a sky absorption band. To confirm this, I superimposed with `splot` the band from the standard star spectrum, confirming my suspects. To remove the sky absorption and to obtain the real [S II] profile, I followed these steps: first, I subtracted the stellar continuum from the standard spectrum, then I shifted it in order to have its sky absorption at the same wavelength of that in the galaxy spectrum, I rescaled it and finally I subtracted the standard spectrum to the galaxy one. There is a problem with rescaling the standard spectrum. The transport equation 3.1 (for absorption only) states that, if I_ν is the specific intensity, when the radiation passes through a gas cloud with dimension s (like the atmosphere), its variation is proportional to the specific intensity itself. Consequently the absorption is stronger in the lines than in the continuum near the doublet.

$$\frac{dI_\nu}{ds} = -k_\nu I_\nu \tag{3.1}$$

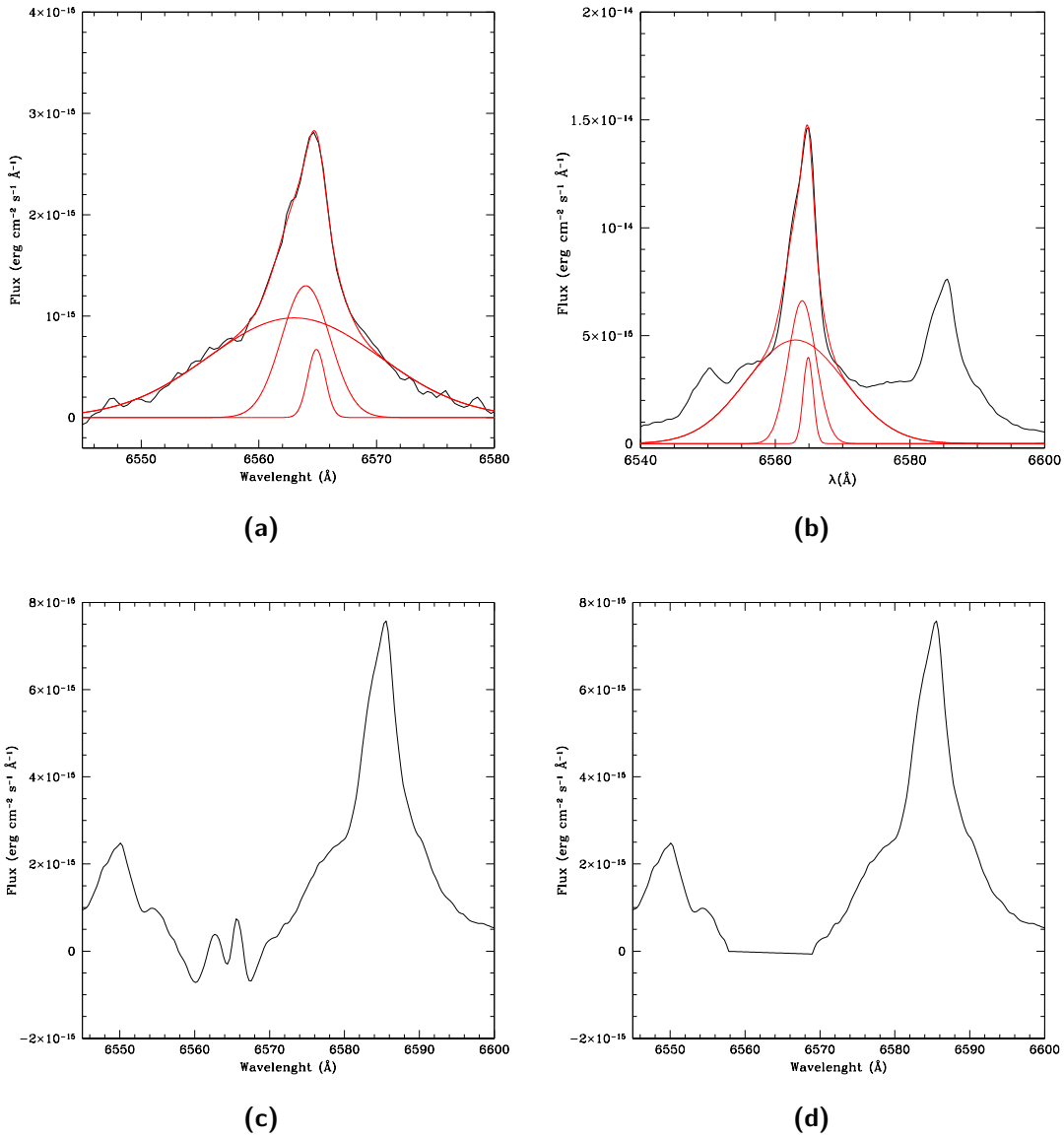

Figure 3.7: (a)Hβ shifted to Hα wavelength and (b) Hα fit for the IC5063 CS region. (c) The [N II]$\lambda\lambda$6548, 6584 after the fit subtraction and (d) after I removed the residuals.

Therefore, in order to totally remove the absorption from the lines, I separated the absorption band in two sections and I rescaled them separately, trying to reproduce the profile of the other emission lines of the same spectrum. The correction results can be seen in Fig. 3.9.

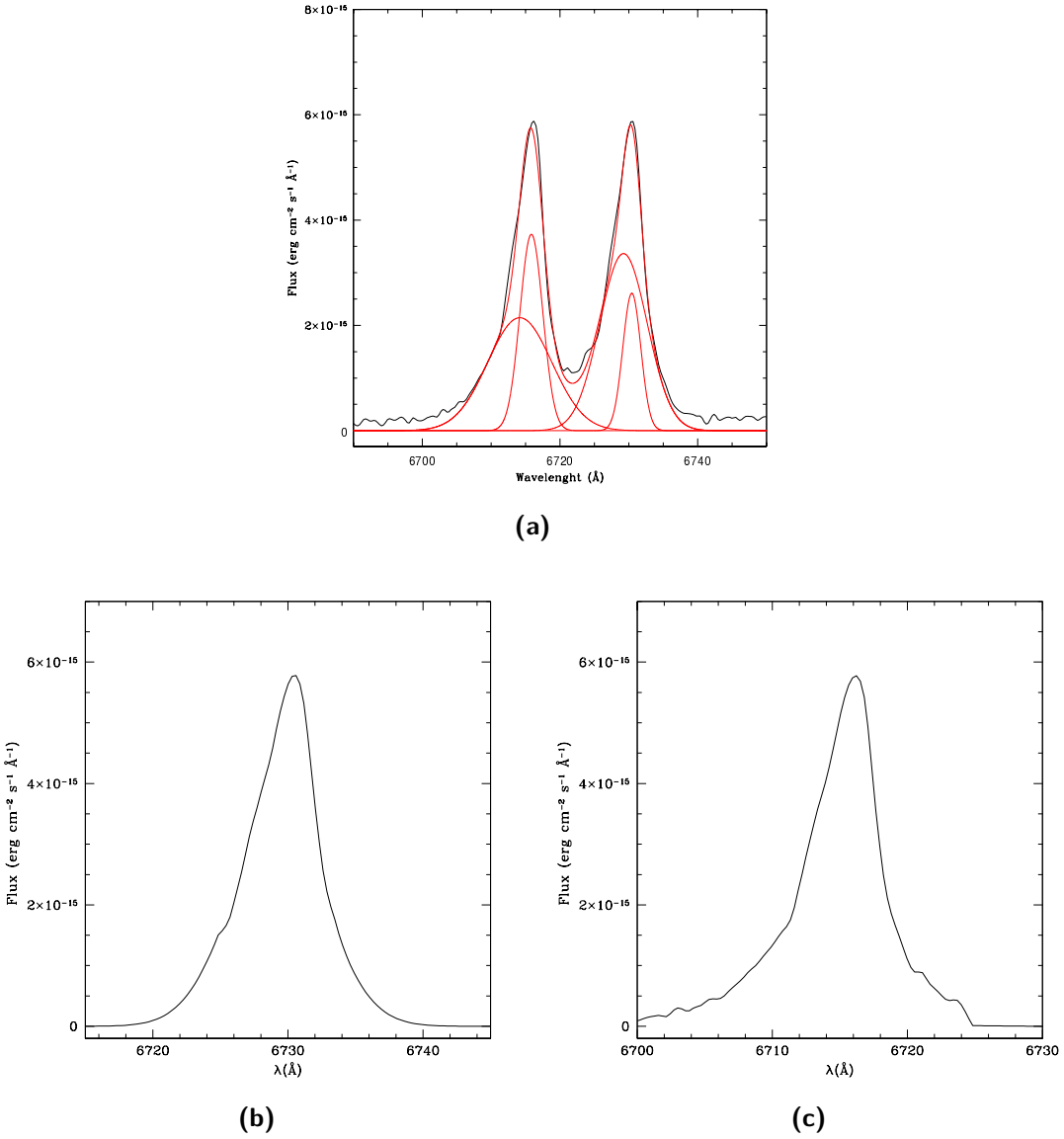

Figure 3.8: (a)[S II] doublet fit for the N0 region of NGC5063. (b) [S II]λ6717 line and (c) [S II]λ6731 line of the same region after the deblending.

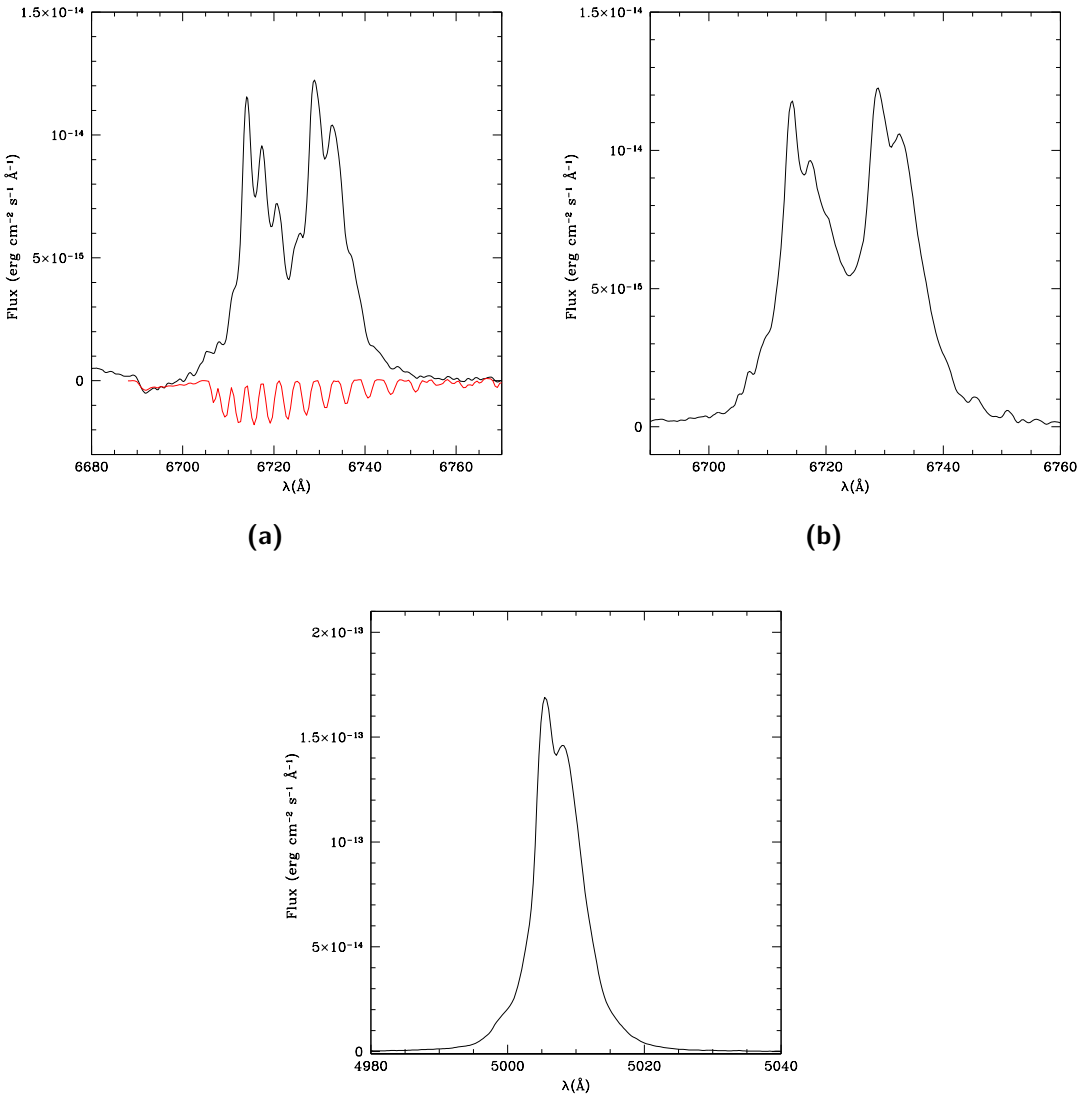

Figure 3.9: (a)The [S II] doublet from region CS of NGC7212 (in black) with the sky absorption band from HR5501 spectrum (in red). (b) The same doublet after the correction. The two remaining peaks are present in all of the other lines of the spectrum, like [O III]λ5007 (c).

Chapter 4

Data Analysis

Once I prepared the final spectra for measurements, I could start the data analysis. The first thing I did was to measure the line fluxes. After that, I corrected all of the fluxes for internal extinction, then I normalized the corrected values to the Hβ flux. The third step was to select the useful diagnostic diagrams and to calculate the lines ratios needed to plot them. Then, I also measured the ionization parameter U which indicates the gas ionization degree. Last but not least, I also calculated the average temperature and electron density of the regions.

4.1 Measurements

The deblending process was the last step of the post-reduction process. Now the spectra are ready to be analysed. As I previously said, in this work I am going to measure some of the main gas properties, and to compare the profiles of the most important emission lines. If a moving cloud emits a spectral line at $\lambda = \lambda_e$, an observer in any other inertial reference frame will see its emission at a wavelength λ_o, which is linked to the original λ_e via the radial velocity difference between the cloud and the observer (eq. 4.1). This is the so called Doppler effect.

$$\frac{\lambda_o - \lambda_e}{\lambda_e} = \frac{v}{c} \tag{4.1}$$

For this reason, if a cloud is moving toward the observer its radiation will be seen *blue-shifted*, while if it is moving in the opposite direction it will be seen *red-shifted*. In case of several moving clouds not spatially resolved, the observed spectral line will be the sum of the single lines and it will become broader. If the spectral resolution of the observing instrument is adequate, its profile will show some features, like multiple peaks, bumps or asymmetries (Fig. 4.1 (a)).

In Sec. 1.4, I showed how the ENLR can have a quite complex kinematics, so I expect to find broaden lines, not as much as BLR lines but broader than normal H II regions lines. Some of the studied emission lines showed base widths larger than 1000 $\mathrm{km s^{-1}}$ (Fig. 4.1 (b)).

It is possible to study how the different gas properties depend on the velocity and on the analysed region, dividing every line of each region in low velocity bins and measuring the flux inside them, as done by Ozaki (2009). There are two ways to divide

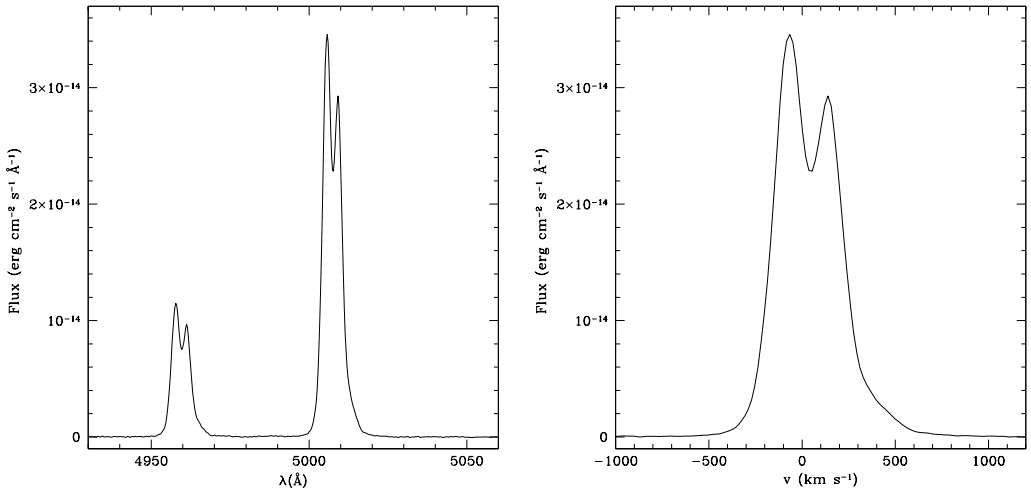

Figure 4.1: (a)[O III]$\lambda\lambda$4959, 5007 emission lines profiles in the N0 region of IC5063. It is easy to notice the presence of two peaks for each lines due to the emission of gas in motion with a different velocity. (b)[O III]λ5007 profile. In the x-axis is showed the velocity, calculated with eq. 4.1 considering $\lambda_e = 5006.8\,\text{Å}$.

the lines. The first one is to follow Ozaki's method and study the properties of a strong line for each region and to divide it, alongside with the other lines, following its features. The second one is to divide the line in fixed velocity bins. The advantages, with the latter method, are that the division is less arbitrary and it is easier to manage a large quantity of data. For these reasons, I decided to follow the second method and I divided the lines into $100\,\text{kms}^{-1}$ bins which is about three times the theoretical instrumental velocity resolution ($\text{R} \simeq 37.5\,\text{kms}^{-1}$).

I developed an IRAF script for this purpose. An IRAF script is a list of instructions which IRAF can automatically carry on. The script requires only the name of the file on which the measure has to be done and the rest wavelength of the lines to be measured. It automatically divides the lines in the required bins and it uses the `sbands` task to measure the flux inside every bin. I decided to measure IC5067 and NGC7212 lines from -700 to $700\,\text{kms}^{-1}$ and NGC5643 lines from -700 to $500\,\text{kms}^{-1}$, because they were narrower. In this way it was possible to obtain all of the measurements easily and quickly.

In Tab. 4.1 all of the measured emission lines, needed in order to estimate the fundamental physical parameters, are listed. Unfortunately, [O III]λ4363 line and the [Ar IV]$\lambda\lambda$4711, 4740 doublet, needed to measure temperature and density of high-ionization gas, and the [O II]$\lambda\lambda$7319, 7330, which are used to measure the low-ionization gas temperature, are too faint to be divided in velocity bins, so I measured their total fluxes and I used them to calculate the average temperature and density for each region. Furthermore, the S/N ratio in the S3 and N2 regions of NGC5643 and in the S2 region of NGC7212 was too low to analyse the emission lines, so I decide to not continue the study of these spectra.

Table 4.1: Measured emission lines and ionization potential of the ions.

Ion	Wavelength (Å)	Ionization potential (eV)
[O II]	3727	13.6
[O III]	4363	35.1
[Ar IV]	4711	40.9
[Ar IV]	4740	40.9
Hβ	4861	-
[O III]	4959	35.1
[O III]	5007	35.1
[O I]	6300	-
Hα	6563	-
[N II]	6584	14.5
[S II]	6717	10.4
[S II]	6731	10.4
[O II]	7319	13.6
[O II]	7330	13.6

4.2 Extinction Correction

The ISM is composed by two elements: gas and dust. Even if dust is a minor component of the ISM in mass, it is very important because it is really efficient in absorbing the incoming radiation and in re-emitting it at longer wavelengths. The spectrum of an ENLR gaseous nebula will be absorbed by the Milky Way dust and by the dust of the ENLR itself. I already corrected the spectra for Galactic extinction before the continuum subtraction, because this is a specified requirement of STARLIGHT, so it lasts to be considered only the inner extinction.

The dust absorption is not costant at all wavelengths, but it is stronger in the blue region of the spectrum and weaker in the red one. In the wavelengths range from $0.125 - 3.5\,\mu$m, this behaviour is well described by an empirical law deduced by Cardelli, Clayton, and Mathis (1989) (Fig. 4.2). This function depends only on the ratio between the total extinction and the selective extinction $R(V) = A(V)/E(B-V)$. A typical value for this ratio is 3.1. When $A(V)$ is known, it is possible to measure the extinction at each wavelength with the equation 4.2, where y is defined as $y = 1/\lambda - 1.82$ (with λ measured in µm) and $a(y)$ and $b(y)$ are the two polynomials in eq. 4.3, 4.4.

$$A(\lambda) = A(V) \cdot \left(a(y) + \frac{b(y)}{R(V)} \right) \tag{4.2}$$

$$a(y) = 1 + 0.17699 \cdot y - 0.50447 \cdot y^2 - 0.02427 \cdot y^3 + 0.72085 \cdot y^4 + 0.01979 \cdot y^5 - 0.77530 \cdot y^6 + 0.32999 \cdot y^7 \tag{4.3}$$

$$b(y) = 1.41338 \cdot y + 2.28305 \cdot y^2 + 1.07233 \cdot y^3 - 5.38434 \cdot y^4 - 0.62251 \cdot y^5 + 5.30260 \cdot y^6 - 2.09002 \cdot y^7 \tag{4.4}$$

$A(V)$ is estimated from the ratio between two lines, whose theoretical value is known. The equation 4.5, where $\frac{I(\lambda_1)}{I(\lambda_2)}$ is the theoretical ratio and $\frac{F(\lambda_1)}{F(\lambda_2)}$ is the observed one, must be inverted and A_{λ_1} and A_{λ_2} must be expressed with eq. 4.2.

$$\frac{I(\lambda_1)}{I(\lambda_2)} = \frac{F(\lambda_1)}{F(\lambda_2)} \cdot 10^{0.4 \cdot (A_{\lambda_1} - A_{\lambda_2})} \tag{4.5}$$

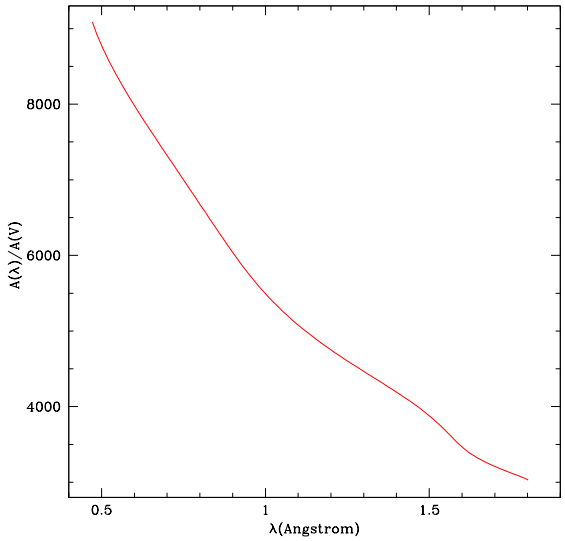

Figure 4.2: Extinction function from Cardelli, Clayton, and Mathis (1989) for the optical band of the spectrum.

A typical ratio used for this purpose is the Hα/Hβ ratio which, for temperature of about 10^4 K and low density, depends only on the extinction. The terms involved in this calculation are:

$$a(\mathrm{H}\alpha) = 0.9088 \quad b(\mathrm{H}\alpha) = -0.2823 \quad A(\mathrm{H}\alpha) = 0.8177A(V)$$

$$a(\mathrm{H}\beta) = 1.0154 \quad b(\mathrm{H}\beta) = 0.4613 \quad A(\mathrm{H}\beta) = 1.1642A(V)$$

$$\frac{I(\mathrm{H}\alpha)}{I(\mathrm{H}\beta)} = 2.86$$

With this method I extimated the extinction in almost all of the velocity bins, where I could measure Hβ, then I corrected all fluxes. Sometimes, in high velocity bins, the calculated $A(V)$ was negative, because the Hα/Hβ ratio was smaller than 2.86, due to the small S/N ratio in the lines wings. In order to continue the analysis without losing the information at those velocities, I decided to set, in these cases, $A(V) = 0$.

I also measured the average $A(V)$ using the total lines fluxes to calculate Hα/Hβ ratio, in order to correct the lines used to measure temperature and density because, as I said before, some of them were too faint to be reasonably divided in velocity bins. In Tab. 4.2 there are all of the so-obtained values for every regions of each galaxy, but I will discuss them in the next chapter.

Finally the emission line correction can be done via the eq. 4.6, where $c_\lambda = \left(a(y) + \frac{b(y)}{R(V)}\right)$.

$$I(\lambda) = F(\lambda) \cdot 10^{0.4 \cdot A(V) \cdot c_\lambda} \tag{4.6}$$

4.3 Diagnostic Diagrams

A gaseous nebula can be ionized by means of different mechanisms. The principal ones are:

Table 4.2: Average $A(V)$ values obtained for each galaxy region.

Regione	IC5063	NGC5643	NGC7212
S2	1.84	1.34	-
S1	1.90	1.03	0.32
S0	2.16	1.33	0.86
CS	2.89	2.06	1.64
CN	2.21	2.13	1.61
N0	1.58	1.14	1.55
N1	1.47	2.37	0.95
N2	1.33	-	1.63

- photoionization by hot main sequence stars (O, B), the main ionization mechanism present in normal H II regions;
- photoionization by very hot highly evolved stars, like white dwarfs, which are the main source of ionizing radiation in planetary nebulae;
- photoionization by a power law continuum, which is the typical mechanism in BLR and NLR of AGN;
- ionization by shock-waves, which is especially active in supernova remnants.

To fully understand the main properties of ionized gas it is very important to indentify which of the previously mentioned ionization mechanism is at work. It is possible to directly investigate the main excitation mechanism of a gas cloud with the help of emission lines ratios. Not all ratios are good but Veilleux and Osterbrock (1987) suggested in their paper some useful selection criteria to choose the best lines ratios:

- the involved lines must be easily measurable;
- they must not be too close to each other, because the deblending process could influence the final results;
- they must not be too distant, because in this case the extintion correction could influence the results;
- lines ratios involving a forbidden line and a Balmer line should be preferred because they are less sensitive to the gas metallicity.

Following these suggestions, several diagnostic ratios were studied in literature, but the most used are those defined by Baldwin, Phillips, and Terlevich (1981). Diagrams obtained with these ratios are commonly called BPT diagrams. In this work, I used three easily measurable line ratios which were able to discern between thermal photoionization and non-thermal photoionization ([N II]λ6584/Hα, [S II]$\lambda\lambda$6717, 6731/Hα, [O I]λ6300/Hα) and one ratio ([O III]λ5007/Hβ) particular sensitive to the gas ionization degree. Veilleux and Osterbrock (1987) claimed that [O I]λ6300/Hα is the best ratio to discern the ionization mechanism, unfortunately it has the flaw that the oxygen line is often weak respect to all of the other involved lines. Nevertheless, I used it because

I could easily measure the [O I]λ6300 in all of the spectra and because the other two ratios could be influenced by the deblending process. However, it is possible to see in Fig. 4.3 (a), (b), (c) that they agree in identifying the gas emission in all of the velocity bins of the region as ionized by a power law continuum. In these three plots, I used the empirical functions described in Kewley et al. (2001) to divide the H II regions section of the plots from the one occupied by all of the other regions. Kewley et al. (2001) used some simulation to verify which section of each diagram is occupied by region ionized by different mechanisms. They found tree functions that can reliably discern the gaseous regions ionized by a thermal continuum, which are located in the bottom-left corner of the diagrams, from regions ionized by other mechanisms, which occupy the remaining part of the graphics.

I also used another diagnostic diagram described in Baldwin, Phillips, and Terlevich (1981) the ΔE vs [O II]λ3727/[O III]λ5007. This diagram was an attempt to combine all of the other diagrams in a single one, by means of some quantities $\Delta(\lambda 1/\lambda 2)$ which are defined in eq. 4.7, 4.8 and 4.9. Those quantities are called *excitation differences* and were obtained by Baldwin, Phillips, and Terlevich (1981) subtracting the results of some simulations about the H II region gas to the measured data. Combining the obtained values for each excitation difference, they created a final marker called ΔE (eq. 4.10). By plotting this quantity versus [O II]λ3727/[O III]λ5007, it is possible to separate H II regions, which are located near $\Delta E = 0 \pm 0.2$, from regions ionized by other mechanisms, which have higher ΔE values. They also empirically showed that shock-ionized regions have [O II]λ3727/[O III]λ5007 > 0 and power-law photoionized regions have [O II]λ3727/[O III]λ5007 < 0.

$$\Delta E\left(\frac{[\mathrm{O\,III}]5007}{\mathrm{H}\beta}\right) = \log\left(\frac{[\mathrm{O\,III}]5007}{\mathrm{H}\beta}\right) + \log(0.32 + x) - 0.44 \tag{4.7}$$

$$\Delta E\left(\frac{[\mathrm{N\,II}]6584}{\mathrm{H}\alpha}\right) = \frac{1}{2}\left(\log\left(\frac{[\mathrm{N\,II}]6584}{\mathrm{H}\alpha}\right) - \log\left(\frac{x}{x + 1.93}\right) + 0.37\right) \tag{4.8}$$

$$\Delta E\left(\frac{[\mathrm{O\,I}]6300}{\mathrm{H}\alpha}\right) = \frac{1}{5}\left(\log\left(\frac{[\mathrm{O\,I}]6300}{\mathrm{H}\alpha}\right) + 2.23\right) \tag{4.9}$$

$$\Delta E = \frac{1}{3}\left(\Delta E\left(\frac{[\mathrm{O\,III}]5007}{\mathrm{H}\beta}\right) + \Delta E\left(\frac{[\mathrm{N\,II}]6584}{\mathrm{H}\alpha}\right) + \Delta E\left(\frac{[\mathrm{O\,I}]6300}{\mathrm{H}\alpha}\right)\right) \tag{4.10}$$

4.4 Ionization Parameter

The *ionization parameter* is an adimensional quantity, which measures the gas ionization degree. For an isotropic radiation source it is defined as:

$$U = \frac{Q}{4\pi r^2 c n_e} \tag{4.11}$$

where Q is the total number of ionizing photons emitted by the source for unit time, r is the distance of the gaseous cloud from the source and n_e is the electron density. In order to measure U it is possible to use some lines ratios which must not depend on

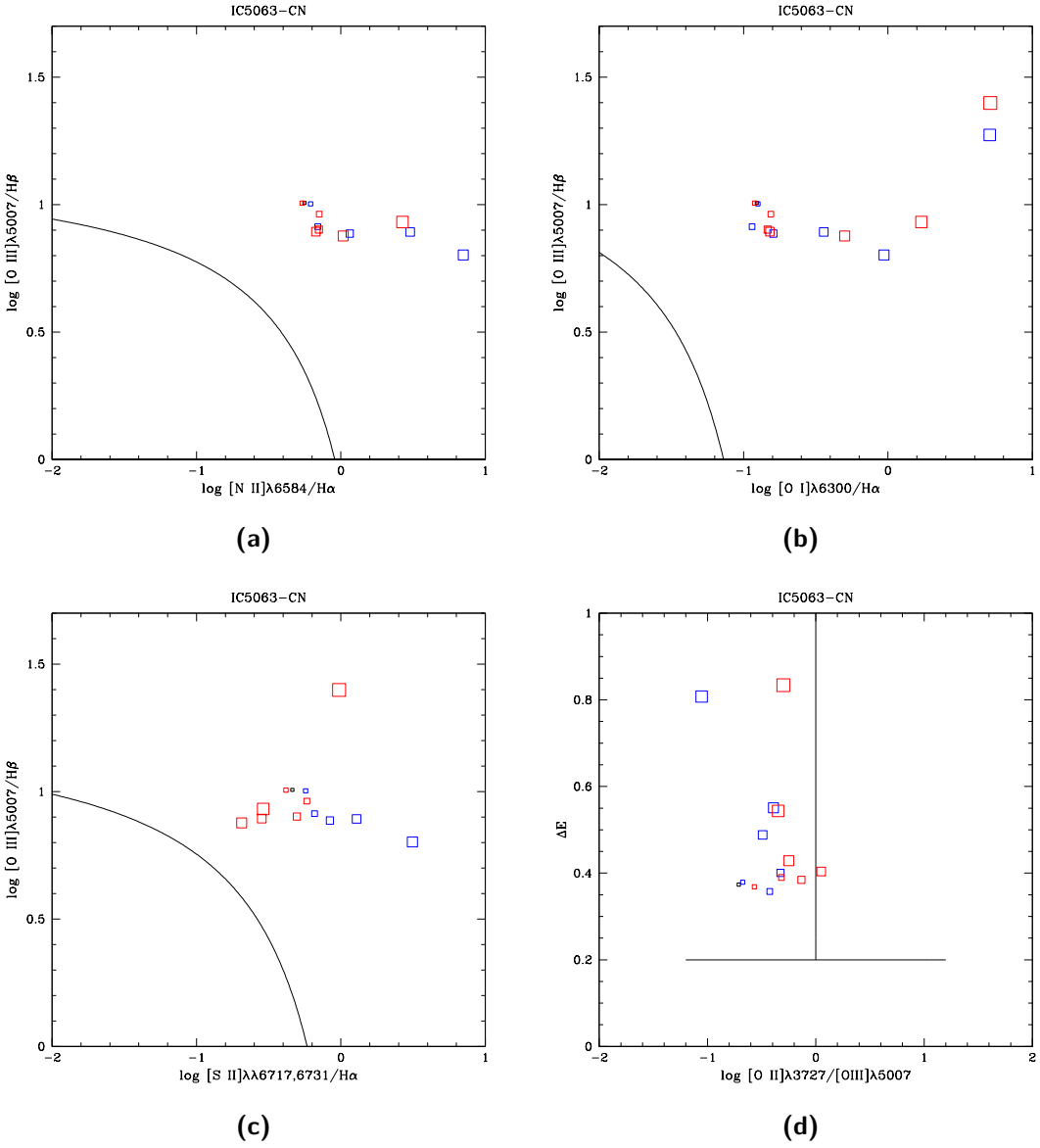

Figure 4.3: (a)[N II]λ6584/Hα vs [O III]λ5007/Hβ (b) [O I]λ6300/Hα vs [O III]λ5007/Hβ (c) [S II]$\lambda\lambda$6717, 6731/Hα vs [O III]λ5007/Hβ diagnostic diagrams for the CN region of IC5063. The black lines are the empirical separation between H II regions and other regions from Kewley et al. (2001). (d) ΔE vs [O II]λ3727/[O III]λ5007 diagnostic diagram for the same region. The vertical line divides the power-law ionized regions (on the left) and the shock ionized ones (on the right). The horizontal line divides the H II regions from the others. In all diagrams, red squares represent bins with $v > 0$, blue squares data with $v < 0$ and the black ones are for $v = 0$. Bigger squares correspond to higher velocities.

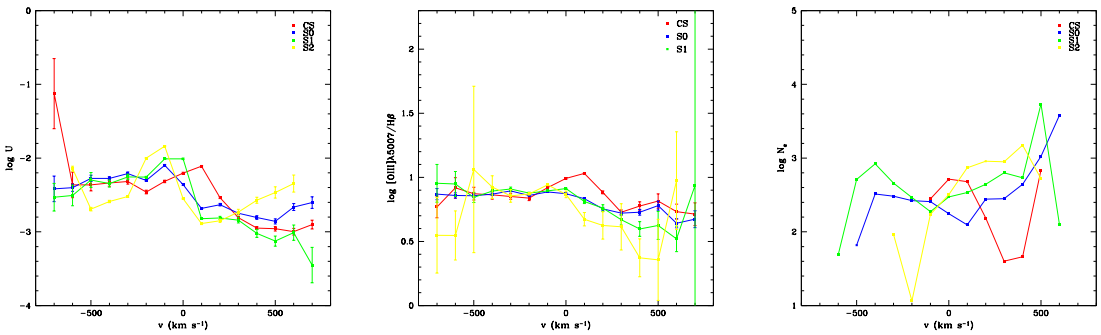

(a) (b) (c)

Figure 4.4: (a) log$U$ vs v, (b) [O III]λ5007/Hβ vs v, (c) N_e vs v diagrams of IC5063 south regions.

density and chemical abundances. The best ratio is [O II]λ3727/[O III]λ5007 (Penston et al. 1990) and its empirical relation with U is expressed by eq. 4.12.

$$\log U = -2.74 - \log\left(\frac{[\mathrm{O\,II}]\lambda 3727}{[\mathrm{O\,III}]\lambda 5007}\right) \tag{4.12}$$

The main problem of [O II]λ3727/[O III]λ5007 is that this ratio strongly depends on the extinction correction. For this reason it is useful to compare the U vs v plot with a similar plot involving [O III]λ5007/Hβ (Fig. 4.4 (a), (b)) which, even if it is not a real ionization parameter, it is quite sensitive to the gas ionization degree and it has the advantage not to depend on the extinction correction, because the two involved lines are close in wavelengths. If the two diagrams are compatible, it means that the U vs v plot is not affected by extinction.

In a paper by Ozaki (2009) about NGC1068, she found that U increases with the velocity. She suggested that this behaviour could be linked to the radiation pressure, because when an optically thick cloud is accelerated, the acceleration is proportional to the ionization parameter itself. She supposed that the ENLR clouds are located inside bigger clouds of absorbing matter. The clouds located in the more dense regions are less accelerated because the ionizing source radiation is strongly absorbed and obviously the ionization parameter is lower, because there are less ionizing photons. On the other hand high velocity clouds see a less absorbed radiation so the radiation pressure is stronger and the number of ionizing photon is higher.

Furthermore U is expected to decrease with the increasing of the cloud distance from the ionizing source (the central AGN) (eq. 4.11,Ozaki 2009); if this does not happen and U remains almost constant, it means that other ionization mechanisms should be at work. All of these arguments will be further discussed in the following chapter.

4.5 Temperature and Electron Density

The last gas properties I tried to measure are temperature and electron density. Most of the needed lines were weak, so I could not calculate these quantities in all of the velocity bins. Therefore, I tried to measure the average values for the regions

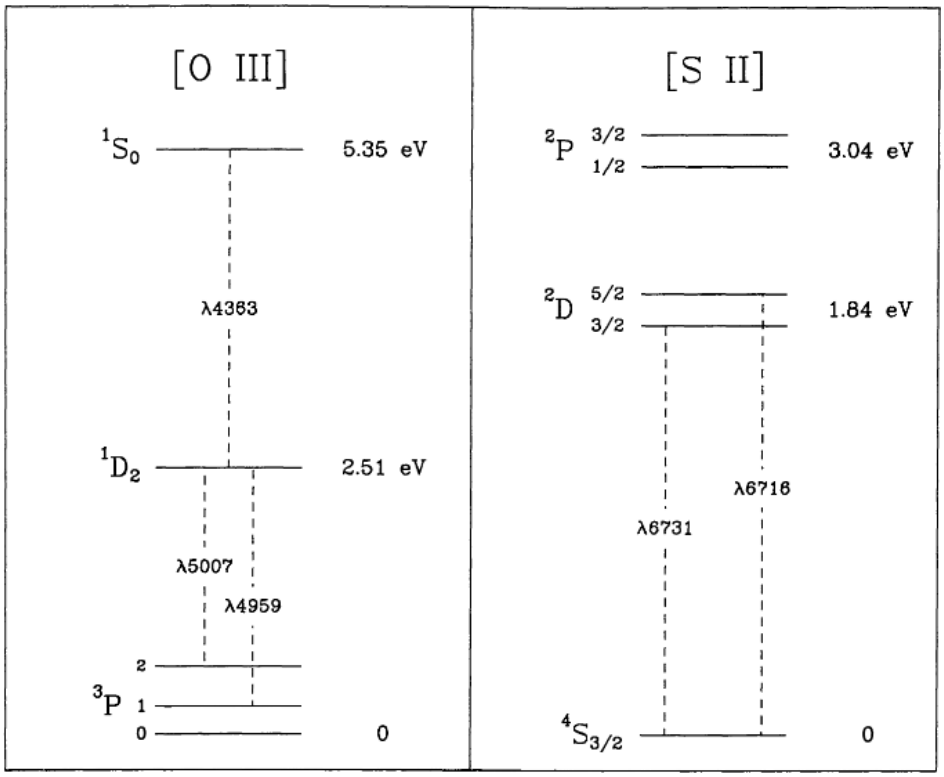

Figure 4.5: The Grotriam diagrams of [O III] and [S II] lines from De Robertis, Dufour, and Hunt (1987).

where I could detect all of the needed lines. Fig. 4.5 shows the Grotrian diagrams for the [O III] lines and [S II] lines, the most used ones to measure temperature and density. For the electron density it is necessary a doublet with very close lines. In this way the excitation potential of the lines is almost the same, but they have a different collisional excitation rate. The lines used to measure the temperature come from a three level system where the gas temperature defines the populations of the upper levels through the Boltzmann equation (eq. 4.13) where N_{i+1} e N_i are the number densities of the excited atoms at levels $i+1$ and i, g_{i+1} and g_i are the statistical weights, $hv_{i,i+1}$ is the energy difference between the two levels, k is the Boltzmann constant and T is the electron temperature. It is possible to measure temperature and electron density of gas with different ionization degrees with the correct choice of lines ratios. For the low ionization gas, [O II]λ3727 and [O II]$\lambda\lambda$7320, 7330 lines are used for the temperature, while [S II]$\lambda\lambda$6717, 6731 lines, for density. In case of high ionization gas, the useful lines are [O III]$\lambda\lambda$4959, 5007 and [O III]λ4363 for temperature, and [Ar IV]$\lambda\lambda$4711, 4740 for density. The ionization potentials for these lines are shown in Tab. 4.3. The critical lines, as I said before, are [Ar IV] and [O III]λ4363 which are, unfortunately, very weak in all of the regions (Fig. 4.6), and [O II]$\lambda\lambda$7320, 7330 which are stronger but blended together, in such a way that it is not possible to easily separate them as I did with the [S II] doublet (Fig. 4.7).

$$\frac{N_{i+1}}{N_i} = \frac{g_{i+1}}{g_i} \exp\left(hv_{i,i+1}/kT\right) \tag{4.13}$$

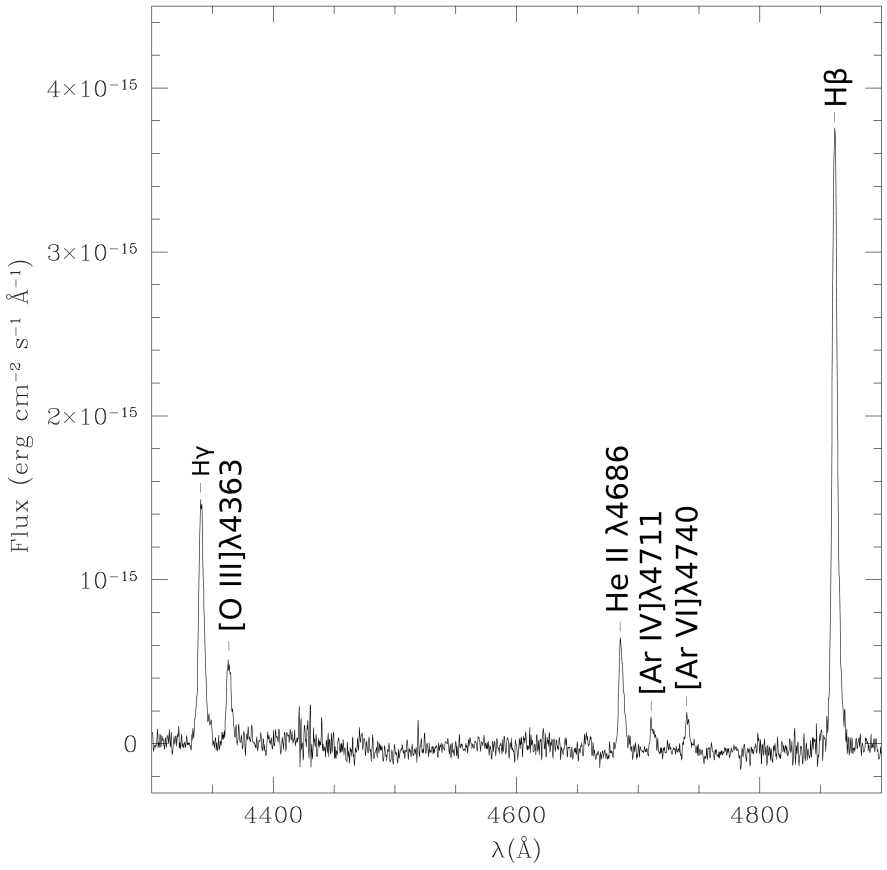

Figure 4.6: The spectrum between 4300 and 4900 Å in the CN region of IC5063. The second line on the left is the [O III]λ4363 line, the two small lines on the right are the [Ar IV]$\lambda\lambda$4711, 4740 doublet. It is possible to see that these lines are too weak, compared with Hβ (the first line on the right), to be divided in velocity bins, also in this high S/N spectrum.

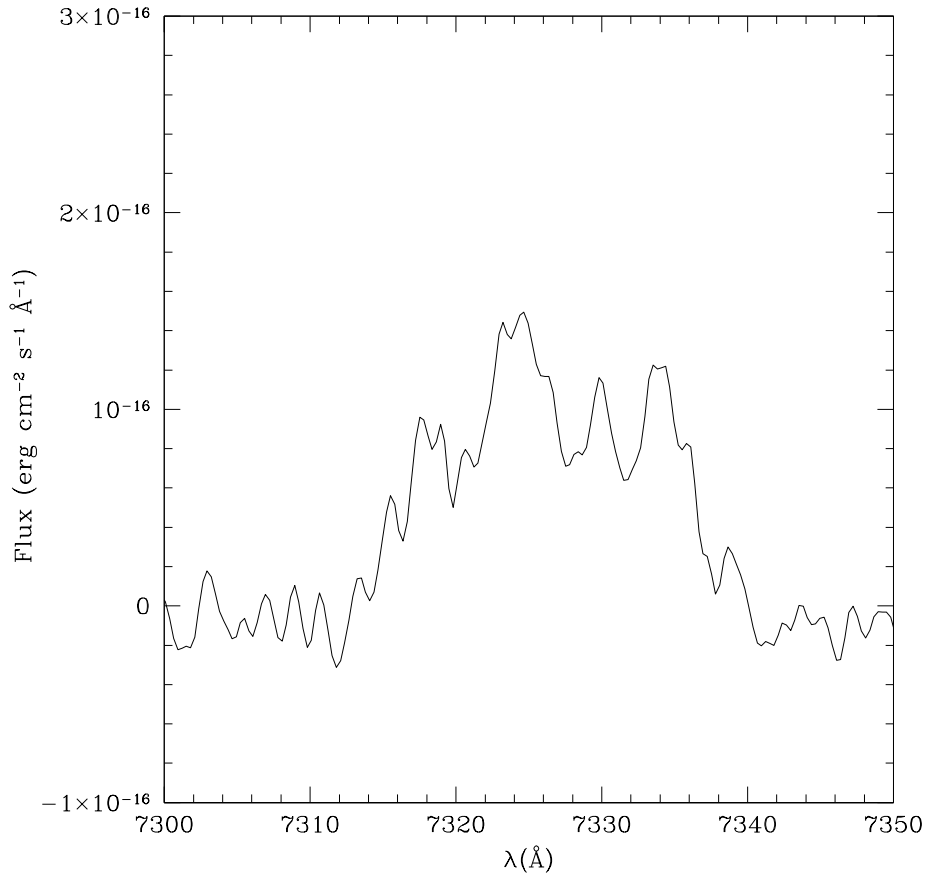

Figure 4.7: The [O II]$\lambda\lambda$7319, 7330 doublet in the N1 region of IC5063. It is possible to see the noisy profile and that the lines are completely blended.

Table 4.3: Ionization potential of the ions whose lines are used to measure temperture and density of the gas (Shaw and Dufour 1995).

Ion	O^+	S^+	O^{2+}	Ar^{3+}
Ionization potential (eV)	13.6	10.4	35.1	40.9

I did the calculation with the `temden` task. Even if the described line ratios are used to measure the temperature or the density, actually they depend on both quantities. For this reason, I started by calculating the density and assuming a temperature of 10^4 K, a typical value observed in photoionized nebulae, then I used the obtained value of density as input for the software to calculate the temperature and I iterated this process till values converged. In case of the low ionization gas, I could take advantage of the good S/N ratio of [S II] lines to calculate the electron density in all of the velocity bins of the regions. Fig. 4.4 (c) shows an example of N_e vs v plot. The analysis will be deepened in the following chapter.

4.6 Metallicity

The metallicity is one of the most important gas properties. As I said in Sec. 1.4, it can shade light on the origin of the ENLR gas. When ENLR has a metallicity compatible with that of the host galaxy, it could be composed of gas which has been part of the galaxy itself for a long time. On the other hand, different metallicity values could suggest that the gas has an external origin and it was brought inside the galaxy recently, by events like merging with other galaxies. In Sec 1.4, I also mentioned that the measurement of the metallicity value is difficult in this kind of gaseous nebulae, because we only have a superficial knowledge of the ionization mechanism. A good way to estimate the metallicity of these gaseous nebulae is to find some kind of line ratios which could be sensitive to this quantity and to compare data to simulations. Vaona (2010) found in his work that there are two lines ratios especially sensitive to metallicity: [N II]λ6584/[S II]$\lambda\lambda$6717, 6731 and [N II]λ6584/[O II]λ3727. They do not involve any hydrogen Balmer line, but only lines of heavy elements. The [N II]λ6584/[S II]$\lambda\lambda$6717, 6731 ratio does not depend on the extinction correction, while [N II]λ6584/[O II]λ3727 is very sensitive to this factor because the two lines are at the opposite extremes of the optical spectrum. The simulation, made with the photoionization code CLOUDY (last described by Ferland et al. (2013)), seem to indicate that there is a dependence of those ratios on the metallicity (Fig. 4.8). It is possible to see that low metallicity values have lower values of both ratios, and when they increase, the metallicity also increases. The arrow in Fig. 4.8 shows the dependence of the ratio on the absorption value. I tried to estimate the metallicity of the studied regions superimposing my data on the simulations.

4.7 Errors

Before starting with the discussions about the obtained results, it is important to open a short discussion about the expected and measured errors. I measured the errors

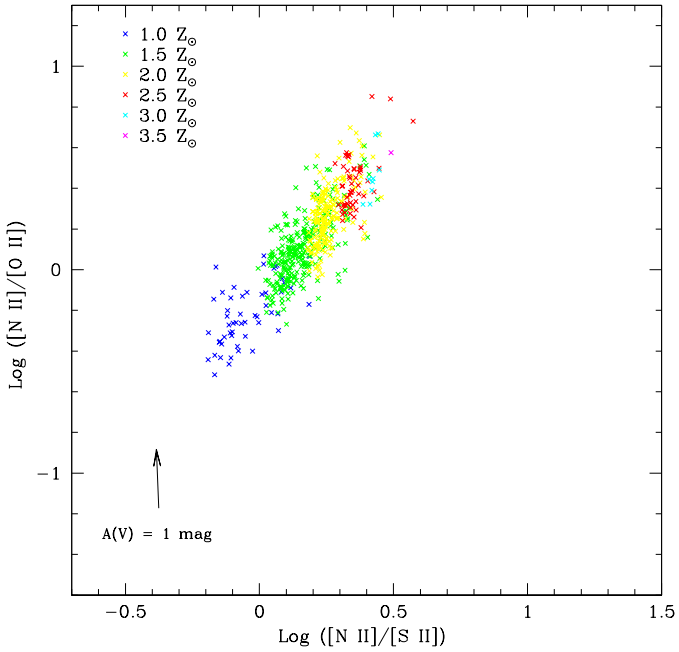

Figure 4.8: The [N II]λ6584/[S II]$\lambda\lambda$6717, 6731 vs [N II]λ6584/[O II]λ3727 with the points obtained by simulations of gas clouds photoionized by a power-law continuum, with metallicities from solar to 3.5 times the solar values.

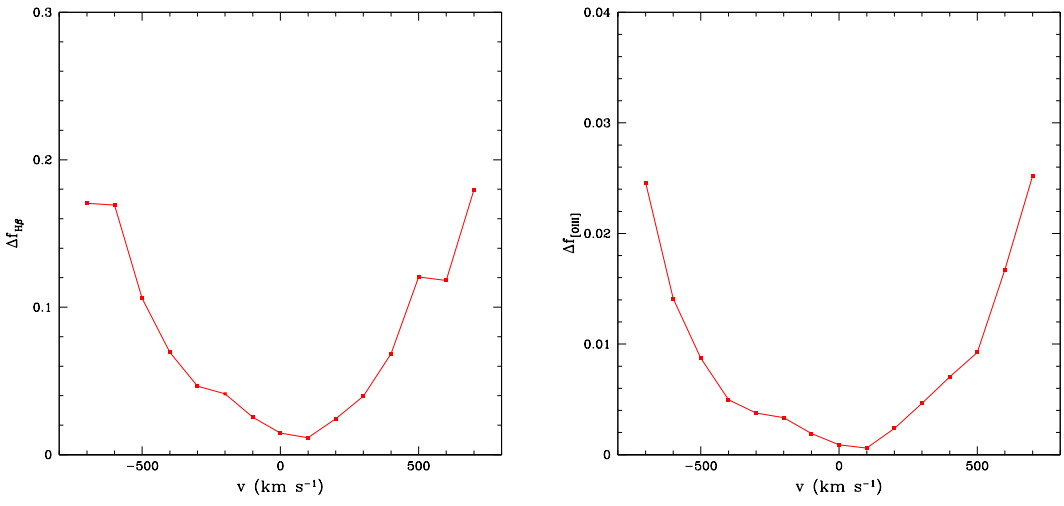

(a) **(b)**

Figure 4.9: The typical errors behaviour for (a) a weak line (Hβ) and (b) a strong line ([O III]λ5007) in the central regions of a galaxy. It has to be noticed the different scale on the y-axis.

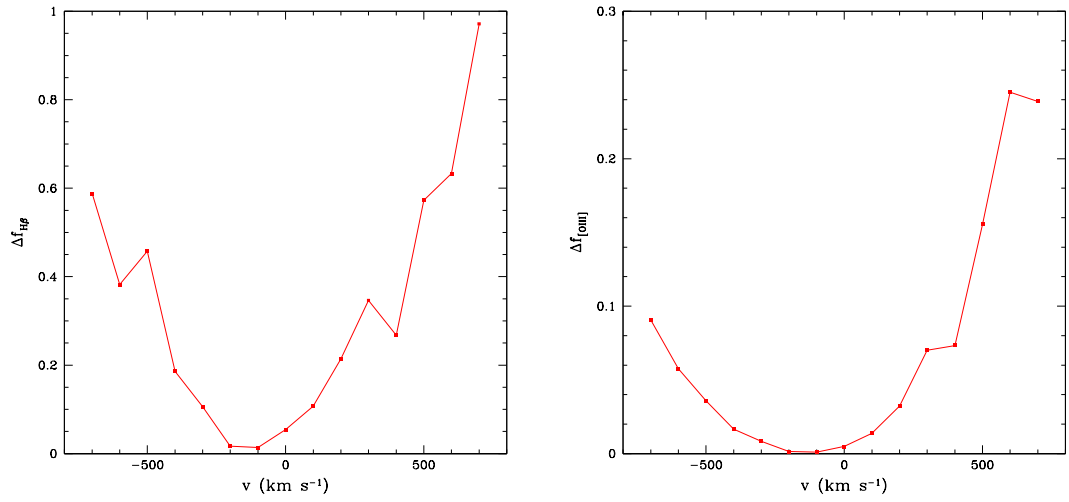

(a) **(b)**

Figure 4.10: The typical errors behaviour for (a) a weak line (Hβ) and (b) a strong line ([O III]λ5007) in an external region of a galaxy. It has to be noticed the different scale on the y-axis.

only for two important quantities: the ionization parameter and the [O III]λ5007/Hβ ratio. These are the only quantities, which depend on the measurements in a simple way. The error bars in the diagnostic diagrams are not useful in this context, while in other quantities such as temperature or density there is the serious problem of the propagation of error: sometimes it can lead to very high error values, therefore, other methods are needed in order to estimate the real uncertainties of the measured quantities.

But what are the main causes of the errors? I measured fluxes which, in a spectrum, are the area below the lines profile. When measuring an area it is possible to make errors in two parameters: the choice of the base and the height of the geometrical shape of the line. In this case, the base of the area is the width of the standard velocity bin, the height is obviously the average height of the line inside the small bin. The error of the bin width is negligible because I arbitrarily divided the lines in 100 kms^{-1} bins, so the possible errors are those due to the computer precision. The uncertainties on the height of the lines instead, could be very big, because they depend on where I decided to set the intensity of the continuum. If the continuum near the line is noisy this could be a difficut task and so this is the main source of error in the fluxes measurements.

For each line bin, the error could be calculated with the equation 4.14 where rms is the *root mean square* of the continuum, I_0 is the average height inside the bin, ΔI is the error on the measured flux and I is the total flux.

$$\frac{rms}{I_0} = \frac{\Delta I}{I} \tag{4.14}$$

It has to be noticed that I am interested in errors of the logarithmic ratio between two lines, so the final values could be obtained with the equation 4.15 where e is the Euler's number.

$$\Delta \log_{10}\left(\frac{I_1}{I_2}\right) = \left(\frac{\Delta I_1}{I_1} + \frac{\Delta I_2}{I_2}\right) \log_{10} e \tag{4.15}$$

To show the general behaviour of the errors as a function of velocity, I produced the plots in Fig. 4.9 which are relative to Hβ and [O III]λ5007 emission lines. In Fig. 4.9 (a) it is possible to see that in the low velocity bins the error for Hβ is almost negligible, while it becomes greater increasing $|v|$. in Fig. 4.9 (b) the behaviour is similar, but the y-axis scale is one tenth of the Hβ one, so the errors on [O III]λ5007, the brightest measured line in every spectra, could be really small. However these are two "good cases", with high S/N ratio. In very noisy spectra, as those in the external regions of the galaxies (Fig. 4.10), the errors could increase of more than one order of magnitude.

Chapter 5

Results

In this chapter I will show the results achieved for each galaxy. I will start discussing the shapes of the profiles of some important emission lines in various regions of each galaxy. This analysis allows to visually compare the emission of differently ionized gas. If two lines of ions with different ionization potential show the same profile, it could mean that the emitting gas is the same in both lines. On the other hand, if they have inconsistent profiles it is possible that they originate in different clouds. However, I have to remind that the spectra were not corrected for dust extinction, therefore I will consider that in the analysis. Then I will examine the behaviour of the absorption coefficient, looking for similarity with what I found in literature. After that I will try to understand which are the main ionization mechanism in the ENLR, thanks to the diagnostic diagrams. Finally I will comment the temperature and density measurement where I could measure it in the galaxies.

5.1 IC5063

First I studied the profile shape of the following emission lines: [O II]λ3727, [Ar IV]$\lambda\lambda$4711, 4740, Hβ, [O III]λ5007, [Fe VII]λ6087 and [O I]λ6300. To compare the shape of different lines, I superimposed their profile as a function of velocity, normalizing the fluxes with the value at the rest wavelength of each line. In Fig. 5.1 it is possible to see the comparison between the Hβ and [O III]λ5007 lines in three different regions of IC5063: S1, CN and N1. They are close to each other in wavelength, therefore there are not any problems related to the extinction. The two lines have quite the same shape everywhere. The only exception is visible in Fig. 5.1 (c), where the Hβ peak at v$>$ 0 is weaker than the [O III] ones. This might suggest that in that region the gas is highly ionized. It is also possible to notice that, even after the correction for the galaxy rotation velocity, the S1 emission lines are blueshifted. It seems that the whole lines are shifted towards negative velocities and this could be a sign of strong radial motions in this ENLR region.

In Fig. 5.2 I compared three lines of oxygen, in three different ionization states: O, O^+ and O^{++}. Because of the different ionization potential (Tab. 5.1) the three lines should be emitted by clouds characterized by different conditions. The [O III]λ5007 and [O I]λ6300 lines have similar profile shapes, in all of the considered regions but, in some cases, the [O I]λ6300 line is slightly weaker than the other line. On the other

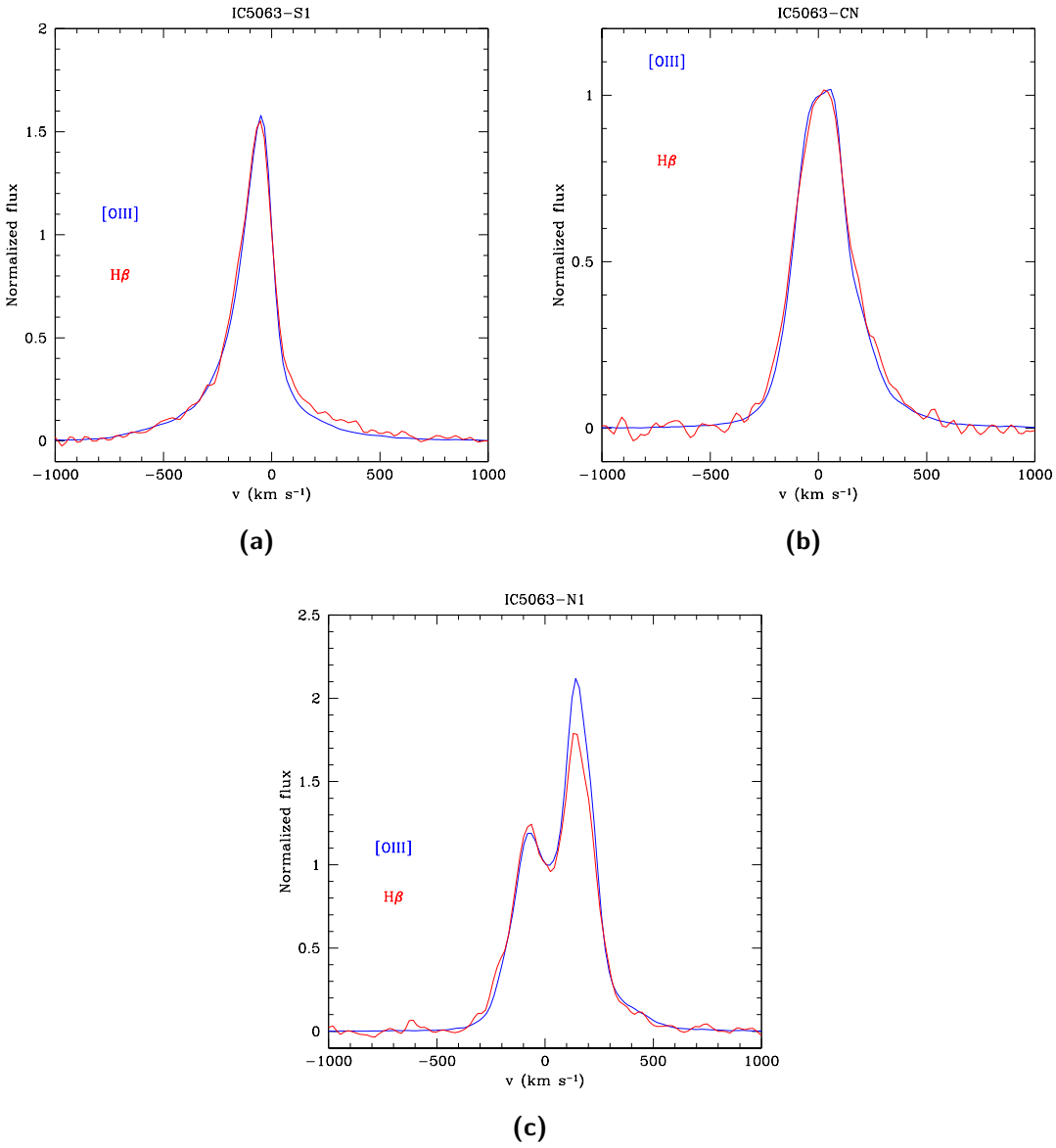

Figure 5.1: Comparison between Hβ (in red) and [O III]λ5007 (in blue) in the following IC5063 regions: S1, CN and N1. The lines fluxes are normalized to the flux value at the rest wavelength of each line.

Table 5.1: Energy needed to produce the various oxygen ions (Shaw and Dufour 1995), argon three times ionized (Shaw and Dufour 1995), and iron six times ionized (A. Kramida et al. 2014).

Ion	H	O	O^{+}	O^{2+}	Ar^{3+}	Fe^{6+}
Ionization potential (eV)	-	-	13.6	35.1	40.9	99.0

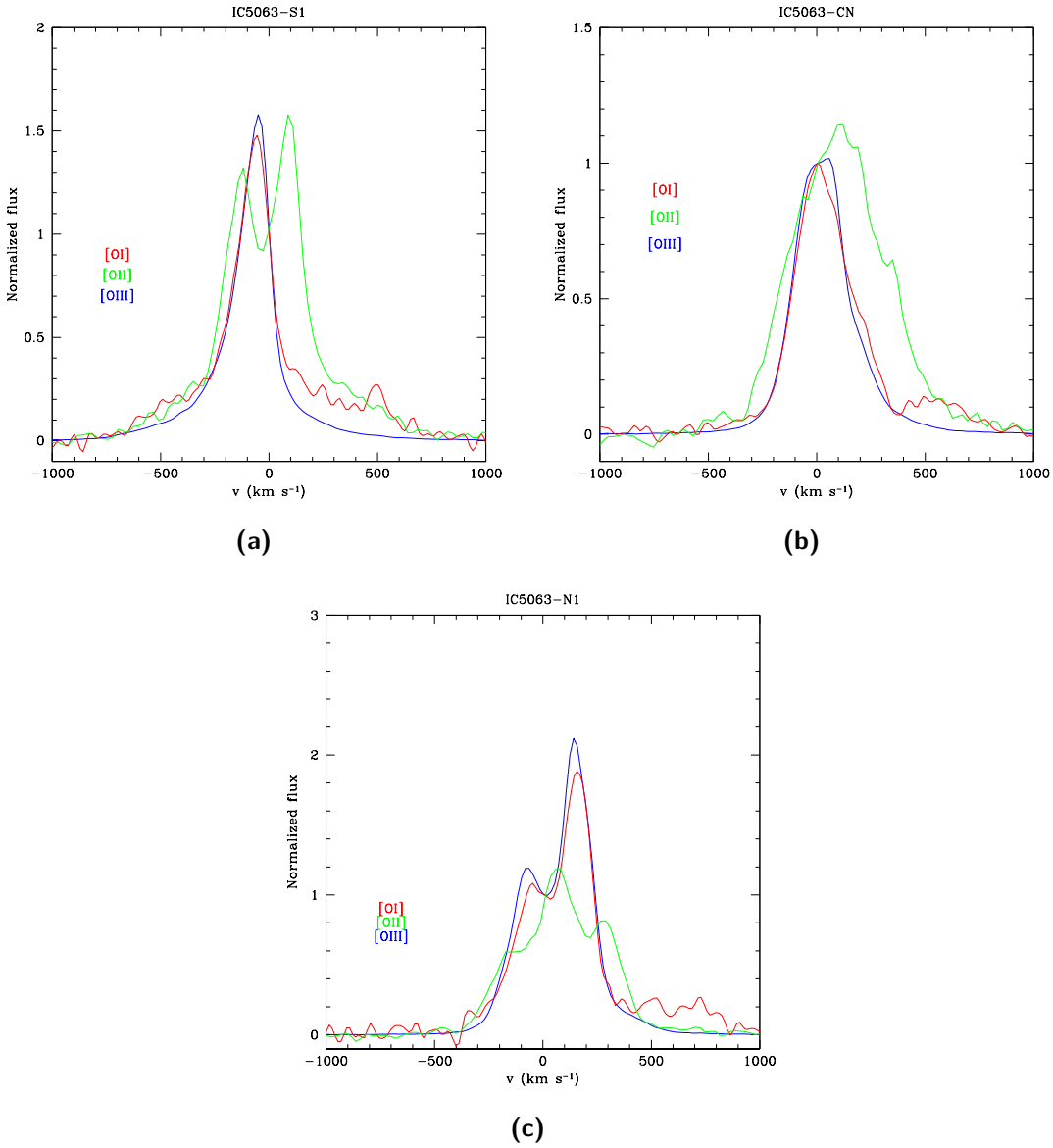

Figure 5.2: Comparison between [O I]λ6300 (red) , [O II]λ3727 (green) and [O III]λ5007 (blue) in the same regions as before. The lines fluxes are normalized to the flux value at the rest wavelength of each line.

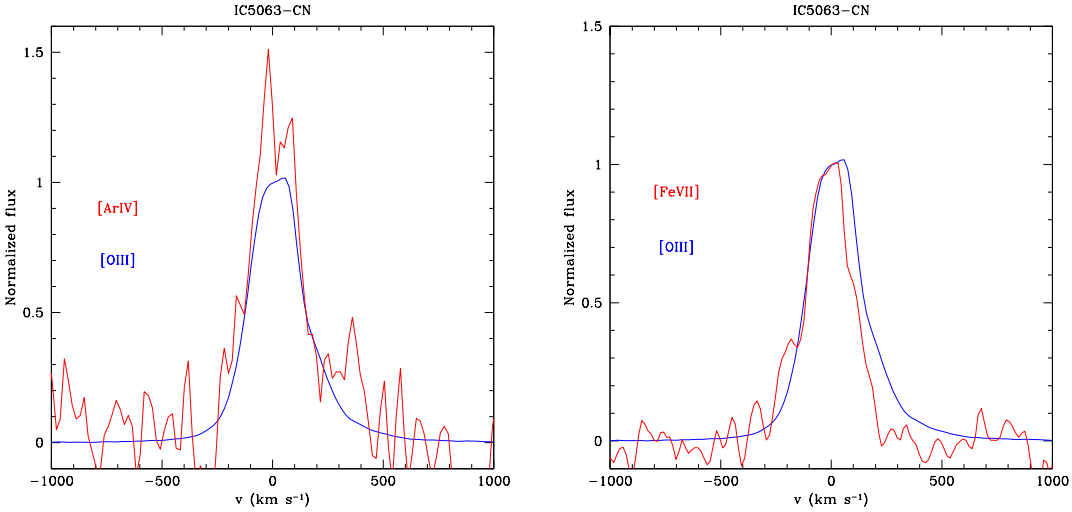

Figure 5.3: (a) Comparison between [Ar IV]λ4740 (red) and [O III]λ5007 (blue) in the CN region. (b)Comparison between [Fe VII]λ6087 (red) and [O III]λ5007 (blue) in the CN region. The lines fluxes are normalized to the flux value at the rest wavelength of each line.

hand, the [O II]λ3727 line has a completely different shape, as it is broader and noisier than the other lines. The reasons could be that the [O II]λ3727 is located in a region of the spectrum characterized by high extinction and low S/N and that it is actually a doublet composed by very close lines: [O II]λ3726 and [O II]λ3729. In Fig. 5.2 (a) the two components are clearly visible.

I compared the [O III]λ5007 emission line profile to that of [Ar IV]λ4740 (Fig. 5.3 (a)) and [Fe VII]λ6087 (Fig. 5.3 (b)). I could compare them only for the central region of IC5063 (CN), because they both are weak lines and the central spectra have the highest S/N ratio. The [Ar IV]λ4740 is a weak emission line which is useful to measure the electron density of the highly ionized gas, and it arises in the same region of the [O III]λ5007 line because the two elements need almost the same energy to be produced. Therefore, they are expected to have the same profile. In Fig. 5.3 (a) it is easy to see that the argon line is quite noisy but it has the same width of the oxygen line. It also shows two peaks which are not present in the oxygen line, but maybe it is only an effect of the low S/N of this line. The [Fe VII]λ6087 is another weak emission line which is interesting because it needs at least an energy of about 100 eV to be produced (Tab. 5.1). Therefore, it comes from clouds with a very high ionization degree. It is easy to see in Fig. 5.3 (b) that the two profiles are similar, but the iron line shows a small peak at $v < 0\,\mathrm{kms}^{-1}$ and a bump at $v > 0\,\mathrm{kms}^{-1}$, which are not present in the [O III]λ5007, and it also is a little narrower than the oxygen line.

In Tab. 5.2 it is possible to see that $A(V)$ is quite high in the whole galaxy. It is larger than 1.0 mag in all regions and less than 1.5 mag only in two regions. These high extinction values are expected because one of the main features of this galaxy is the presence of a complex system of dust lanes whose axis is aligned with that of the ionization cones (see Sec. 2.1.1). Furthermore, the highest $A(V)$ values are those

Table 5.2: Average $A(V)$ values obtained for IC5063.

Region	$A(V)$ (mag)
S2	1.84
S1	1.90
S0	2.16
CS	2.89
CN	2.21
N0	1.58
N1	1.47
N2	1.33

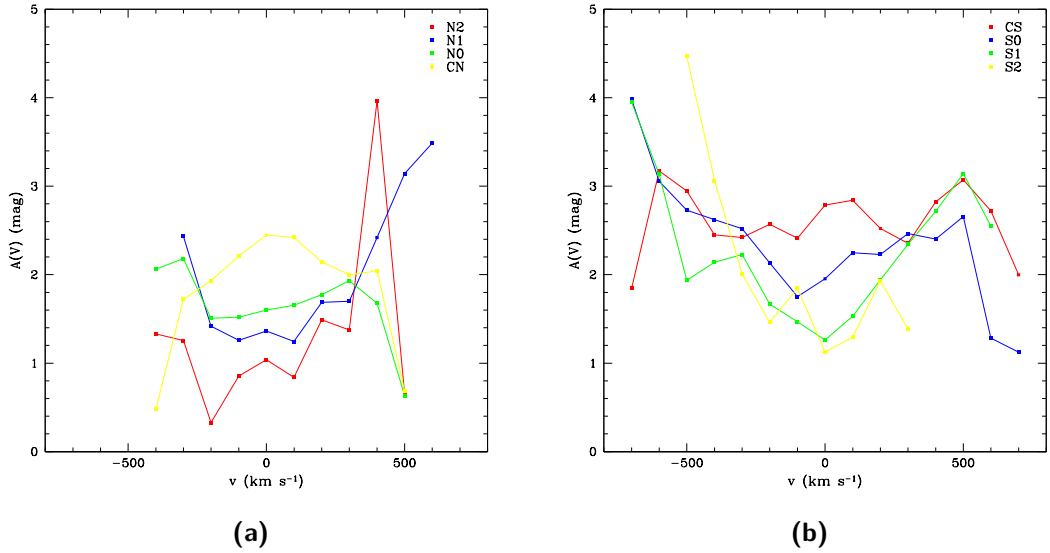

(a) **(b)**

Figure 5.4: $A(V)$ vs v diagrams for IC5063 northern regions (a) and southern regions (b).

in the nuclear regions of the galaxy and the extinction decreases as the distance from the nucleus increases. Looking at the behavior of $A(V)$ in the velocity bins (Fig. 5.4) it is possible to see that the different regions show different trends. The CN region has the highest value at $v = 0\,\mathrm{km s^{-1}}$ then it drops to lower values. Furthermore, the N0 region shows the highest $A(V)$ values at $v = -300\,\mathrm{km s^{-1}}$ then it suddenly drop and it start to increase slowly till $v = 300\,\mathrm{km s^{-1}}$, where it drops again. In the other regions, the general behaviour of the absorption value is to increase when $|v|$ increases, but, for $v > 0\,\mathrm{km s^{-1}}$, in the bins with the higher velocities it suddenly drops. An exception is the CS region, which shows a high data dispersion but a quite constant value. Another issue to notice is that at high velocities also the data dispersion increases, and this may be due to the low S/N ratio of the lines wings, in particular on Hβ. There are velocity bins which apparently lack of extinction. There, the measured Hα/Hβ is smaller than the theoretical value and I decided to set $A(V)$ to 0 in order not to lose all of the high velocity components.

In order to understand the gas ionization mechanism for every region of the galaxy, I plotted the diagnostic diagrams described in Sec. 4.3, (see Fig. 5.5 and those that

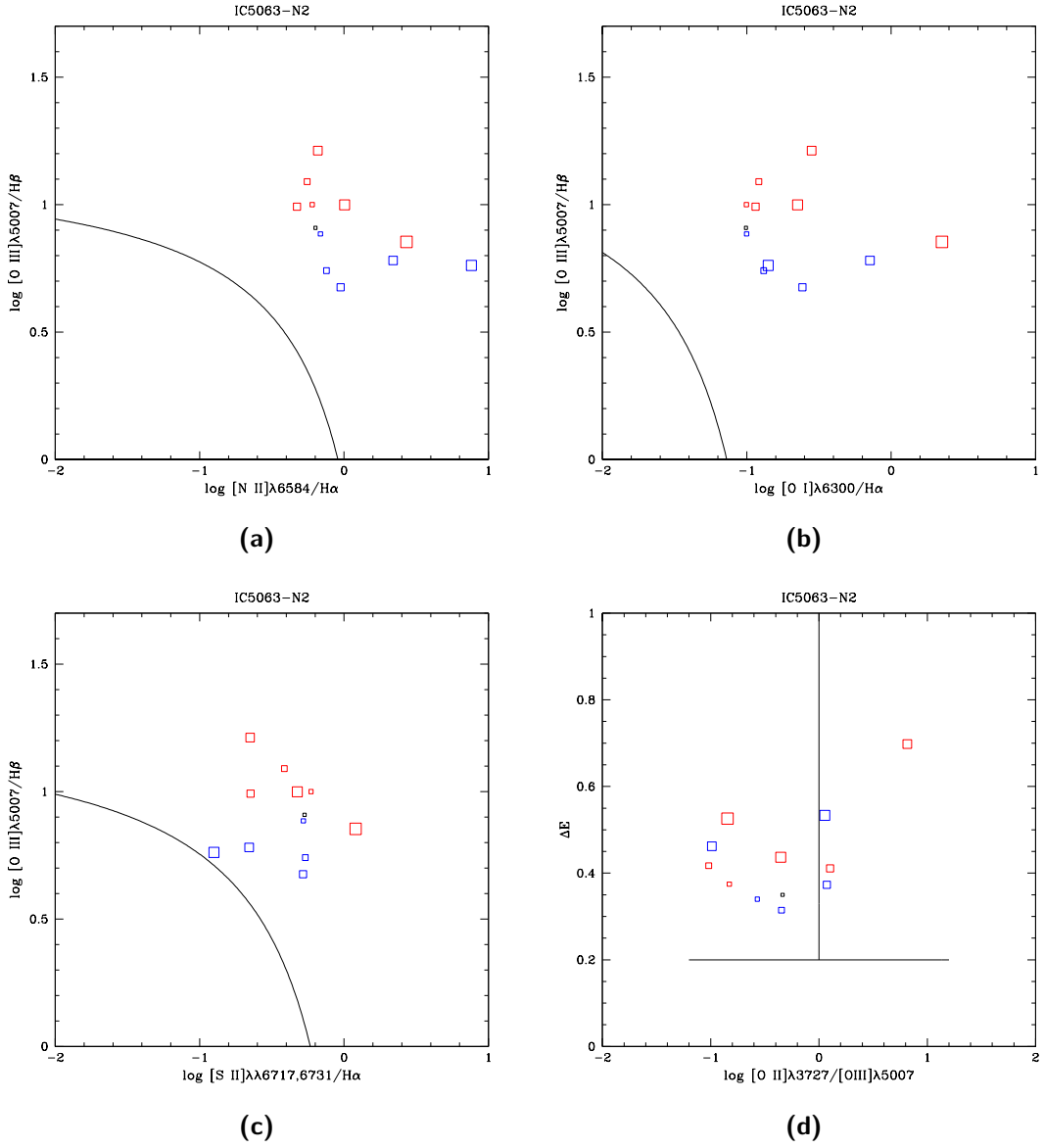

Figure 5.5: (a)[N II]λ6584/Hα vs [O III]λ5007/Hβ (b) [O I]λ6300/Hα vs [O III]λ5007/Hβ (c) [S II]$\lambda\lambda$6717, 6731/Hα vs [O III]λ5007/Hβ diagnostic diagrams for the N2 region of IC5063. The black lines are the empirical separation between H II regions and other regions from Kewley et al. (2001). (d) ΔE vs [O II]λ3727/[O III]λ5007 diagnostic diagram for the same region. The vertical line divides the power-law ionized regions (on the left) and the shock ionized ones (on the right). The horizontal line divides the H II regions from the others. In all diagrams, red squares represent bins with $v > 0$, blue squares data with $v < 0$ and the black ones are for $v = 0$. Bigger squares correspond to higher velocities.

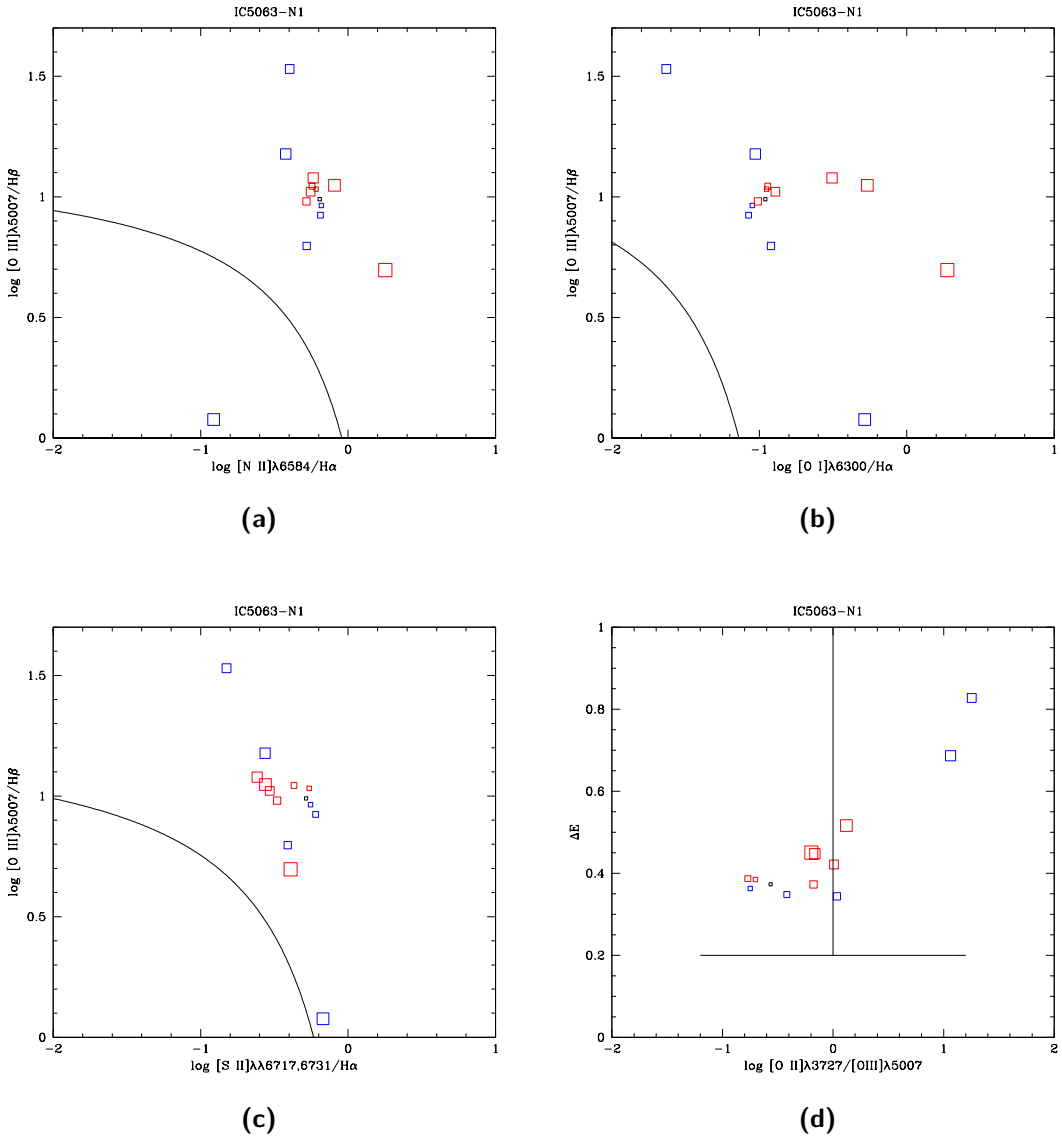

Figure 5.6: (a)[N II]λ6584/Hα vs [O III]λ5007/Hβ (b) [O I]λ6300/Hα vs [O III]λ5007/Hβ (c) [S II]$\lambda\lambda$6717, 6731/Hα vs [O III]λ5007/Hβ diagnostic diagrams for the N1 region of IC5063. The black lines are the empirical separation between H II regions and other regions from Kewley et al. (2001). (d) ΔE vs [O II]λ3727/[O III]λ5007 diagnostic diagram for the same region. The vertical line divides the power-law ionized regions (on the left) and the shock ionized ones (on the right). The horizontal line divides the H II regions from the others. In all diagrams, red squares represent bins with $v > 0$, blue squares data with $v < 0$ and the black ones are for $v = 0$. Bigger squares correspond to higher velocities.

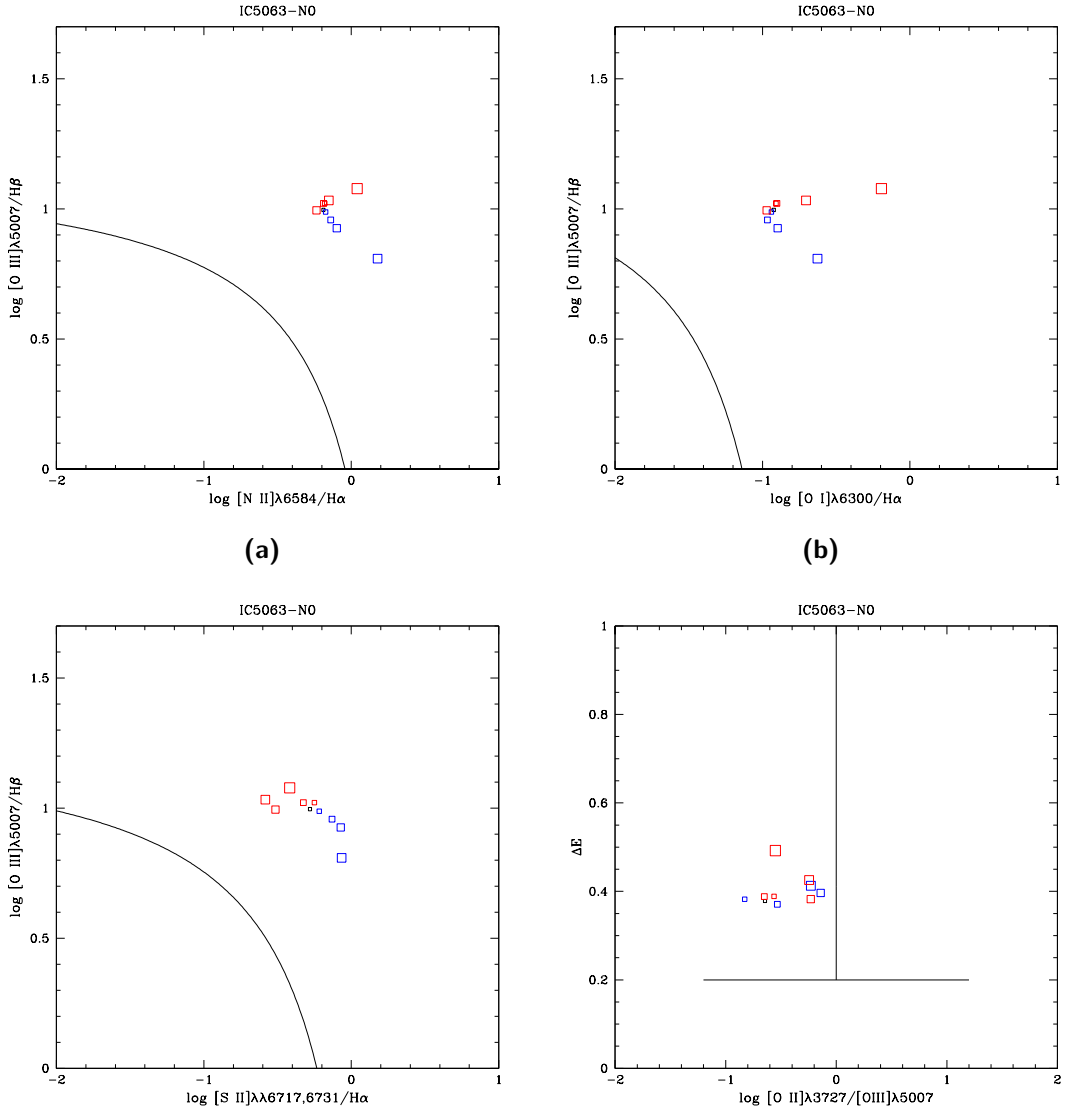

Figure 5.7: (a)[N II]λ6584/Hα vs [O III]λ5007/Hβ (b) [O I]λ6300/Hα vs [O III]λ5007/Hβ (c) [S II]$\lambda\lambda$6717, 6731/Hα vs [O III]λ5007/Hβ diagnostic diagrams for the N0 region of IC5063. The black lines are the empirical separation between H II regions and other regions from Kewley et al. (2001). (d) ΔE vs [O II]λ3727/[O III]λ5007 diagnostic diagram for the same region. The vertical line divides the power-law ionized regions (on the left) and the shock ionized ones (on the right). The horizontal line divides the H II regions from the others. In all diagrams, red squares represent bins with $v > 0$, blue squares data with $v < 0$ and the black ones are for $v = 0$. Bigger squares correspond to higher velocities.

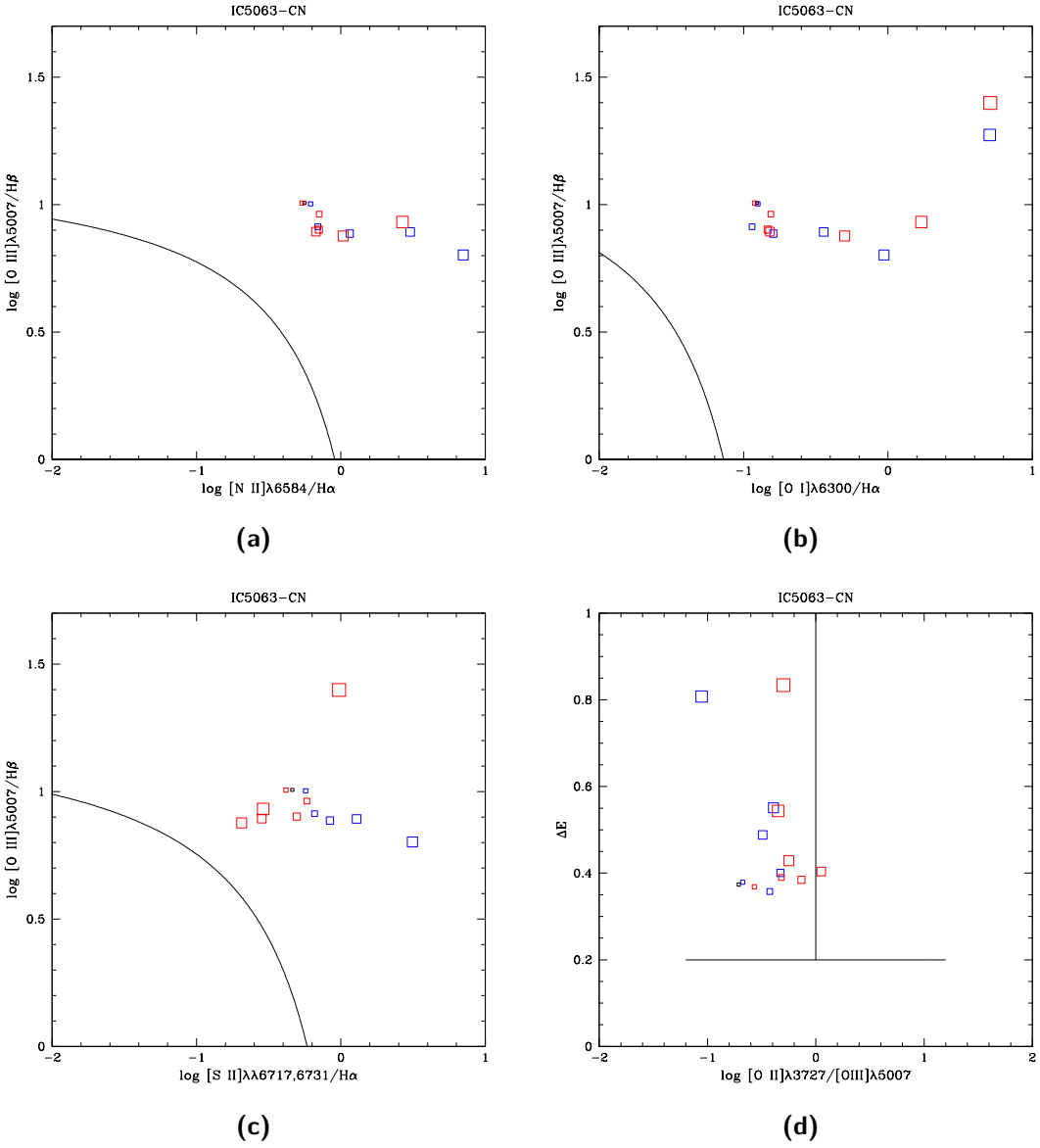

Figure 5.8: (a)[N II]λ6584/Hα vs [O III]λ5007/Hβ (b) [O I]λ6300/Hα vs [O III]λ5007/Hβ (c) [S II]$\lambda\lambda$6717, 6731/Hα vs [O III]λ5007/Hβ diagnostic diagrams for the CN region of IC5063. The black lines are the empirical separation between H II regions and other regions from Kewley et al. (2001). (d) ΔE vs [O II]λ3727/[O III]λ5007 diagnostic diagram for the same region. The vertical line divides the power-law ionized regions (on the left) and the shock ionized ones (on the right). The horizontal line divides the H II regions from the others. In all diagrams, red squares represent bins with $v > 0$, blue squares data with $v < 0$ and the black ones are for $v = 0$. Bigger squares correspond to higher velocities.

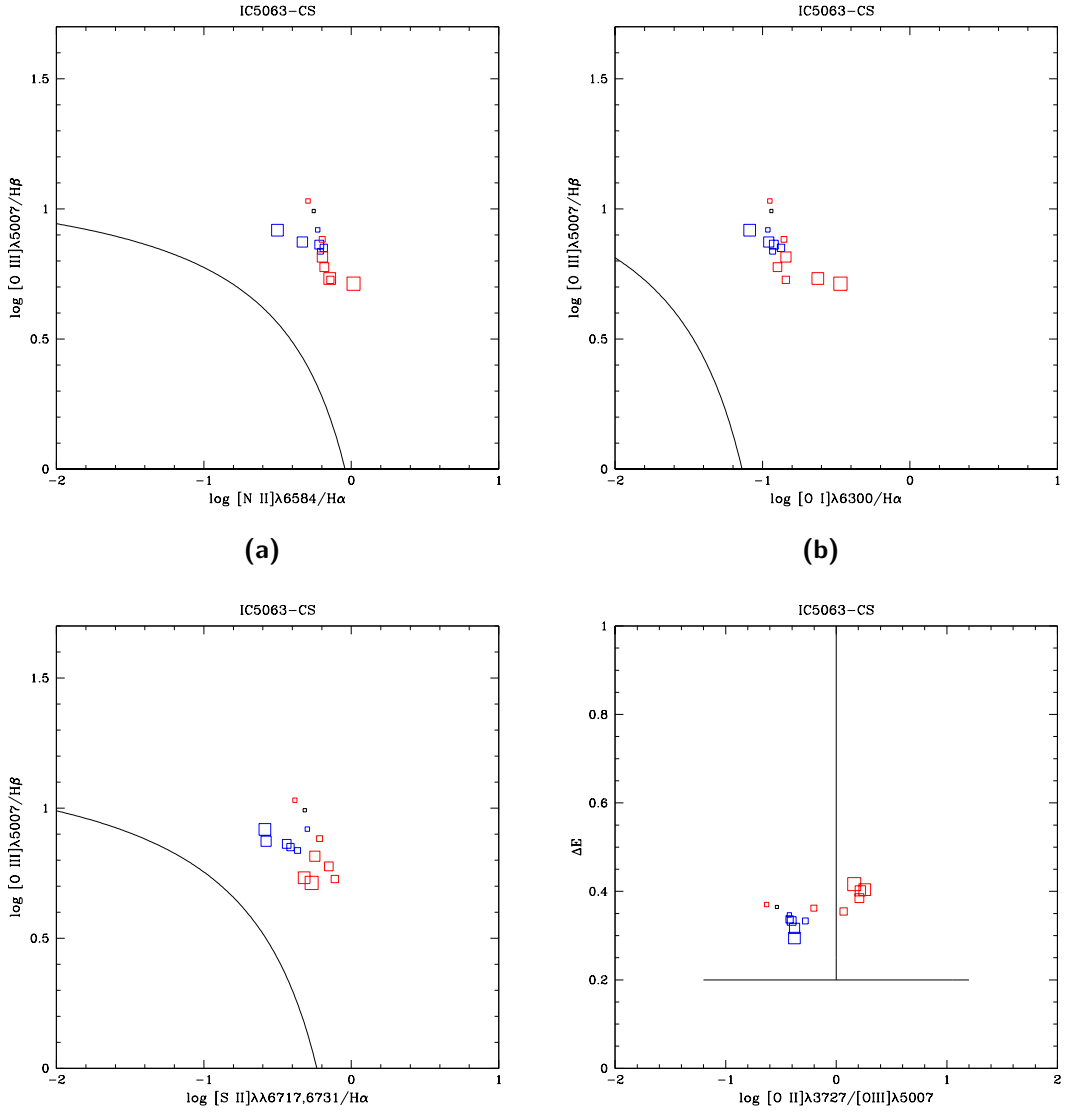

Figure 5.9: (a)[N II]λ6584/Hα vs [O III]λ5007/Hβ (b) [O I]λ6300/Hα vs [O III]λ5007/Hβ (c) [S II]$\lambda\lambda$6717, 6731/Hα vs [O III]λ5007/Hβ diagnostic diagrams for the CS region of IC5063. The black lines are the empirical separation between H II regions and other regions from Kewley et al. (2001). (d) ΔE vs [O II]λ3727/[O III]λ5007 diagnostic diagram for the same region. The vertical line divides the power-law ionized regions (on the left) and the shock ionized ones (on the right). The horizontal line divides the H II regions from the others. In all diagrams, red squares represent bins with $v > 0$, blue squares data with $v < 0$ and the black ones are for $v = 0$. Bigger squares correspond to higher velocities.

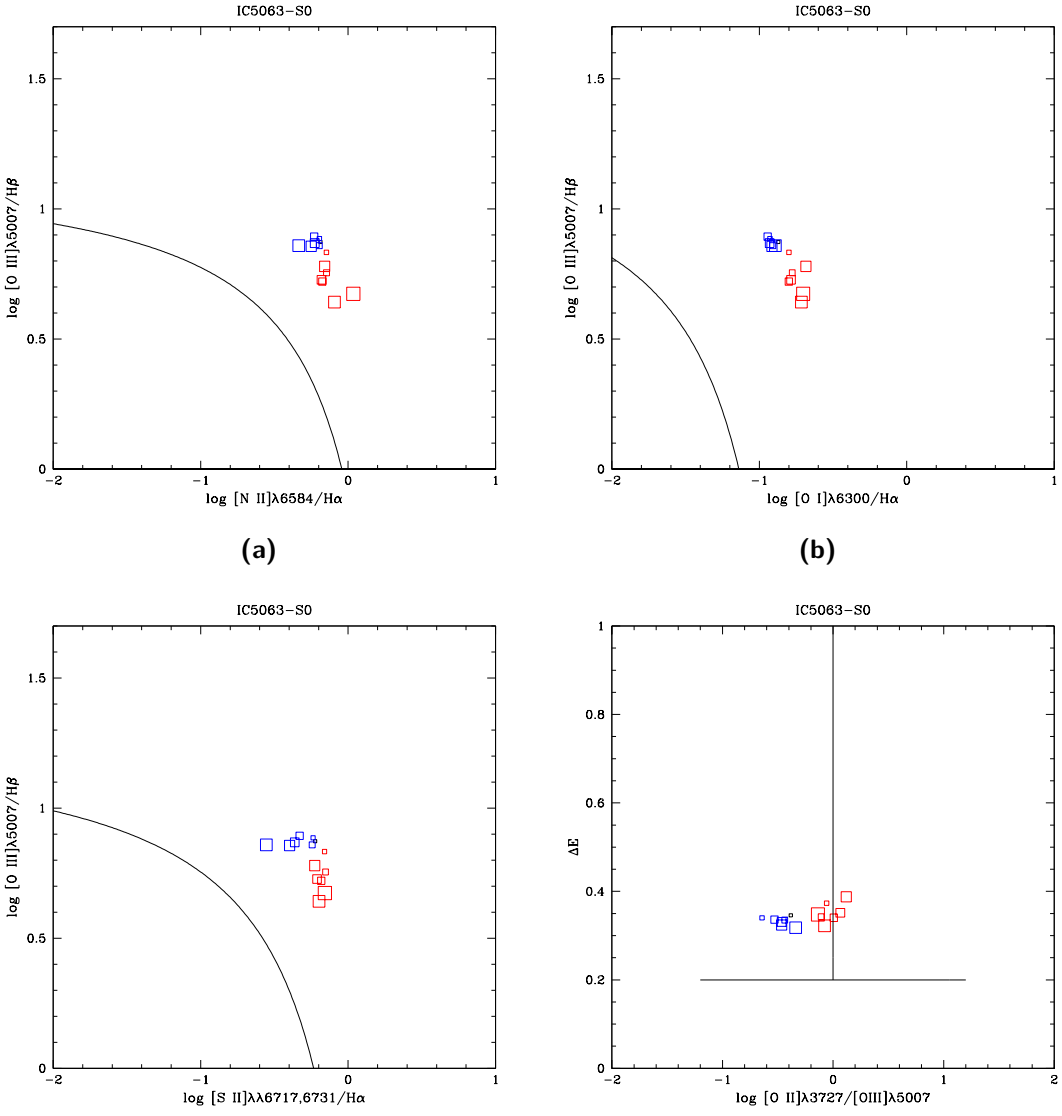

Figure 5.10: (a)[N II]λ6584/Hα vs [O III]λ5007/Hβ (b) [O I]λ6300/Hα vs [O III]λ5007/Hβ (c) [S II]$\lambda\lambda$6717, 6731/Hα vs [O III]λ5007/Hβ diagnostic diagrams for the S0 region of IC5063. The black lines are the empirical separation between H II regions and other regions from Kewley et al. (2001). (d) ΔE vs [O II]λ3727/[O III]λ5007 diagnostic diagram for the same region. The vertical line divides the power-law ionized regions (on the left) and the shock ionized ones (on the right). The horizontal line divides the H II regions from the others. In all diagrams, red squares represent bins with $v > 0$, blue squares data with $v < 0$ and the black ones are for $v = 0$. Bigger squares correspond to higher velocities.

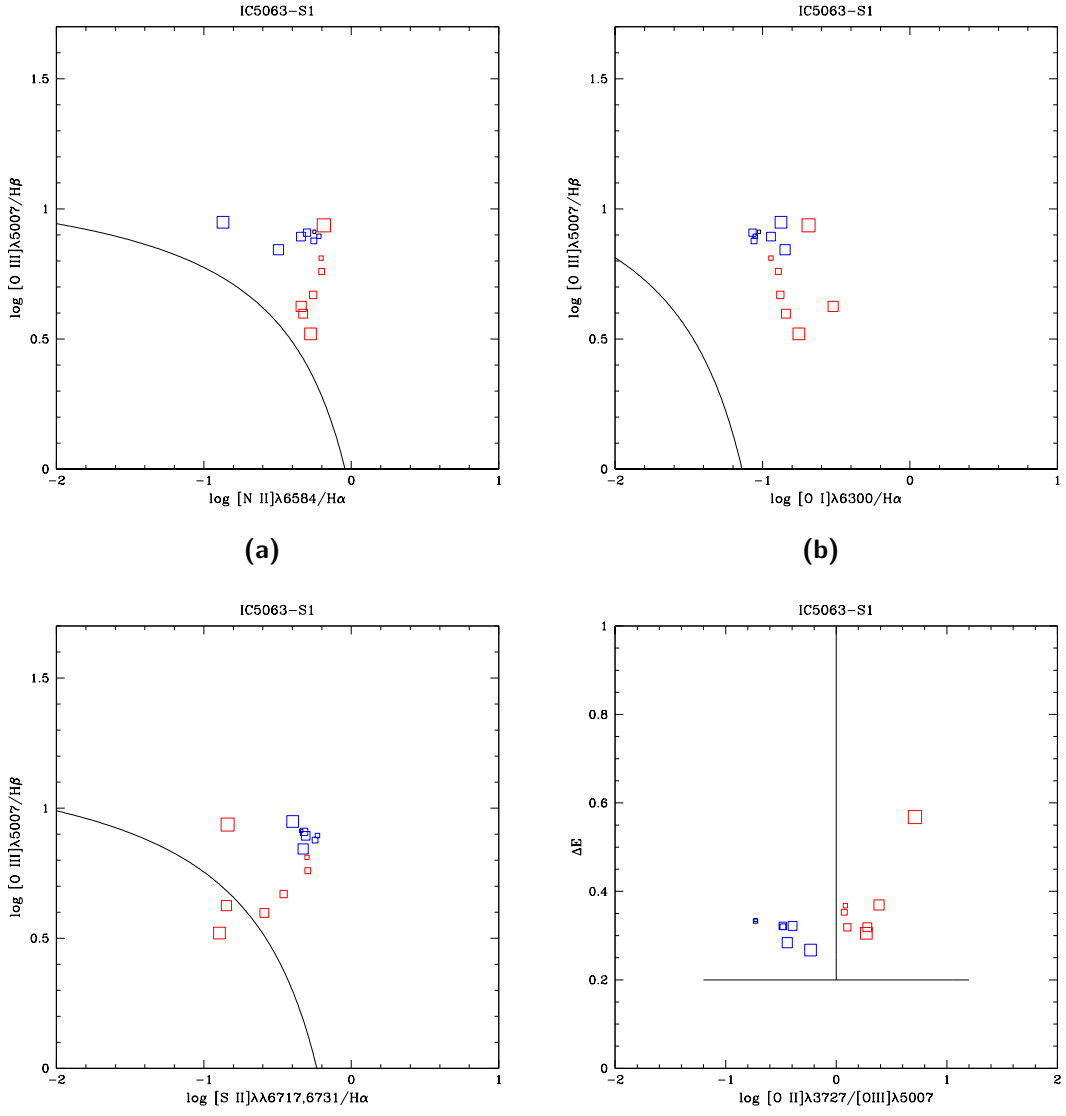

Figure 5.11: (a)[N II]λ6584/Hα vs [O III]λ5007/Hβ (b) [O I]λ6300/Hα vs [O III]λ5007/Hβ (c) [S II]$\lambda\lambda$6717, 6731/Hα vs [O III]λ5007/Hβ diagnostic diagrams for the S1 region of IC5063. The black lines are the empirical separation between H II regions and other regions from Kewley et al. (2001). (d) ΔE vs [O II]λ3727/[O III]λ5007 diagnostic diagram for the same region. The vertical line divides the power-law ionized regions (on the left) and the shock ionized ones (on the right). The horizontal line divides the H II regions from the others. In all diagrams, red squares represent bins with $v > 0$, blue squares data with $v < 0$ and the black ones are for $v = 0$. Bigger squares correspond to higher velocities.

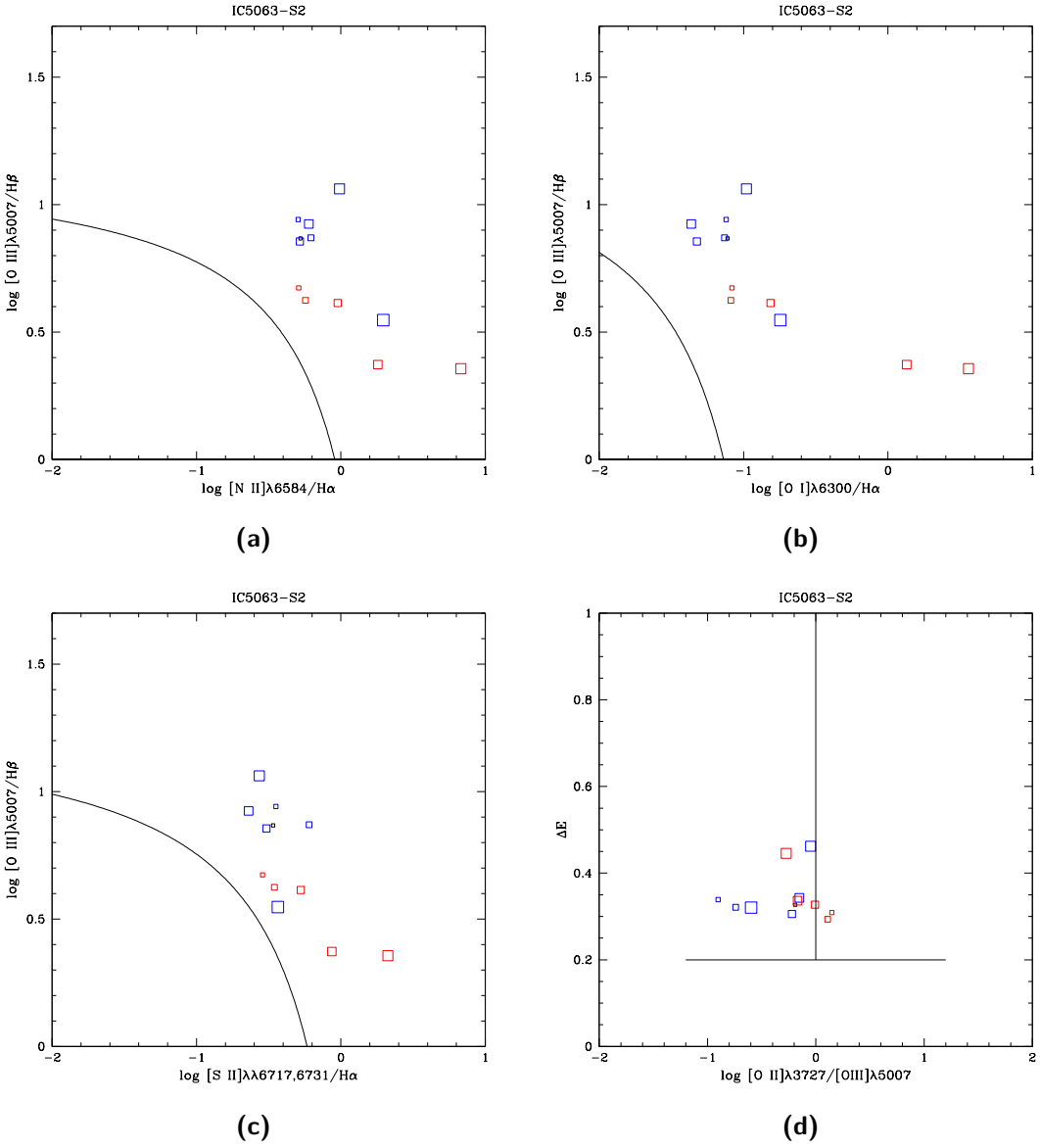

Figure 5.12: (a)[N II]λ6584/Hα vs [O III]λ5007/Hβ (b) [O I]λ6300/Hα vs [O III]λ5007/Hβ (c) [S II]$\lambda\lambda$6717, 6731/Hα vs [O III]λ5007/Hβ diagnostic diagrams for the S2 region of IC5063. The black lines are the empirical separation between H II regions and other regions from Kewley et al. (2001). (d) ΔE vs [O II]λ3727/[O III]λ5007 diagnostic diagram for the same region. The vertical line divides the power-law ionized regions (on the left) and the shock ionized ones (on the right). The horizontal line divides the H II regions from the others. In all diagrams, red squares represent bins with $v > 0$, blue squares data with $v < 0$ and the black ones are for $v = 0$. Bigger squares correspond to higher velocities.

follow). All of them exclude the ionization from hot main sequence stars as the main ionization mechanism at work in this galaxy. Only a small number of regions have velocity components located in the section of the diagram which indicates ionization by the H II regions. Moreover, these points are classified in this way only in one diagnostic diagram and they are not confirmed by other measurements. It has to be noticed that, in most of these diagrams, it does not seem to be any dependence on velocity of the ionization mechanism. It is very interesting that the ΔE vs [O II]λ3727/[O III]λ5007 diagram identifies a relevant number of the misured regions as ionized by shock-waves. In the S1 region (5.11 (d)) it seems that all of the gas which moves with $v > 0\,\mathrm{kms}^{-1}$ is ionized by this mechanism. It is possible to notice this trend also in the nearby S0 and CS regions. In the other plots there is not a particular trend in the shock ionized regions. I have to remind that [O II]λ3727/[O III]λ5007 is strongly affected by the extinction so this effect could be a consequence of the correction. In order to check the accuracy of the correction it can be useful to compare the behaviour of the ionization parameter, as a function of the velocity, to that of the [O III]λ5007/Hβ ratio. The [O III]λ5007/Hβ ratio is not a real ionization parameter, but it is quite sensitive to the gas ionization degree and it does not depend on the extinction because the involved lines are close. If the behaviours of these two quantities are similar, it means that the extinction correction is good. Comparing the diagrams 5.13 (d) and (e) it is possible to see that for the S1, S0 and CS regions the U vs v and [O III]λ5007/Hβ vs v diagrams are in good agreement, so it is possible that shocks are important in ionizing some of the ENLR gas clouds.

Analysing more accurately the ionization parameters it is possible to see that in the northern regions there is a high data dispersion, in particular for $v < 0\,\mathrm{kms}^{-1}$. Also the [O III]λ5007/Hβ vs v plot shows high dispersion in those velocity bins, so it is not possible to compare the behaviours of these quantities. For $v > 0\,\mathrm{kms}^{-1}$ the data are slightly more understandable, and it is possible to see a difference in the values of ionization parameter at $v < 0$, where $\log U \sim -2.5$, and $v > 0\,\mathrm{kms}^{-1}$, where $\log U \sim -2.0$. This small difference could be caused by the increase of the electron density at high v, which is shown in Fig. 5.13 (c). In fact, recalling the equation 4.11, $U \propto n_e^{-1}$, so if n_e increases, U is expected to decrease. This behaviour can be seen in all of the northern regions.

In the southern regions there is a smaller dispersion, so it is possible to better discuss the data. The first thing to notice is that for $v < 0\,\mathrm{kms}^{-1}$ the ionization parameter is costant in every region, with values between -2.3 and -2.6, with the only exception of the region S2 which shows an initial drop of the ionization parameter followed by a small increase. Except for this last region, [O III]λ5007/Hβ behaves as U. For positive values of velocity, U decreases when v increases, and there is the same trend also in [O III]λ5007/Hβ. This behaviour agrees with the increase of electron density with the velocity in all regions. Therefore, we can exclude extinction effects. The ionization parameter in the S2 region, for $v > 0\,\mathrm{kms}^{-1}$ increases as the velocity increases. Ozaki (2009) supposed that this kind of behaviour in an ENLR is related to the presence of shock-waves. However, this behaviour is not confirmed by [O III]λ5007/Hβ. The ΔE vs [O II]λ3727/[O III]λ5007 diagram shows that some of S2 velocity bins are ionized by shock-waves, but there is not a full correspondance between the two plots. The reason of this behaviour could be the extinction correction. In those velocity bins I could not measure A(V), so I used the measured values without any correction. In these

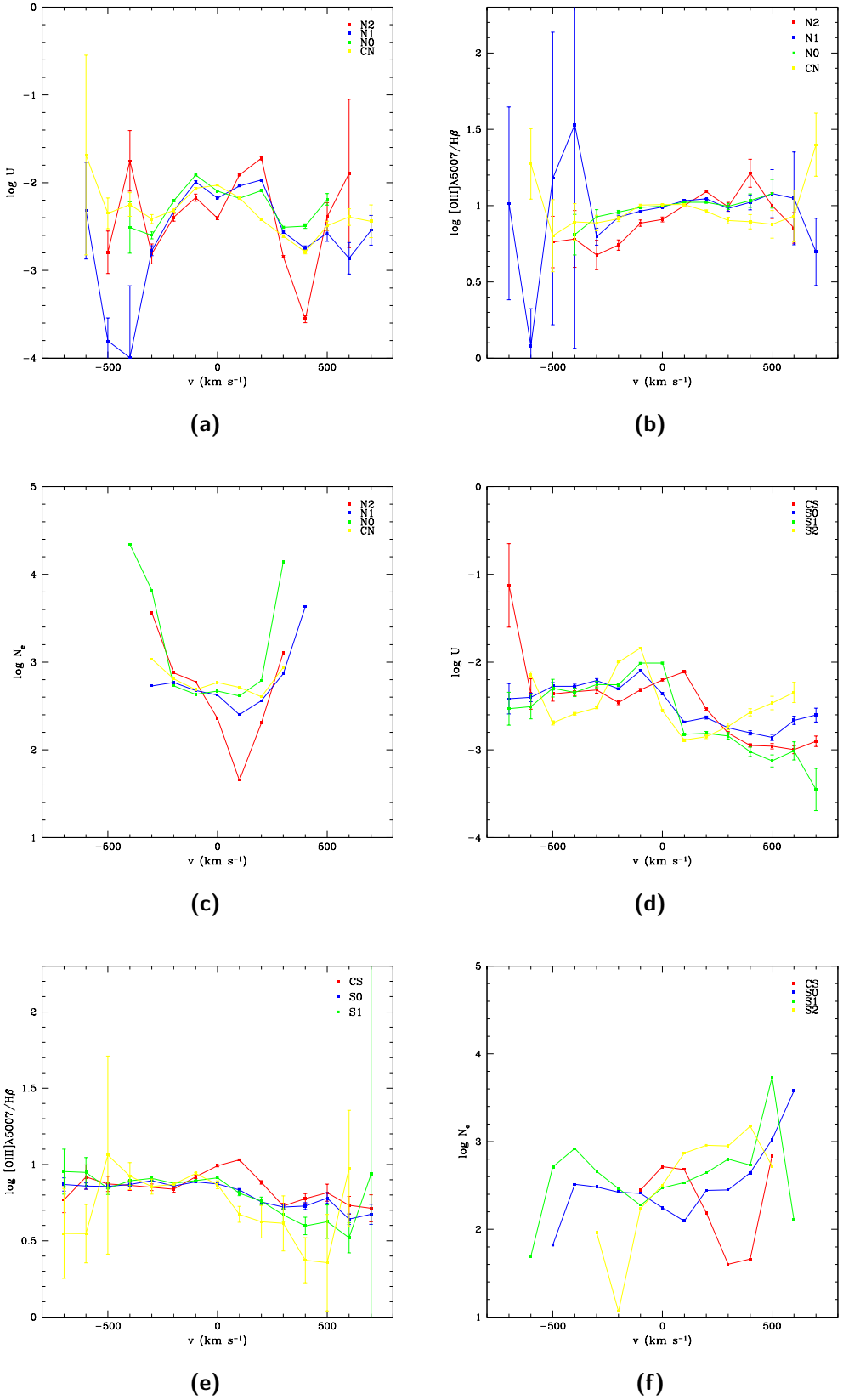

Figure 5.13: U vs v,[O III]λ5007/Hβ vs v and N_e vs v diagrams for the northern regions (in the first three graphics) and southern regions (in the last three).

Table 5.3: Temperature and density in IC5063.

	Low Ionization		High Ionization	
Region	T (K)	n_e (cm^{-3})	T (K)	n_e (cm^{-3})
S2	9696.2	328.8	-	-
S1	7632.8	449.8	-	-
S0	14286.9	210.3	-	-
CS	10478.9	76.4	13306.0	7548.5
CN	10900.8	625.6	13624.3	16815.7
N0	10756.3	688.5	13915.6	4005.5
N1	11349.0	505.8	13260.2	1987.1
N2	11552.3	224.5	14339.4	1038.6

cases, due to the $A(V)$ dependence on the wavelength, there is an underestimation of the [O II]λ3727/[O III]λ5007 ratio, which means an overestimation of the ionization parameter (see eq. 4.12). It is also possible to see that there is not any dependance of the U trends on the distance from the ionizing source.

Other physical parameters that I analysed are gas temperature and density. As previously mentioned (Sec. 4.5), I could not measure those quantities in all of the velocity bins, but I obtained only average values for each region. I could also measure temperature and electron density of gas in two different ionization degrees. In Tab. 5.3 all of the measured value for IC5063 are listed. It is possible to notice that the highly ionized gas is characterized by higher values of both quantities, especially density. Moreover, the temperature values are compatible with photoionized gas where the main cooling process is the emission of metals forbidden lines. In this case, the expected temperature is between 10000 and 20000 K, depending on the efficiency of the heating and cooling processes (Osterbrock and Ferland 2006). Only the S2 and S1 regions show a lower temperature, maybe due to the small S/N in the [O II] lines.

Once obtained the average temperature of the low-ionized gas, I tried to measure the electron density in the velocity bins, by means of the [S II] lines. The results are shown in Fig. 5.13 (c) and (f). In some cases it was not possible to measure this quantity. The main reason for this difficulty in measuring the density could be the lines deblending process: when imprecise, it could have as a consequence that the measured ratios are outside the sensitivity range of the formula used to estimate density from the [S II] lines ratio. This could also influence the measured values of the density, together with the fact that the real temperature could be different from the average temperature, which I used to calculate the density, in some of the velocity bins.

Finally, I considered the gas metallicity. Fig. 5.14 and 5.15 show the graphics with the metallicity models and measurements for every velocity bin in each region. It is possible to easily notice that not all of the measured points are in good agreement with the simulations. In general, data corresponding to lower velocities seem to be in good agreement with the models, while the high velocities bins are often far away from them. It seems that there are two different behaviours in these plots. For example in the CN region (Fig. 5.14 (d)) there is an overestimation of the [N II]/[S II] ratio, while in the CS region (Fig. 5.15 (a)) there is an underestimation of the [N II]/[O II] ratio. The first

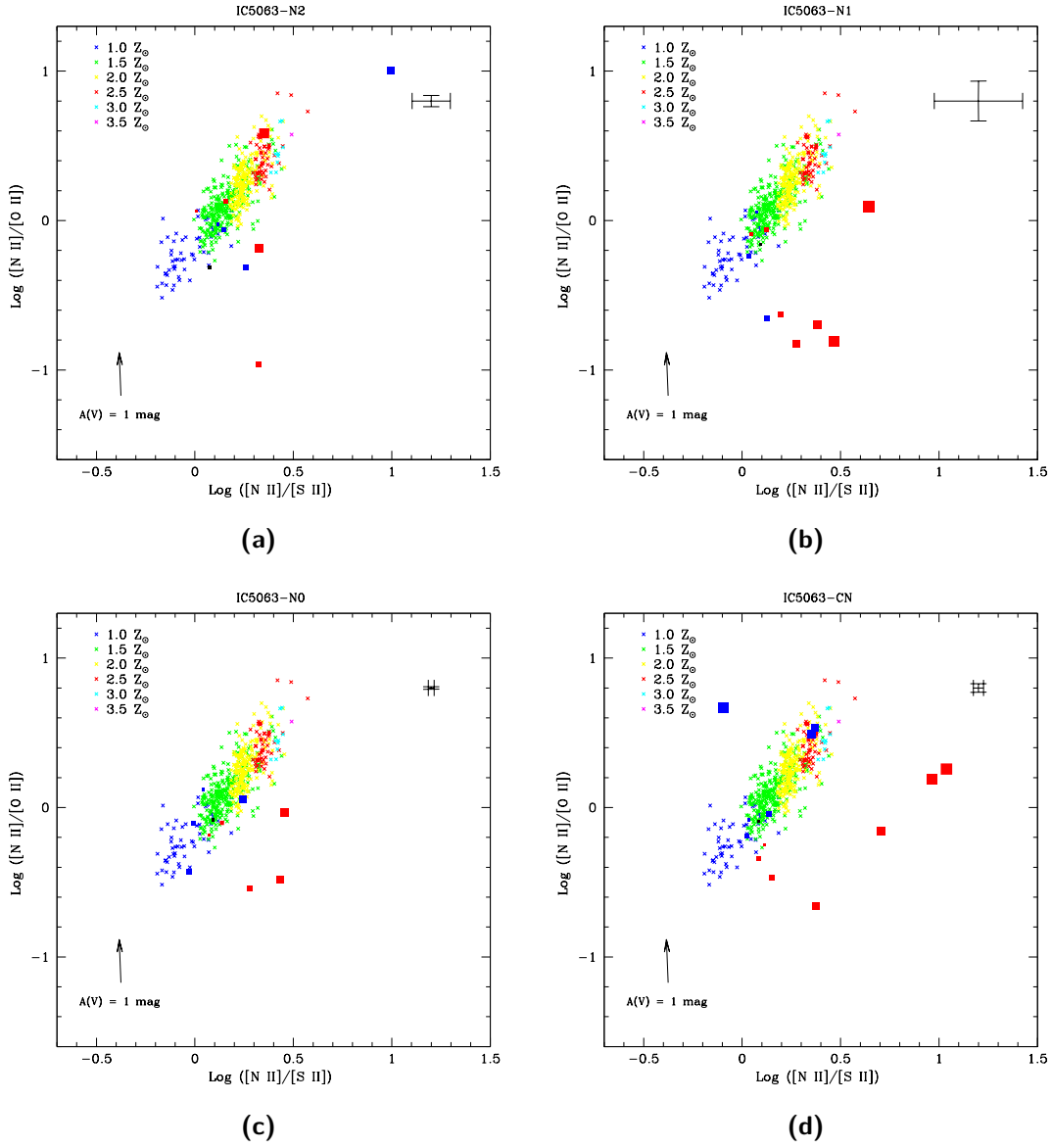

Figure 5.14: [N II]λ6584/[S II]$\lambda\lambda$6717, 6731 vs [N II]λ6584/[O II]λ3727 diagrams of IC5063 northern regions. The coloured cross are the points from the simulation by Vaona (2010). The red squares are the measurements in the $v > 0\,\mathrm{kms}^{-1}$ bins, the blue squares are the $v < 0$ bins, the black one is the $v = 0$ bin. Bigger squares correspond to higher velocities. The arrow shows the effect of the extinction for $A(V) = 1\,\mathrm{mag}$. The error bars in the up right corner of the diagrams represent the median error of the data.

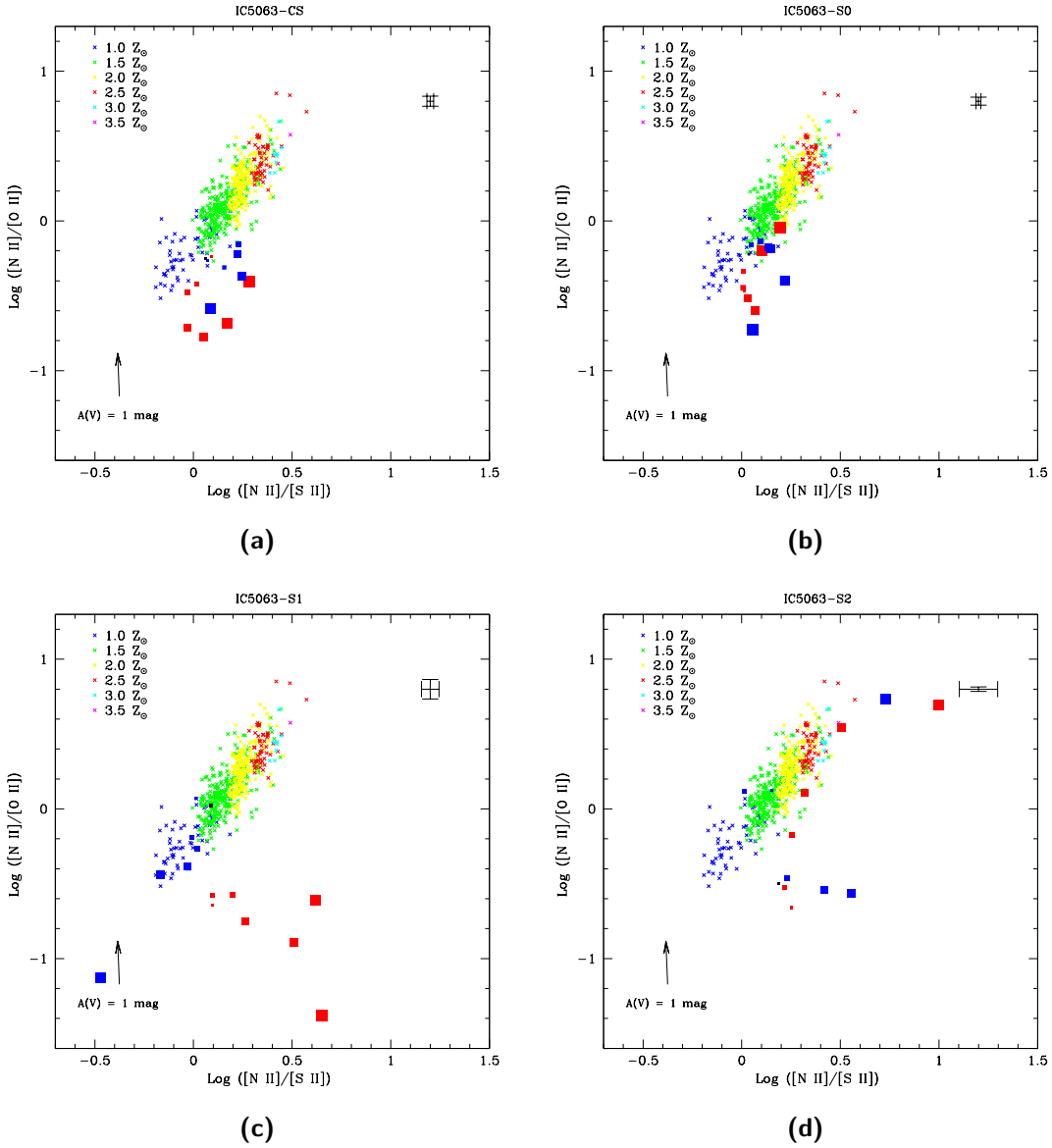

Figure 5.15: [N II]λ6584/[S II]$\lambda\lambda$6717, 6731 vs [N II]λ6584/[O II]λ3727 diagrams of IC5063 southern regions. The coloured cross are the points from the simulation by Vaona (2010). The red squares are the measurements in the $v > 0\,\mathrm{kms}^{-1}$ bins, the blue squares are the $v < 0$ bins, the black one is the $v = 0$ bin. Bigger squares correspond to higher velocities. The arrow shows the effect of the extinction for $A(V) = 1$ mag. The error bars in the up right corner of the diagrams represent the median error of the data.

ratio could be affected by the [S II] doublet deblending procedure. On the other hand, the second one is strongly affected by the extinction correction and an underestimation of the ratio could be linked to an overestimation of the extinction correction. In the northern regions, the data of low velocity bins are compatible with the simulations and they seem to suggest metallicity values between 1 and 1.5 $Z_\odot$. However, some of the high velocity data, seem to suggest very high metallicity. In the southern region there is the same trend, but with two exceptions. In the CS region it seems that there is a general overestimation of the extinction value of about 1 mag, while in the S2 region the points are randomly spread in the whole plot. It is very interesting that, in the S1 region, the $v < 0\,\mathrm{kms}^{-1}$ bins are in the $1\,Z_\odot$ section of the plot, while the $v > 0\,\mathrm{kms}^{-1}$ bins are spread away from the models. These very same points are the ones that in Fig. 5.11 (d) are pointed out as shock-wave ionized regions. But the other regions that show this behaviour in the ΔE vs [O II]λ3727/[O III]λ5007 do not show any peculiar behaviour in the metallicity diagram.

5.2 NGC5643

Hβ and [O III]λ5007 profiles are in a good agreement also in this galaxy, even if in some cases the Hβ profile is rather noisy. For example in Fig. 5.16 (a) the weak peak at v$< 0\,\mathrm{kms}^{-1}$ which is present in the [O III] line is also recognisable in the left Hβ wing. In Fig. 5.16 (c), where the Hβ profile is noisier, the general behaviour of the two profiles is compatible. The main difference can be seen in the CN region (Fig. 5.16 (b)) where [O III]λ5007 shows an evident bump at $v > 0\,\mathrm{kms}^{-1}$ that is missing in the other line profile. This disagreement could be due to a high ionization degree of the emitting gas.

Fig. 5.17 shows the comparison of the oxygen lines profiles. It is possible to see that, in the first two regions, the [O I]λ6300 and the [O III]λ5007 lines have a similar profile shape. In the CN region it is possible to see the same small difference observed also between Hβ and [O III]λ5007. In the N1 region the [O I] line is very noisy and the differences between the two profiles are remarkable. In this galaxy it is possible to see that the [O II]λ3727 line is very broad in respect to the other oxygen lines (Fig. 5.17).

In this galaxy, the [Ar IV]λ4740 line is weak and noisy, therefore I compared the [Ar IV]λ4711 line to the [O III]λ5007. The [Ar IV]λ4740 and [Fe VII]λ6087 emission lines have, in the CN region of the galaxy, a profile very similar to the [O III]λ5007 line. The argon line shows a noisy profile also in this galaxy but the average shape is the same of the oxygen line. Even in such an indented profile it is possible to observe the same asymmetry in both lines. On the other hand the iron lines has a bit larger profile than [O III]λ5007. This could mean that there are high velocity clouds with higher ionization degree.

NGC5643 shows high $A(V)$ values, as in IC5063. They are all larger than 1 mag and in the nuclear regions they exceed 2 mag. In the external regions $A(V)$ drops of about 1 mag except in the N1 region, where its value is comparable with those of the central regions. Such a high value could be due to the small S/N in the Hβ region of the spectrum. Its profile is the most indented between those of the whole galaxy. The high nuclear absorption values are expected, because Simpson et al. (1997) already pointed out a sudden drop of the [O III]/Hα ratio in the apex of the ionization cone (see Sec. 2.1.2). Looking at $A(V)$ as a function of the velocity bins it is possible to see a

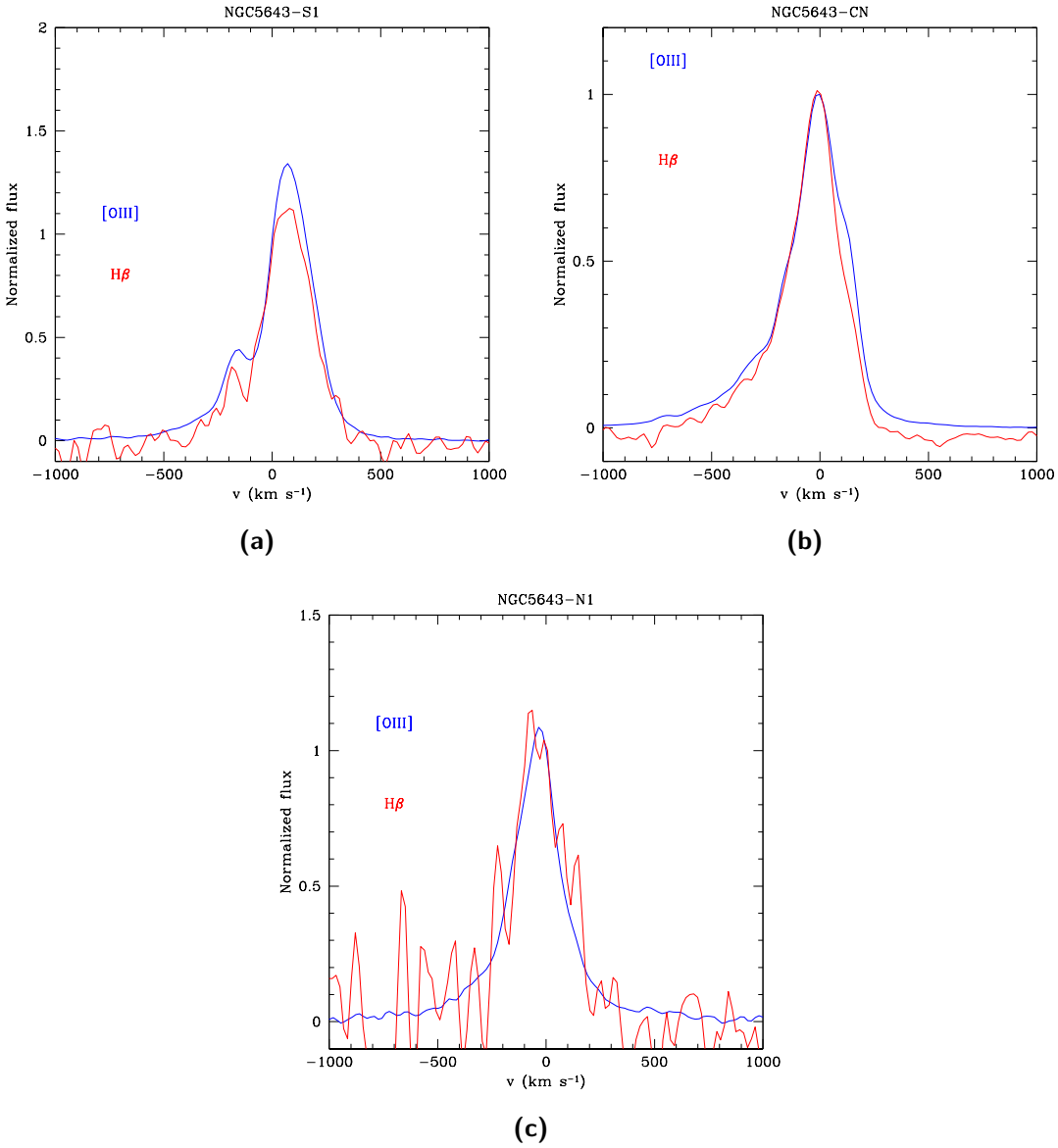

Figure 5.16: Comparison between Hβ and [O III]λ5007 in the following NGC5643 regions: CN, S1 and N1. The lines fluxes are normalized to the flux value at the rest-frame wavelength of each line.

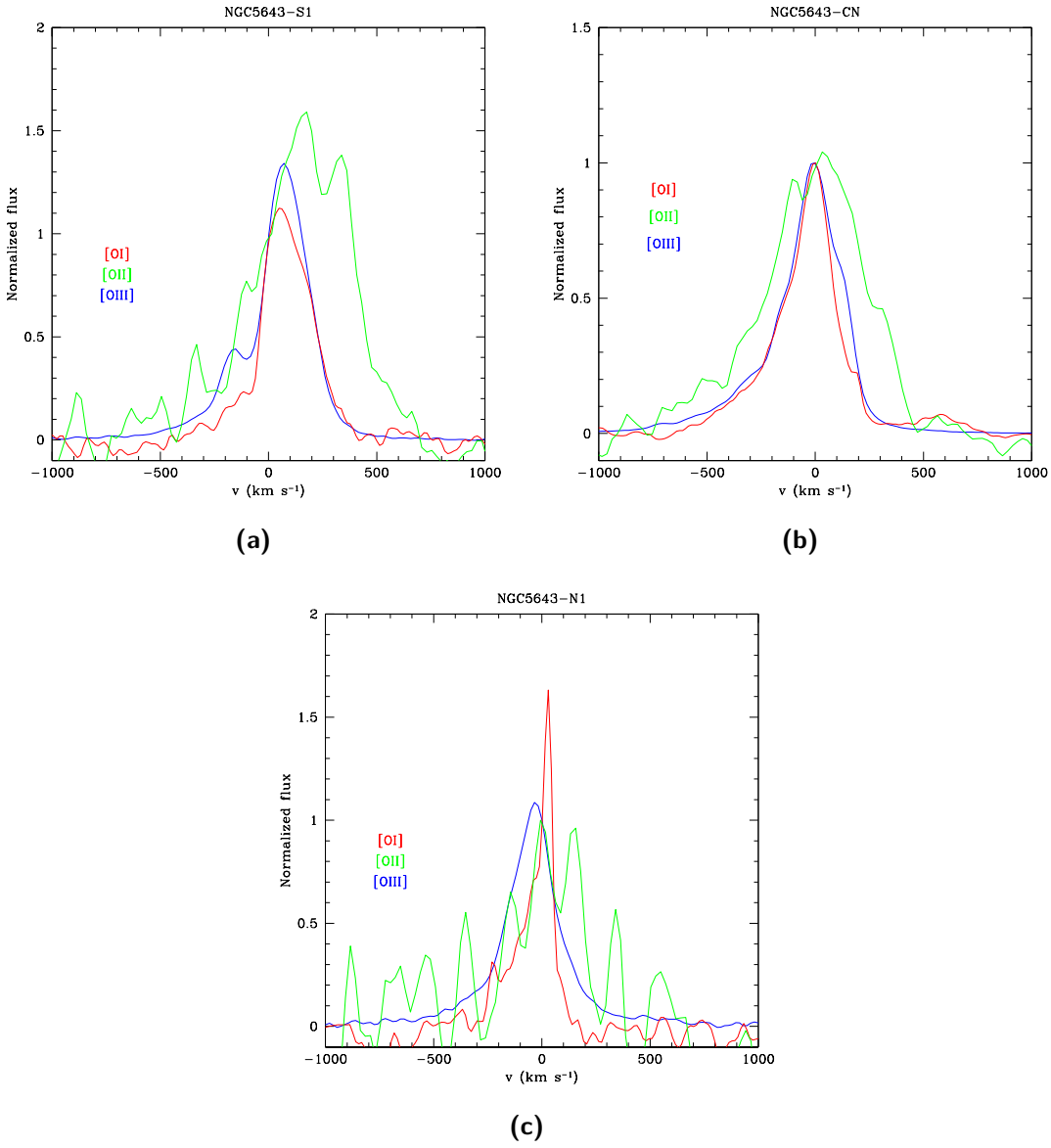

Figure 5.17: Comparison between [O I]λ6300, [O II]λ3727 and [O III]λ5007 in the same regions as before. The lines fluxes are normalized to the flux value at the rest-frame wavelength of each line.

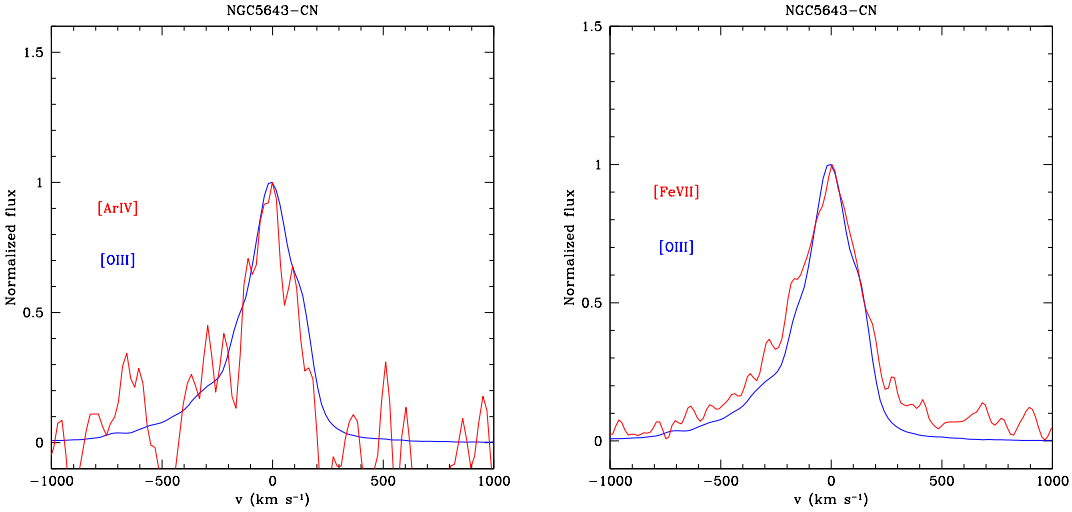

Figure 5.18: (a) Comparison between [Ar IV]λ4711 and [O III]λ5007 in the CN region. (b)Comparison between [Fe VII]λ6087 and [O III]λ5007 in the CN region. The lines fluxes are normalized to the flux value at the rest-frame wavelength of each line.

Table 5.4: Average $A(V)$ values obtained for NGC5643.

Region	$A(V)$ (mag)
S2	1.34
S1	1.03
S0	1.33
CS	2.06
CN	2.13
N0	1.14
N1	2.37

chaotic trend in most of the regions (Fig. 5.19). Only the most central regions, CN, CS, S0, show a stable $A(V)$ profile and values compatible with the average one. In all of these regions there is a peculiar tendency of $A(V)$ to decrease for $v < 0\,\mathrm{km s^{-1}}$ which cannot be easily explained. The N1 absorption plot shows the effects of the indented Hβ profile, with very scattered data. In almost all of the regions there is at least one very high $A(V)$ value in the high velocity bins. It is not clear if there is a physical reason for this behaviour or if it is an effect of the low S/N on lines wings.

Interestingly the [O III] image and the excitation map in Fig. 2.2 (b) and (c) show that the ENLR of this galaxy is composed by a small circular halo with a 1 arcsec radius centerd on the active nucleus and a single ionization cone. The farthest regions I analysed in this galaxy are at about 3 arcsec from the galactic nucleus in both directions, so in one direction I should expect to find more H II regions than power-law photoionized gas. However, it is possible to see in Fig. 5.20 and in those that follow, that the main ionization mechanism, in all of these regions, is a power-law continuum or, in some

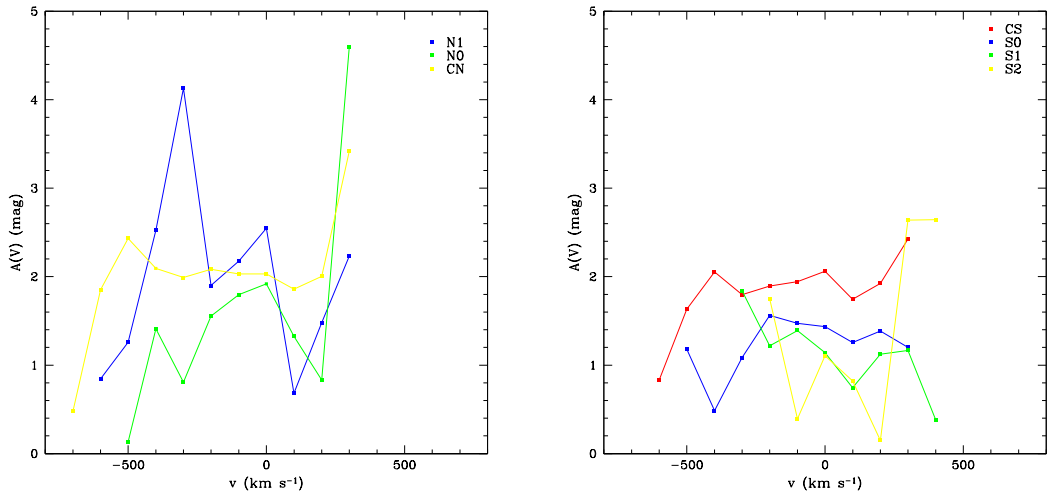

Figure 5.19: $A(V)$ vs v diagrams for NGC5643 northern regions (a) and southern regions (b).

cases, shock-waves. Therefore, these data seem to confirm the presence of another ionization cone on the other side of the galaxy which could not be seen in the images by Simpson et al. (1997).

In the first three BPT diagrams for each region, there are not any other notable features. The ΔE vs [O II]λ3727/[O III]λ5007 diagrams show that in some regions shock-ionization could be important in the gas ionization process, but there is not any striking case like the one of S1 region of IC5063. Moreover, it is possible that there is an overestimation of the number of shock-ionized regions, because as showed before, there could be an overestimation of the extinction correction in some particular cases. To overestimate the extinction value means to increase the [O II]λ3727/[O III]λ5007 ratio, because the [O II] line is more corrected than the [O III] one and the obtained ratio is larger. This does not affect the other diagrams because the involved lines are near to each other, so their ratio does not depend on the extinction correction (see Sec. 4.3).

The analysis of the ionization parameter in this galaxy is very interesting. Looking at the plots in Fig. 5.27 (a) it is possible to see that in the N0 and CN regions the ionization parameter seems to be constant in all bins at $v < 0\,\mathrm{kms}^{-1}$, with an average value of about $U \sim -2.2$. On the other hand, for $v > 0\,\mathrm{kms}^{-1}$, U starts to drop very quickly, but [O III]λ5007/Hβ (5.27 (b)) shows the opposite trend. A possible explanation for those behaviours is, again, the overestimation of the absorption, combined with very weak Hβ wings. An overestimation of $A(V)$ could bring to higher measurement of the [O II]λ3727/[O III]λ5007 ratio which is reflected in a lower value of the ionization parameter. Furthermore if the main reason of the overestimation is the weakness of the Hβ wings this could influence the measure of the [O III]λ5007/Hβ ratio, which will certainly be higher than the real one. For these reasons it is possible that the real values of the ionization parameter are near to the previously mentioned average value. Contrary to what I expected in the N1 region, the ionization parameter and the [O III]λ5007/Hβ ratio are in good agreement, even if they show quite big error bars.

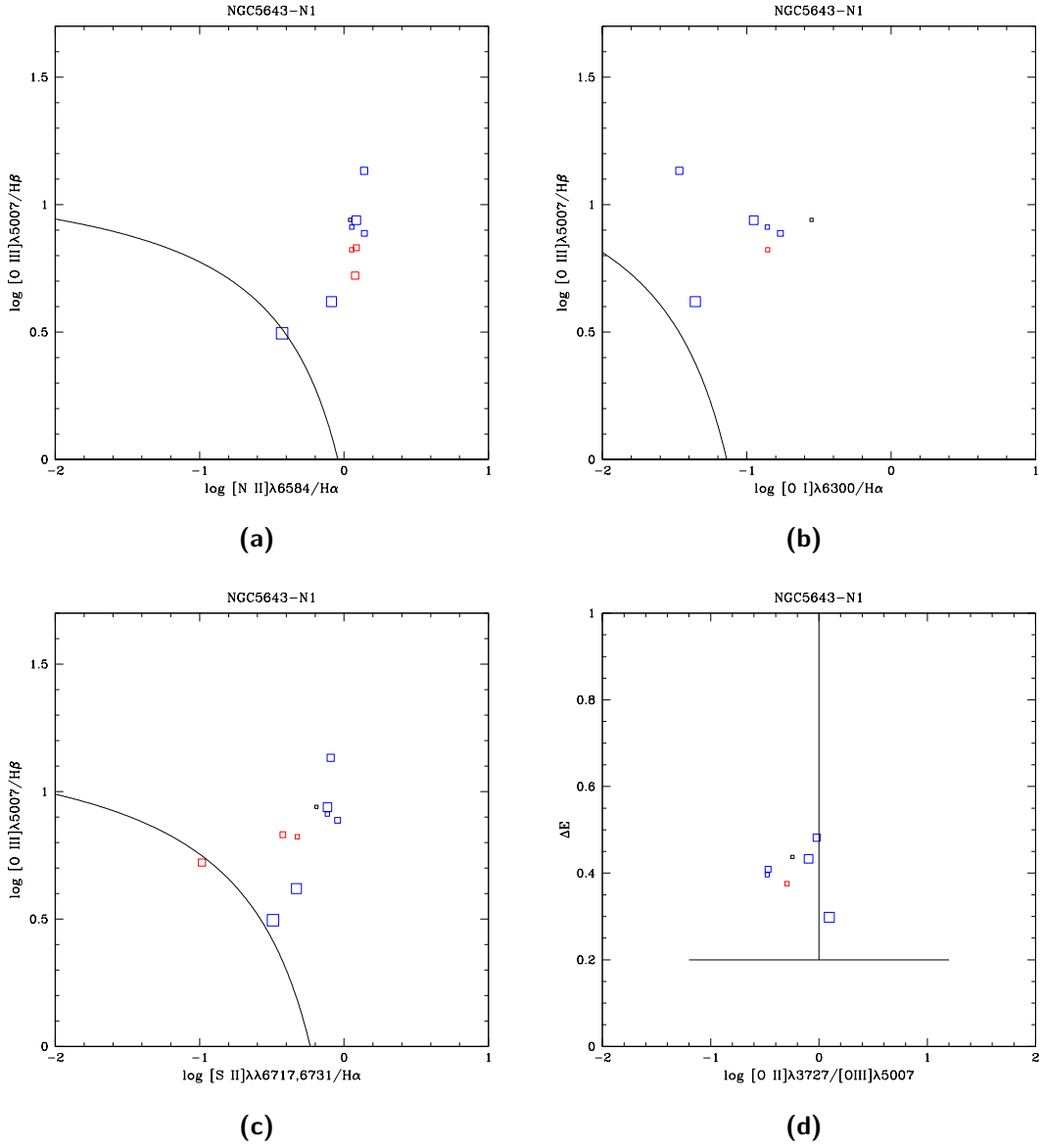

Figure 5.20: (a)[N II]λ6584/Hα vs [O III]λ5007/Hβ (b) [O I]λ6300/Hα vs [O III]λ5007/Hβ (c) [S II]$\lambda\lambda$6717, 6731/Hα vs [O III]λ5007/Hβ diagnostic diagrams for the N1 region of NGC5643. The black lines are the empirical separation between H II regions and other regions from Kewley et al. (2001). (d) ΔE vs [O II]λ3727/[O III]λ5007 diagnostic diagram for the same region. The vertical line divides the power-law ionized regions (on the left) and the shock ionized ones (on the right). The horizontal line divides the H II regions from the others. In all diagrams, red squares represent bins with $v > 0$, blue squares data with $v < 0$ and the black ones are for $v = 0$. Bigger squares correspond to higher velocities.

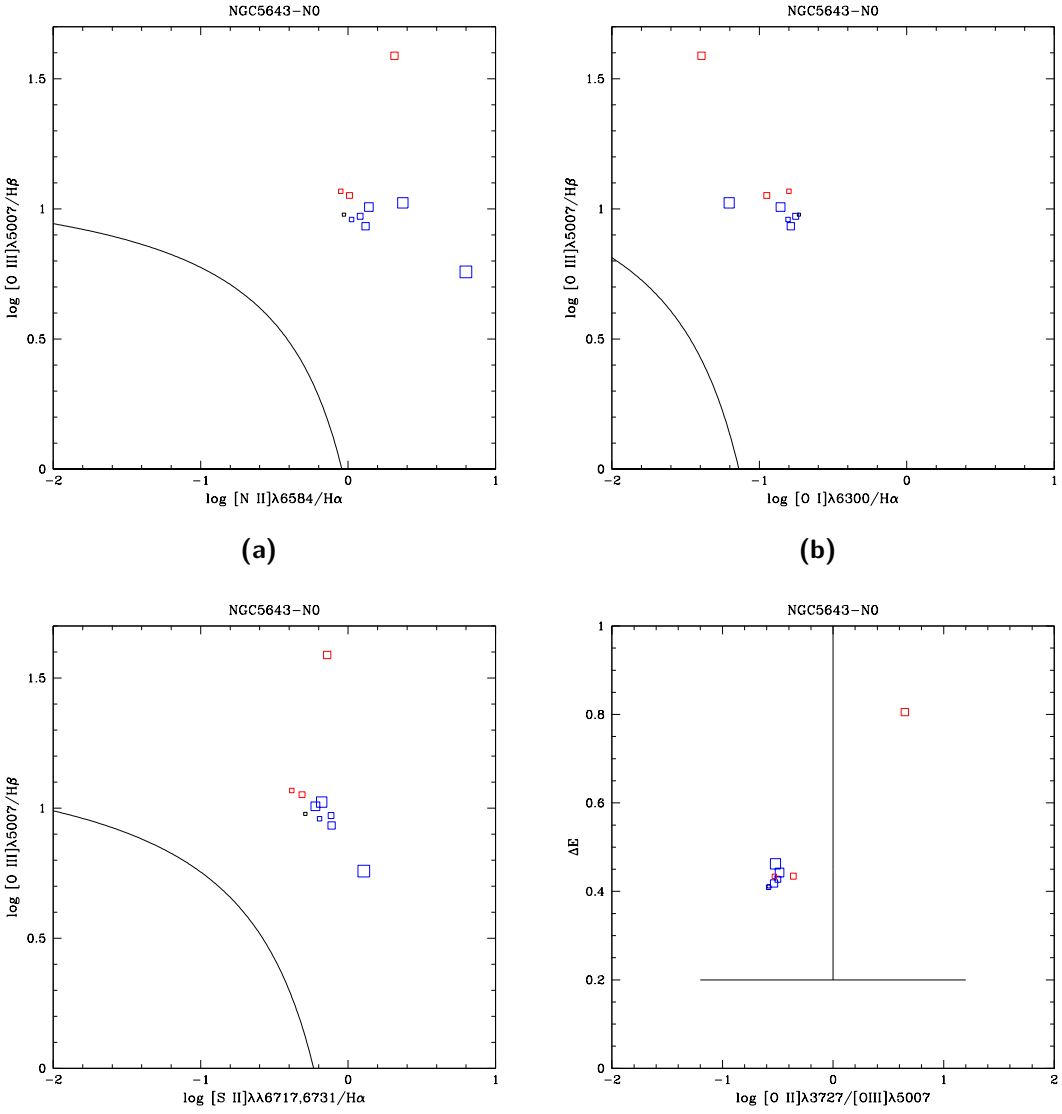

Figure 5.21: (a)[N II]λ6584/Hα vs [O III]λ5007/Hβ (b) [O I]λ6300/Hα vs [O III]λ5007/Hβ (c) [S II]$\lambda\lambda$6717, 6731/Hα vs [O III]λ5007/Hβ diagnostic diagrams for the N0 region of NGC5643. The black lines are the empirical separation between H II regions and other regions from Kewley et al. (2001). (d) ΔE vs [O II]λ3727/[O III]λ5007 diagnostic diagram for the same region. The vertical line divides the power-law ionized regions (on the left) and the shock ionized ones (on the right). The horizontal line divides the H II regions from the others. In all diagrams, red squares represent bins with $v > 0$, blue squares data with $v < 0$ and the black ones are for $v = 0$. Bigger squares correspond to higher velocities.

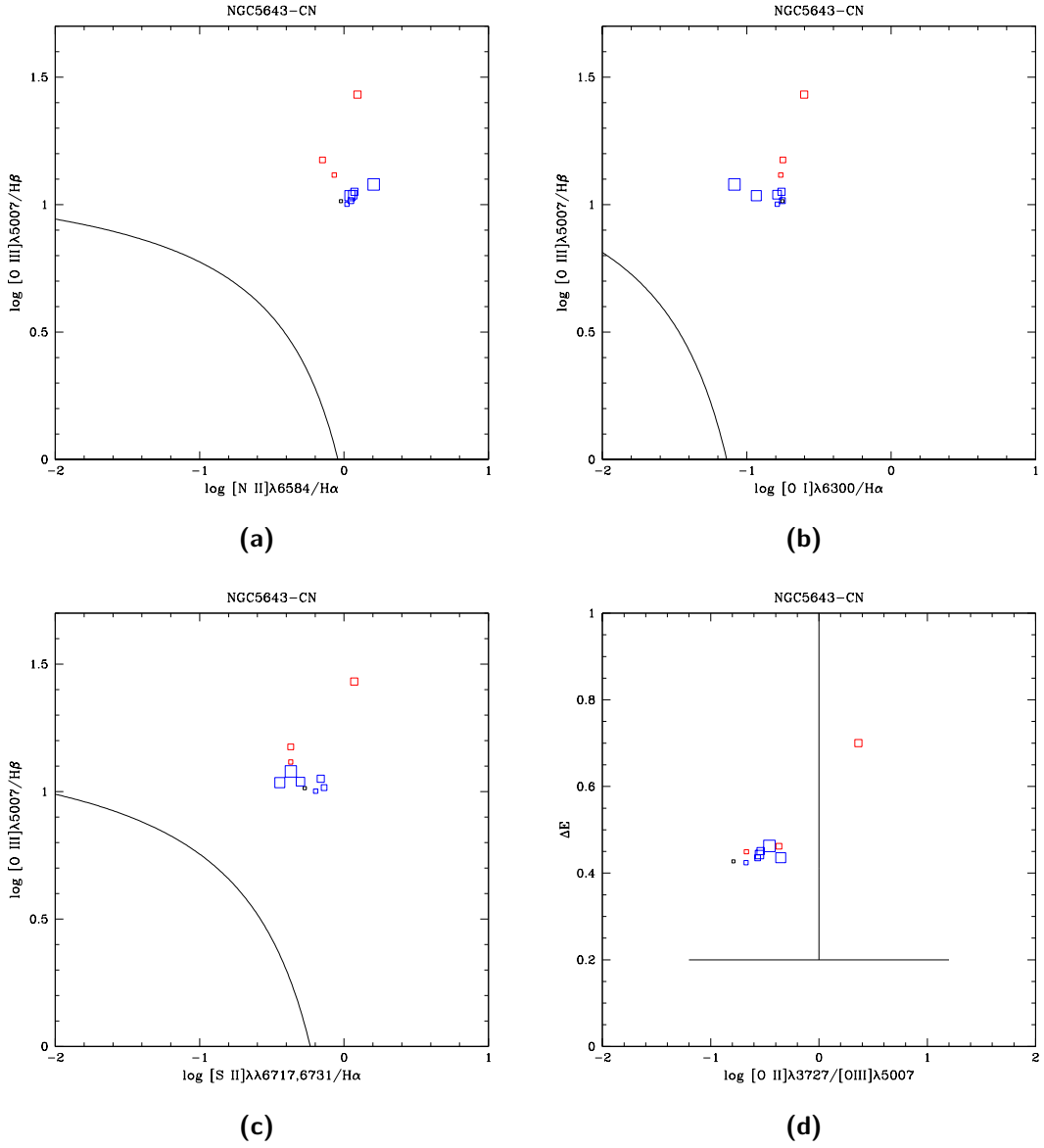

Figure 5.22: (a)[N II]λ6584/Hα vs [O III]λ5007/Hβ (b) [O I]λ6300/Hα vs [O III]λ5007/Hβ (c) [S II]$\lambda\lambda$6717, 6731/Hα vs [O III]λ5007/Hβ diagnostic diagrams for the CN region of NGC5643. The black lines are the empirical separation between H II regions and other regions from Kewley et al. (2001). (d) ΔE vs [O II]λ3727/[O III]λ5007 diagnostic diagram for the same region. The vertical line divides the power-law ionized regions (on the left) and the shock ionized ones (on the right). The horizontal line divides the H II regions from the others. In all diagrams, red squares represent bins with $v > 0$, blue squares data with $v < 0$ and the black ones are for $v = 0$. Bigger squares correspond to higher velocities.

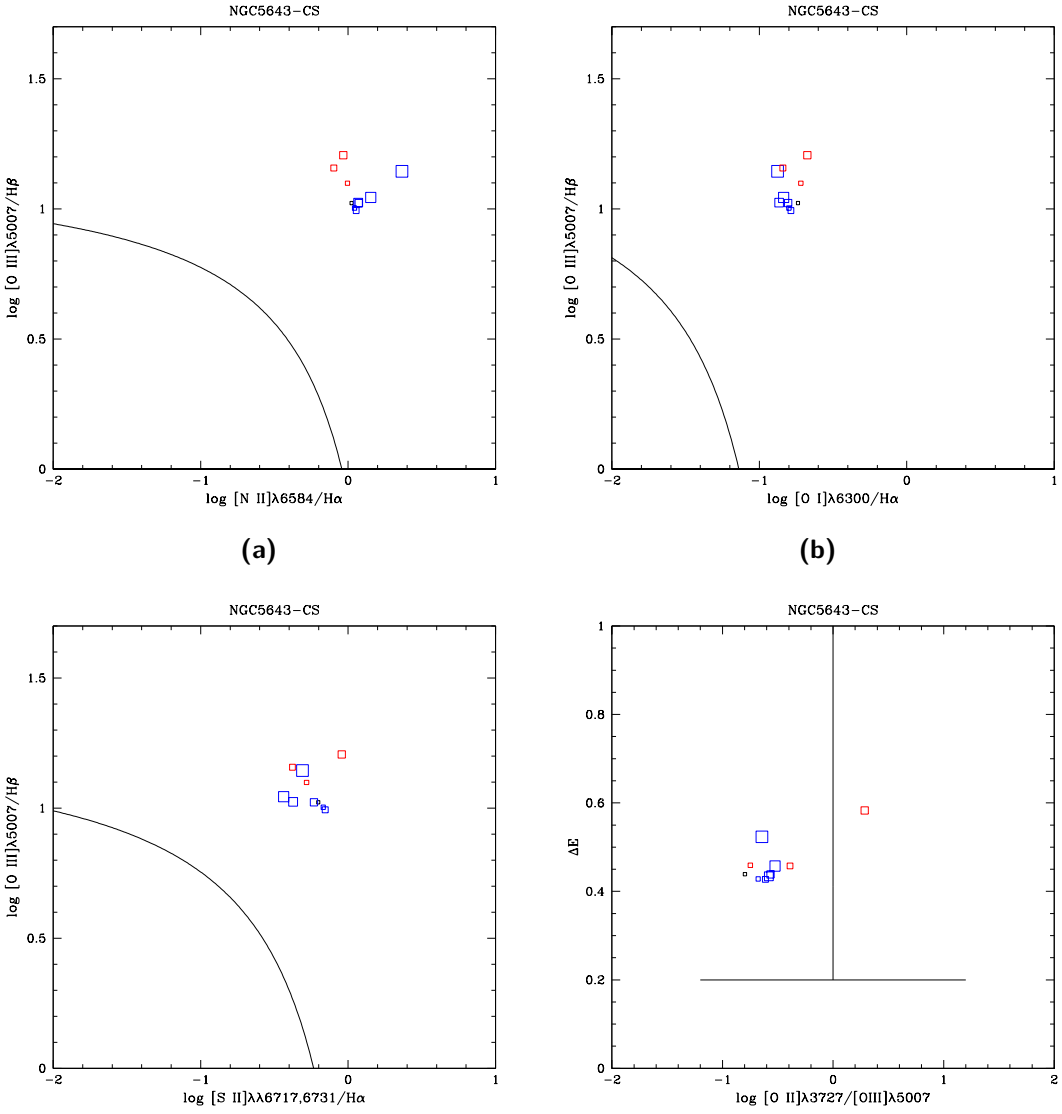

Figure 5.23: (a)[N II]λ6584/Hα vs [O III]λ5007/Hβ (b) [O I]λ6300/Hα vs [O III]λ5007/Hβ (c) [S II]$\lambda\lambda$6717, 6731/Hα vs [O III]λ5007/Hβ diagnostic diagrams for the CS region of NGC5643. The black lines are the empirical separation between H II regions and other regions from Kewley et al. (2001). (d) ΔE vs [O II]λ3727/[O III]λ5007 diagnostic diagram for the same region. The vertical line divides the power-law ionized regions (on the left) and the shock ionized ones (on the right). The horizontal line divides the H II regions from the others. In all diagrams, red squares represent bins with $v > 0$, blue squares data with $v < 0$ and the black ones are for $v = 0$. Bigger squares correspond to higher velocities.

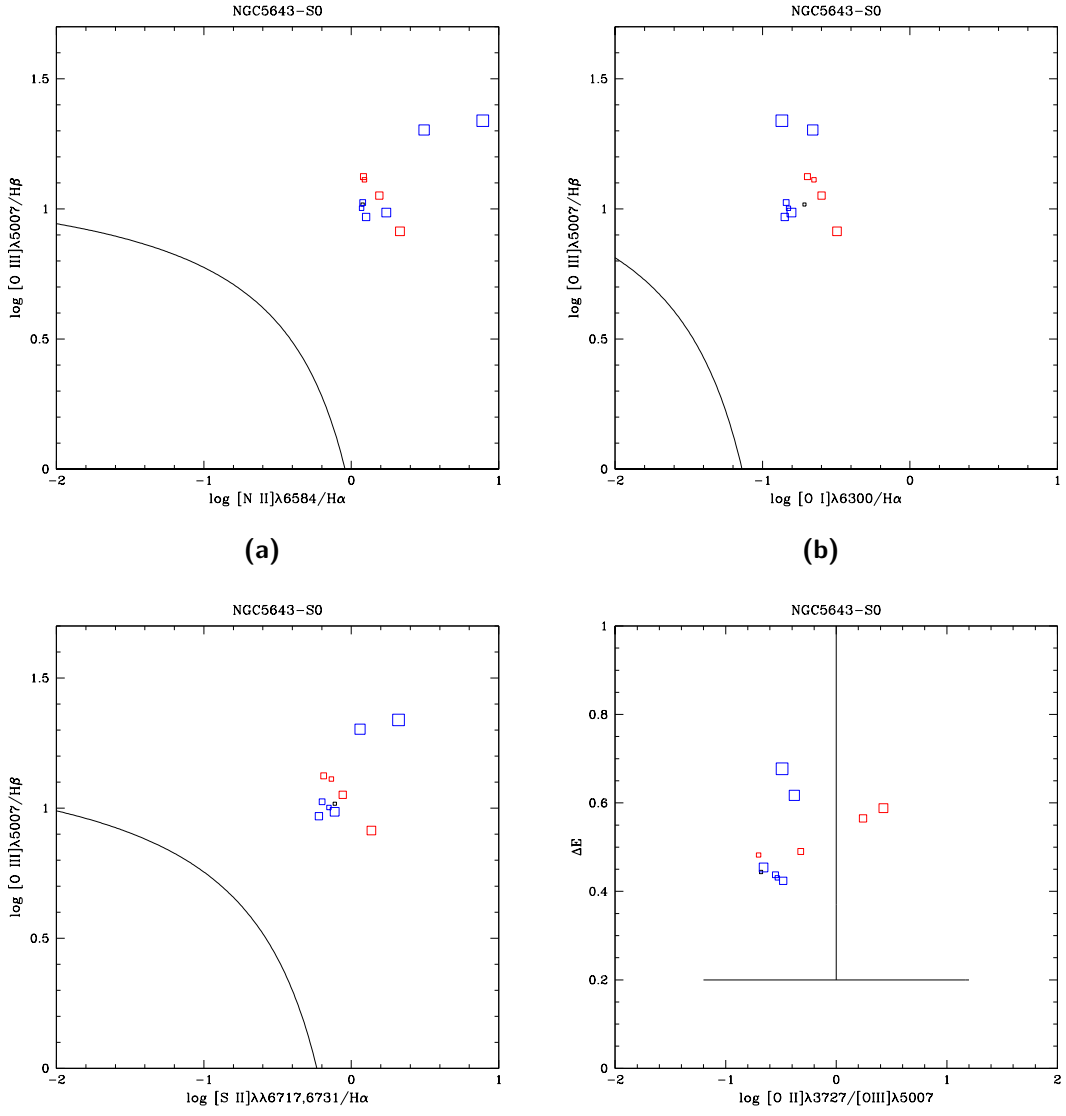

Figure 5.24: (a)[N II]λ6584/Hα vs [O III]λ5007/Hβ (b) [O I]λ6300/Hα vs [O III]λ5007/Hβ (c) [S II]$\lambda\lambda$6717, 6731/Hα vs [O III]λ5007/Hβ diagnostic diagrams for the S0 region of NGC5643. The black lines are the empirical separation between H II regions and other regions from Kewley et al. (2001). (d) ΔE vs [O II]λ3727/[O III]λ5007 diagnostic diagram for the same region. The vertical line divides the power-law ionized regions (on the left) and the shock ionized ones (on the right). The horizontal line divides the H II regions from the others. In all diagrams, red squares represent bins with $v > 0$, blue squares data with $v < 0$ and the black ones are for $v = 0$. Bigger squares correspond to higher velocities.

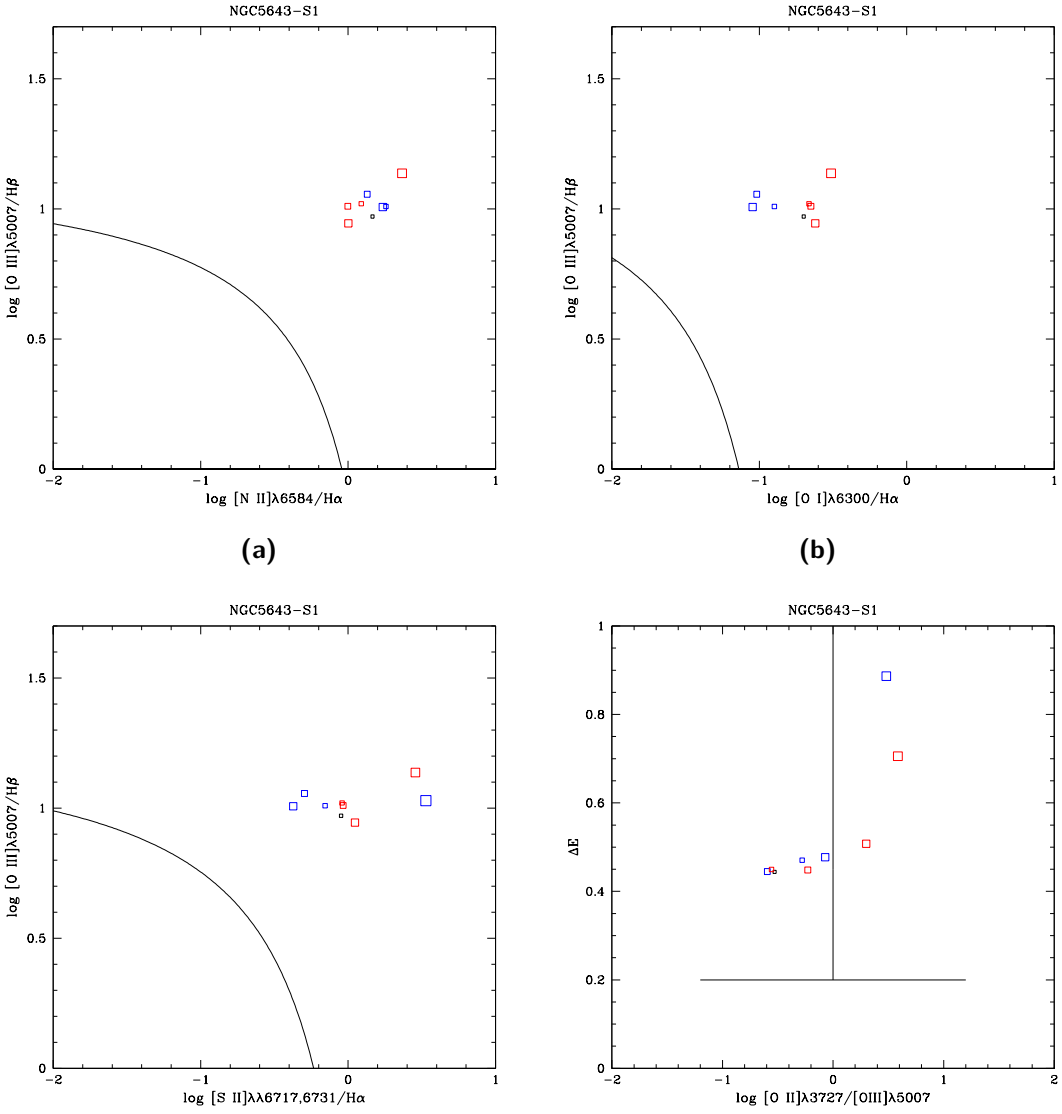

Figure 5.25: (a)[N II]λ6584/Hα vs [O III]λ5007/Hβ (b) [O I]λ6300/Hα vs [O III]λ5007/Hβ (c) [S II]$\lambda\lambda$6717, 6731/Hα vs [O III]λ5007/Hβ diagnostic diagrams for the S1 region of NGC5643. The black lines are the empirical separation between H II regions and other regions from Kewley et al. (2001). (d) ΔE vs [O II]λ3727/[O III]λ5007 diagnostic diagram for the same region. The vertical line divides the power-law ionized regions (on the left) and the shock ionized ones (on the right). The horizontal line divides the H II regions from the others. In all diagrams, red squares represent bins with $v > 0$, blue squares data with $v < 0$ and the black ones are for $v = 0$. Bigger squares correspond to higher velocities.

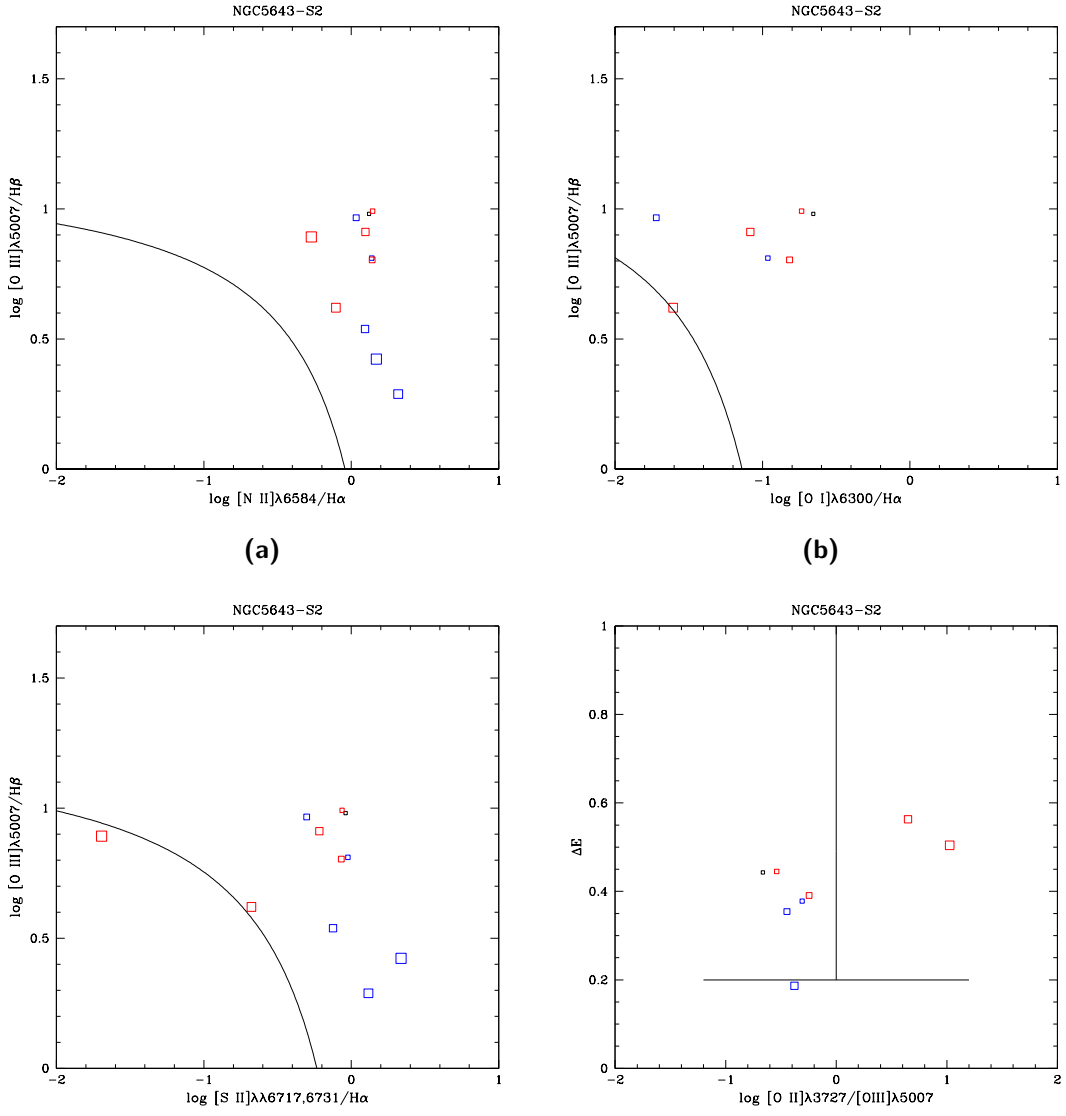

Figure 5.26: (a)[N II]λ6584/Hα vs [O III]λ5007/Hβ (b) [O I]λ6300/Hα vs [O III]λ5007/Hβ (c) [S II]$\lambda\lambda$6717, 6731/Hα vs [O III]λ5007/Hβ diagnostic diagrams for the S2 region of NGC5643. The black lines are the empirical separation between H II regions and other regions from Kewley et al. (2001). (d) ΔE vs [O II]λ3727/[O III]λ5007 diagnostic diagram for the same region. The vertical line divides the power-law ionized regions (on the left) and the shock ionized ones (on the right). The horizontal line divides the H II regions from the others. In all diagrams, red squares represent bins with $v > 0$, blue squares data with $v < 0$ and the black ones are for $v = 0$. Bigger squares correspond to higher velocities.

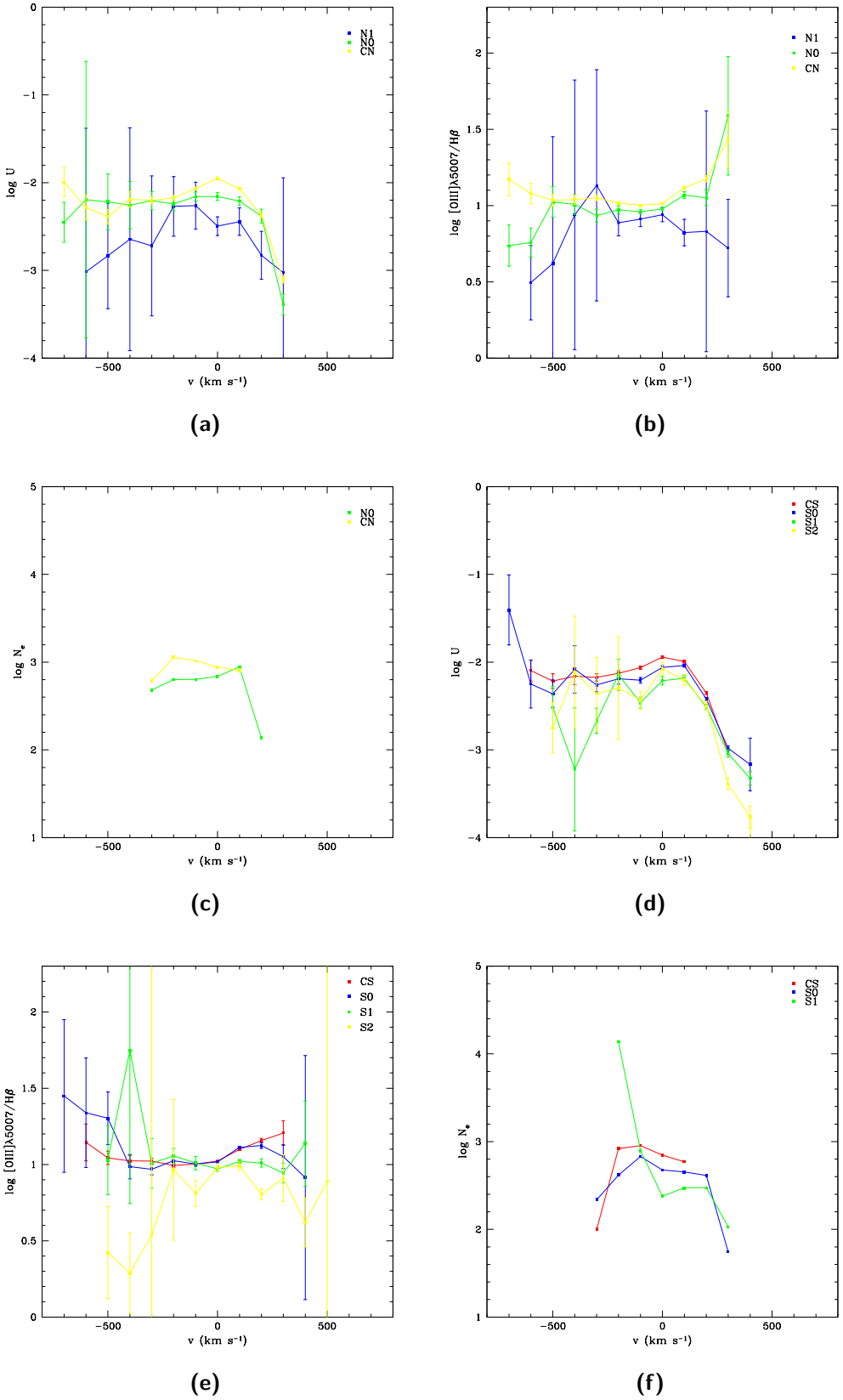

Figure 5.27: U vs v,[O III]λ5007/Hβ vs v and N_e vs v diagrams for the northern regions (in the first three graphics) and southern regions (in the last three).

Table 5.5: Temperature and density in NGC5643.

	Low Ionization		High Ionization	
Region	T (K)	n_e (cm^{-3})	T (K)	n_e (cm^{-3})
S1	9011.7	96.6	-	-
S0	10357.9	404.1	-	-
CS	11318.8	379.1	13585.6	4947.54
CN	10242.7	591.7	12981.3	6410.73
N0	12833.5	572.6	-	-

This could mean that the absorption correction in the region is not bad. U is about constant in all of the velocity bins, inside the error bars. About the southern regions, they show the same behaviour of the region CN and N0. For $v < 0\,\mathrm{kms}^{-1}$ U is constant and its average values is $U \sim -2.2$, except for the S2 region where there is a high data dispersion. For $v > 0\,\mathrm{kms}^{-1}$ the ionization parameter value drops quickly. Here the problem is that [O III]λ5007/Hβ is nearly constant in all of the velocity bins, so maybe my previous explanation cannot explain this situation. Moreover the error bars on $\log U$ are quite small. However, it is possible that an overestimation of $A(V)$ in which both Hα and Hβ wings are noisy, can be the explanation to this problem.

In this galaxy there is also a dependence of the ionization parameter profile on the distance from the galactic nucleus. The U profile of more distant regions is slightly lower than that of nearer ones in both sides of the galaxy and this is expected if the only ionization source is the central AGN (Ozaki 2009).

It is clear from Tab. 5.5 that in NGC5643 I could not measure temperature and electron density in all of the studied region and, in particular, I was able to measure the highly ionized gas temperature and density only in the nucleus of the galaxy, because all the needed lines were not visible in other regions. Nevertheless, it is easy to see that the high ionization gas density is higher than the low ionization gas density. Also the temperature shows such a behaviour, but the differences are smaller. However the measured temperatures are inside the theoretical limits for photoionized gas. Also in this galaxy I tried to measure the density in the velocity bins using the [S II] lines. It is possible to see in Fig. 5.27 (c) and (f) that I could do the measurement only in the most central regions and for low values of $|v|$. LogN_e is quite constant for $v \sim 0$, and in most of the cases it decreases for slightly higher values of $|v|$. It is possible that this behaviour and the problems in measuring the electron density are due to the lines deblending method.

The general situation about metallicity is the same of the previous galaxy. The points of the low velocity bins are, more or less, near the areas covered by models, and they seem to indicate high metallicity values, from 1.5 to 2.5 $\mathrm{Z}_{\odot}$. An overestimation of about 0.5 mag of the $A(V)$ values could explain most of the points outside the models area, in almost all of the galaxy regions. Furthermore, the two bins of S2 at $v > 0\,\mathrm{kms}^{-1}$ are classified as shock-ionized regions by the diagnostic diagram in Fig. 5.26 (d). Fig. 5.25 panel (d) identifies three velocity bins as shock-ionized and they are the ones in the lower part of Fig. 5.29 (c), confirming that this kind of simulations are not able to estimate the metallicity in shock-ionized regions. However, there are other data

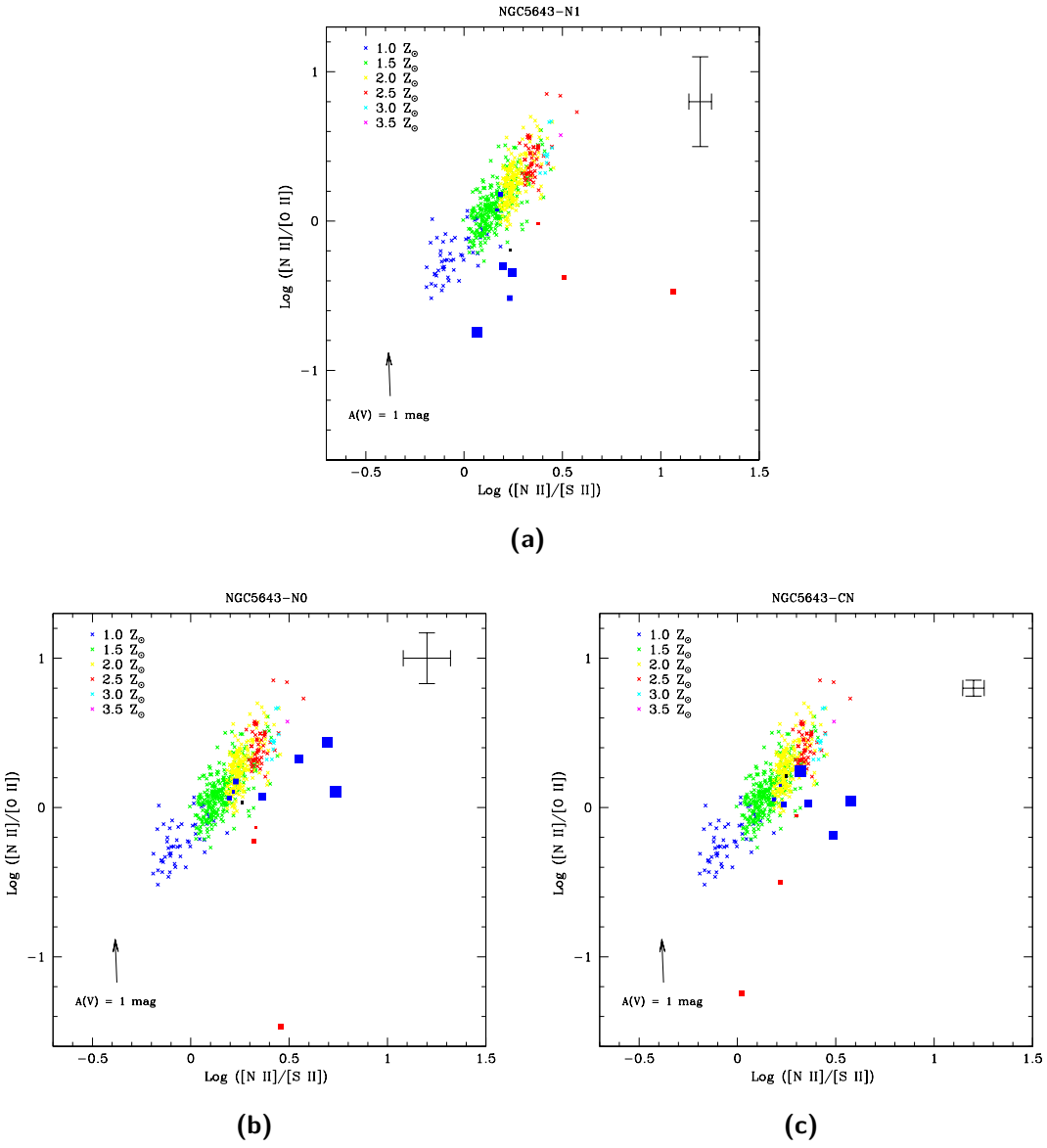

Figure 5.28: [N II]λ6584/[S II]$\lambda\lambda$6717, 6731 vs [N II]λ6584/[O II]λ3727 diagrams of NGC5643 northern regions. The coloured cross are the points from the simulation by Vaona (2010). The red squares are the measurements in the $v > 0\,\mathrm{kms}^{-1}$ bins, the blue squares are the $v < 0$ bins, the black one is the $v = 0$ bin. Bigger squares correspond to higher velocities. The arrow shows the effect of the extinction for $A(V) = 1\,\mathrm{mag}$. The error bars in the up right corner of the diagrams represent the median error of the data.

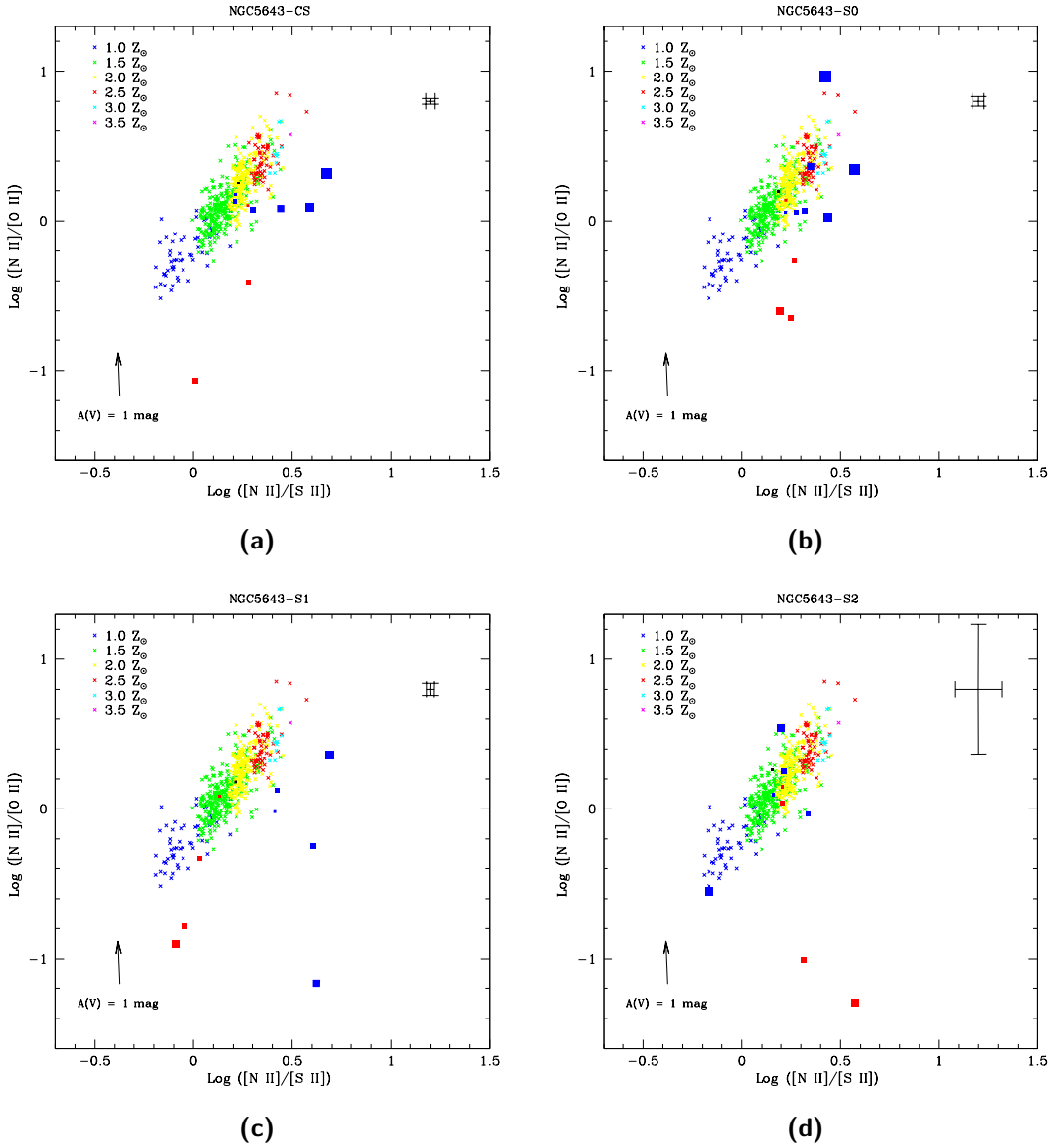

Figure 5.29: [N II]λ6584/[S II]$\lambda\lambda$6717, 6731 vs [N II]λ6584/[O II]λ3727 diagrams of NGC5643 southern regions. The coloured cross are the points from the simulation by Vaona (2010). The red squares are the measurements in the $v > 0\,\mathrm{kms}^{-1}$ bins, the blue squares are the $v < 0$ bins, the black one is the $v = 0$ bin. Bigger squares correspond to higher velocities. The arrow shows the effect of the extinction for $A(V) = 1$ mag. The error bars in the up right corner of the diagrams represent the median error of the data.

outside the models area, whose position could be only explained as inaccuracies in the flux measurement due to the deblending process.

5.3 NGC7212

NGC7212 is the last galaxy that I studied. By analyzing the lines profiles(Fig. 5.30), it is possible to see that in the N1 and CN regions, Hβ and [O III]λ5007 show a rather similar profile, even if in the N1 region Hβ is slightly weaker than [O III] for $v \sim 0\,\mathrm{kms}^{-1}$. In the S1 region instead, the two profiles are very different. For $v > -100\,\mathrm{kms}^{-1}$ the lines shape is similar, but, for $v < -100\,\mathrm{kms}^{-1}$, H$\beta$ shows a strong peak which is not present in the [O III] line.

Also the three oxygen lines reported in Fig. 5.31 (a) have different profiles, but it is possible to see that [O I] seems to have a peak in the same position of Hβ. In the CN region the tree lines have very similar profiles, while in the N1 region the profiles of [O I] and [O III] are similar but the [O III] line seems to be a little weaker.

In Fig. 5.32 it is possible to see the plots of the [Ar IV]λ4740 and [Fe VII]λ6087 compared with the [O III]λ5007 line. Unfortunately the argon line is very noisy. However it seems to be a quite wide line and the average profile could be similar to the [O III]λ5007 line. Also the [Fe VII]λ6087 line is quite noisy with respect to the lines of the other galaxies. It also seems to be relatively stronger at low velocities ($\pm 300\,\mathrm{kms}^{-1}$) with respect to the oxygen line and it could mean that there are very highly ionized clouds which are moving at low velocity in the ENLR.

NGC7212 is the galaxy in my sample that shows the lower values of the average $A(V)$ (Tab. 5.6). In the nuclear regions there are the highest values and they are around $A(V) \sim 1.5\,\mathrm{mag}$, in the external regions the absorption value drops quickly until it arrives to 0.32 mag in the region S1 and 0.42 mag in N1. The region N2 shows a sudden rise of $A(V)$ to the values typical of the nucleus, but in this region the spectrum around Hβ is quite noisy, so it is difficult to measure the right value of Hβ flux. Unexpectedly these absorption values are lower than those measured by Bisigello (2012) who uses the same spectra of this work. The two different deblending methods and the different division of the galaxy in regions, could be the reason of the disagreement between the measurements of the two works. There is also a difference in the $A(V)$ radial trend, because Bisigello (2012) and Cracco et al. (2011) measured that $A(V)$ increases with the increasing of the distance from the nucleus of the galaxy. However, it is possible to see in Fig. 5.33 that the absorption values measured in the low velocity bins confirm the average values. By analizing the $A(V)$ behaviour in function of the velocity, it is possible to see that, in the region with higher S/N ratio, the absorption value tends to increase in the high velocity bins. In the N1 region it was possible to measure the values only at low velocities, from -300 up to $+200\,\mathrm{kms}^{-1}$, and $A(V)$ seems to be almost constant. In the other external regions there are few data and the $A(V)$ profile is quite indented.

By considering the diagnostic diagrams it is possible to see that there is not any region in which the main ionization sources are hot stars. All of the measured points are above the empirical function from Kewley et al. (2001) meaning that there is not any H II region in the gas I analysed. Only in the ΔE vs [O II]λ3727/[O III]λ5007 diagram (Fig. 5.36 (d) and 5.38 (d)) there are some points in the section occupied by the H II

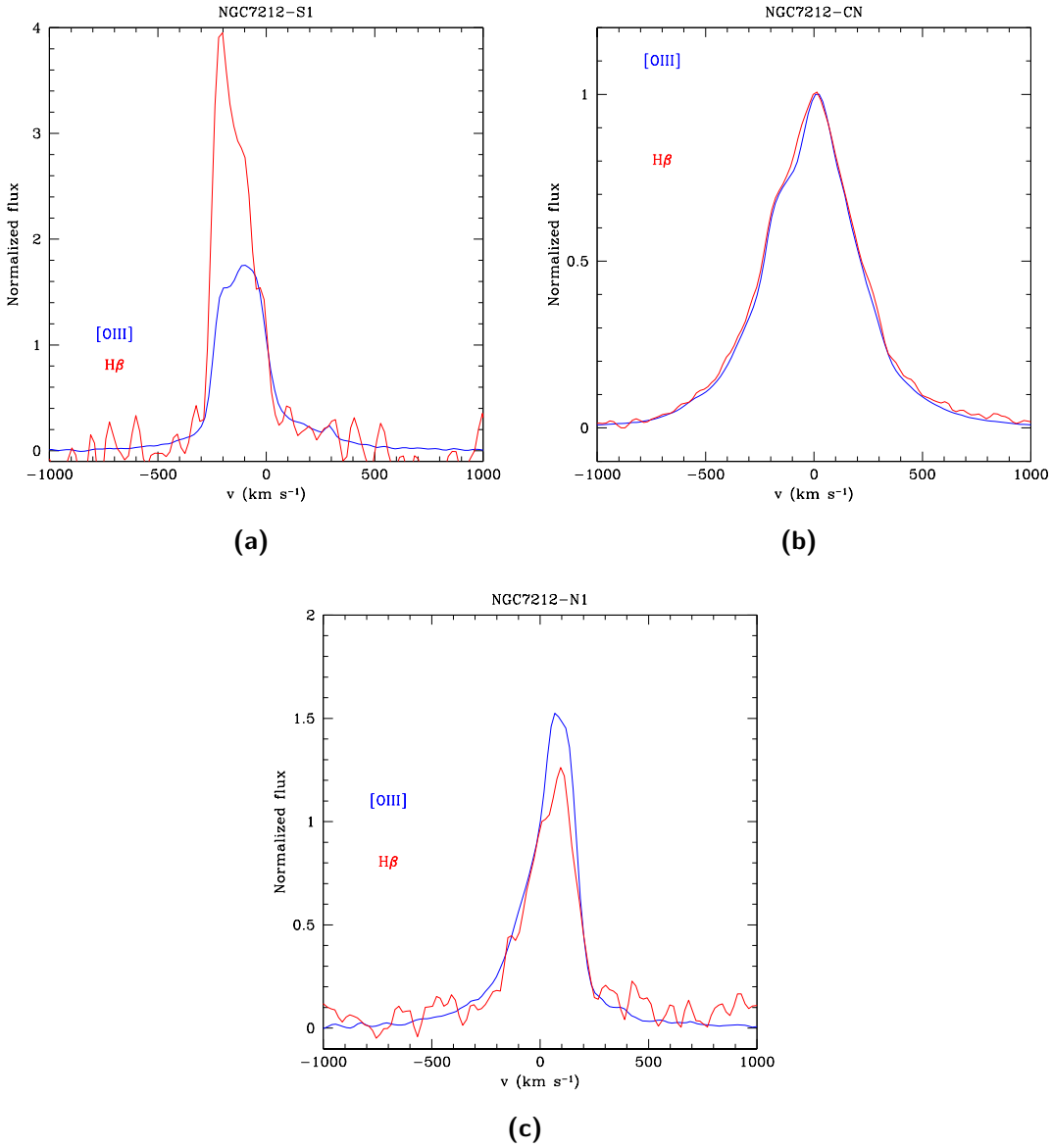

Figure 5.30: Comparison between Hβ and [O III]λ5007 in the following NGC7212 regions: CN, S1 and N1. The lines fluxes are normalized to the flux value at the rest wavelength of each line.

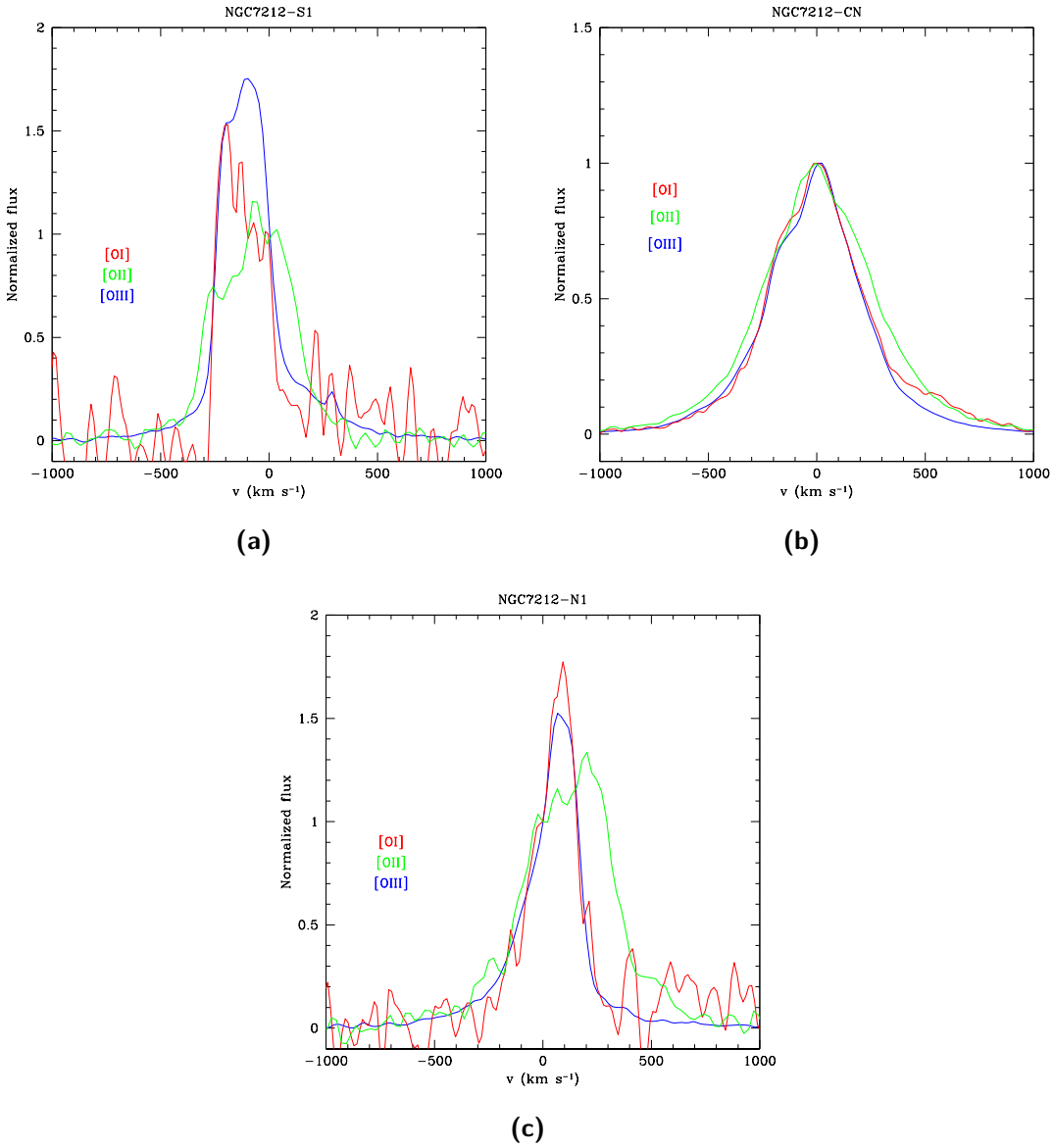

Figure 5.31: Comparison between [O I]λ6300, [O II]λ3727 and [O III]λ5007 in the same regions as before. The lines fluxes are normalized to the flux value at the rest wavelength of each line.

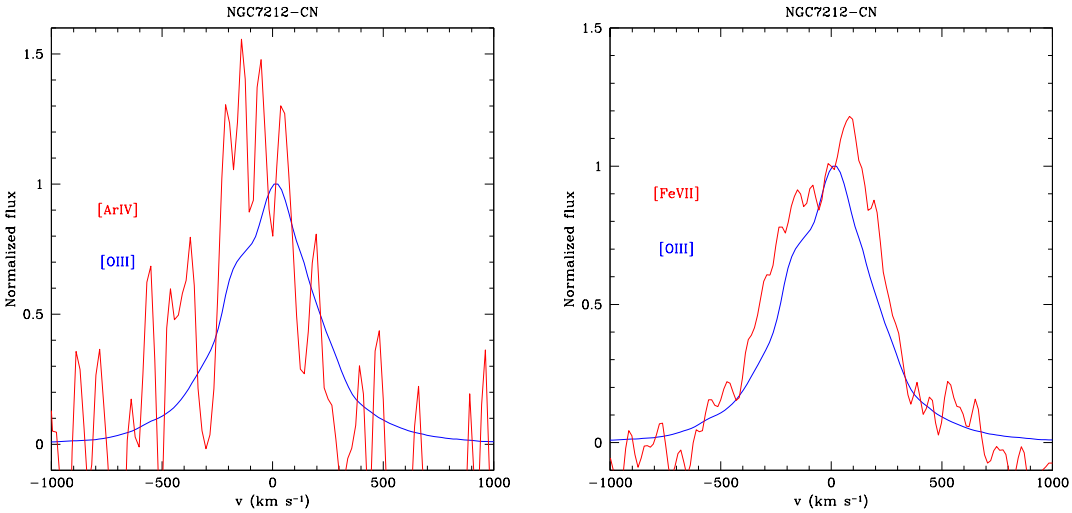

Figure 5.32: (a) Comparison between [Ar IV]λ4740 and [O III]λ5007 in the CN region. (b)Comparison between [Fe VII]λ6087 and [O III]λ5007 in the CN region. The lines fluxes are normalized to the flux value at the rest wavelength of each line.

Table 5.6: $A(V)$ values obtained for NGC7212 in this work and by Bisigello (2012). For her values there are the distances from the nucleus of the region where they were measured.

Region	R (arcsec)	$A(V)$ (mag)	R (arcsec)	$A(V)$ (mag)	
				4.0	2.04
S1		3.0	0.32	3.0	1.39
S0		1.8	0.86	2.0	1.18
CS		0.6	1.64	1.0	0.09
CN		0.6	1.61	0.0	1.40
N0		1.8	1.55	1.0	1.93
N1		3.0	0.95	2.0	1.60
N2		4.5	1.63	3.0	2.08
			4.0	2.69	

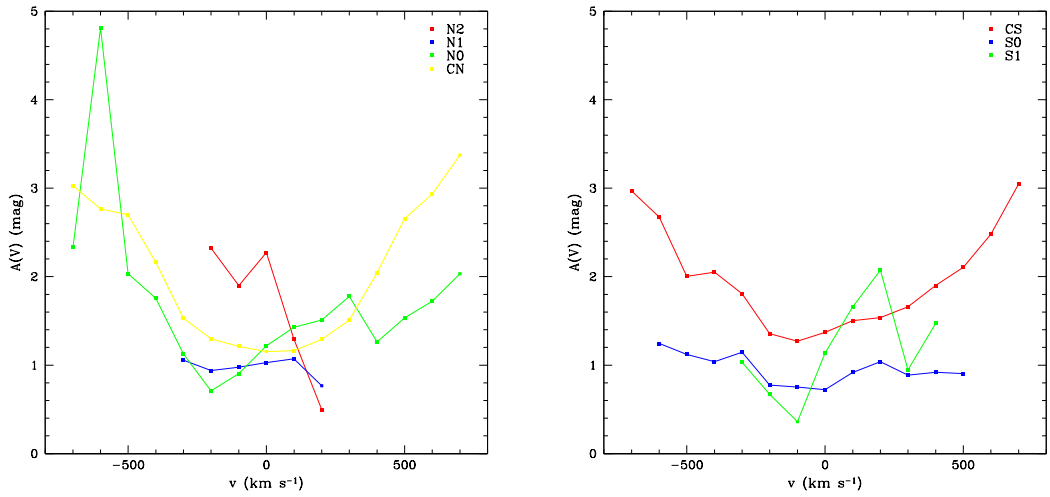

(a) **(b)**

Figure 5.33: $A(V)$ vs v diagrams for NGC5643 northern regions (a) and southern regions (b).

Table 5.7: Temperature and density in NGC7212.

	Low Ionization		High Ionization	
Region	T (K)	n_e (cm^{-3})	T (K)	n_e (cm^{-3})
S0	12006.2	217.9	-	-
CS	15671.2	755.2	-	-
CN	15734.3	505.3	-	-
N0	8823.2	850.8	-	-
N1	14911.2	492.4	-	-

region, but there is not any confirmation by the other diagrams. The same diagram shows that there are some regions in which shock-waves are important in ionizing the gas and it is possible to see in Fig. 5.35 (d) and 5.36 (d) that in some of the regions only the velocity bins with $v > 0\,\mathrm{kms}^{-1}$ could be shock-ionized.

The ionization parameter in Fig. 5.41 (a) and (c) shows quite a smooth behaviour in the nuclear regions (N0, CN, CS). It is constant in the low velocity bins and it goes down very smoothly in the high velocity bins, probably because the electron density increases in those regions (see Fig. 5.41 (c-f)). The general behaviour in these regions is confirmed by [O III]λ5007/Hβ. There is a good agreement between those two trends also for the external regions where there are more noisy $\log U$ profiles, especially for $v > 0\,\mathrm{kms}^{-1}$. In the velocity bins where there is no agreement, in some cases, there are large error bars, so it is possible that the real behaviours are compatible. It is also possible to see that the CN region has an ionization parameter profile that is slightly higher than the N0 one, and this could be a sign of the dependence of U on the distance from the ionization source. It is not possible to see anything about the other regions, because they have too much noisy profiles.

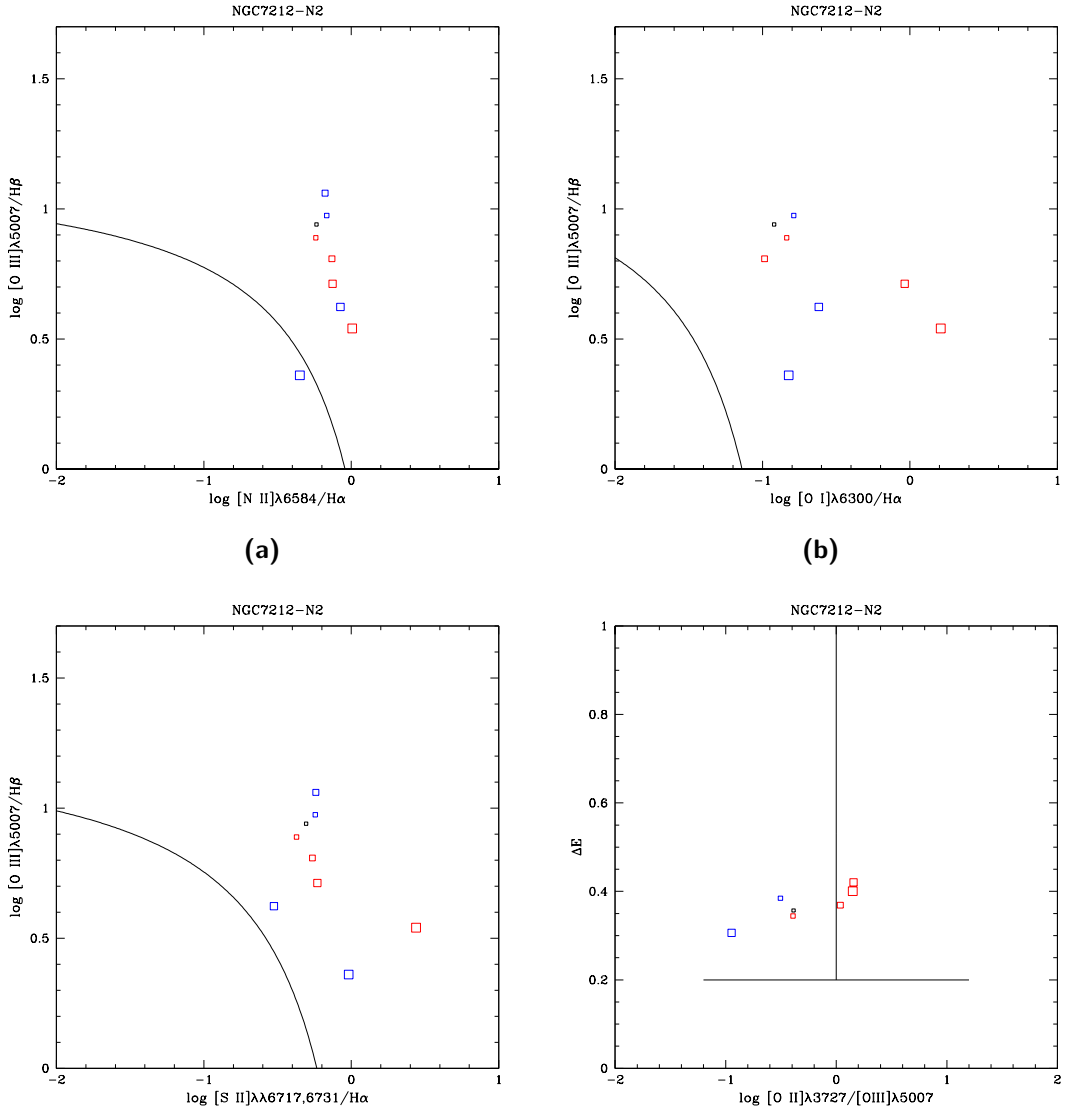

Figure 5.34: (a)[N II]λ6584/Hα vs [O III]λ5007/Hβ (b) [O I]λ6300/Hα vs [O III]λ5007/Hβ (c) [S II]$\lambda\lambda$6717, 6731/Hα vs [O III]λ5007/Hβ diagnostic diagrams for the N2 region of NGC7212. The black lines are the empirical separation between H II regions and other regions from Kewley et al. (2001). (d) ΔE vs [O II]λ3727/[O III]λ5007 diagnostic diagram for the same region. The vertical line divides the power-law ionized regions (on the left) and the shock ionized ones (on the right). The horizontal line divides the H II regions from the others. In all diagrams, red squares represent bins with $v > 0$, blue squares data with $v < 0$ and the black ones are for $v = 0$. Bigger squares correspond to higher velocities.

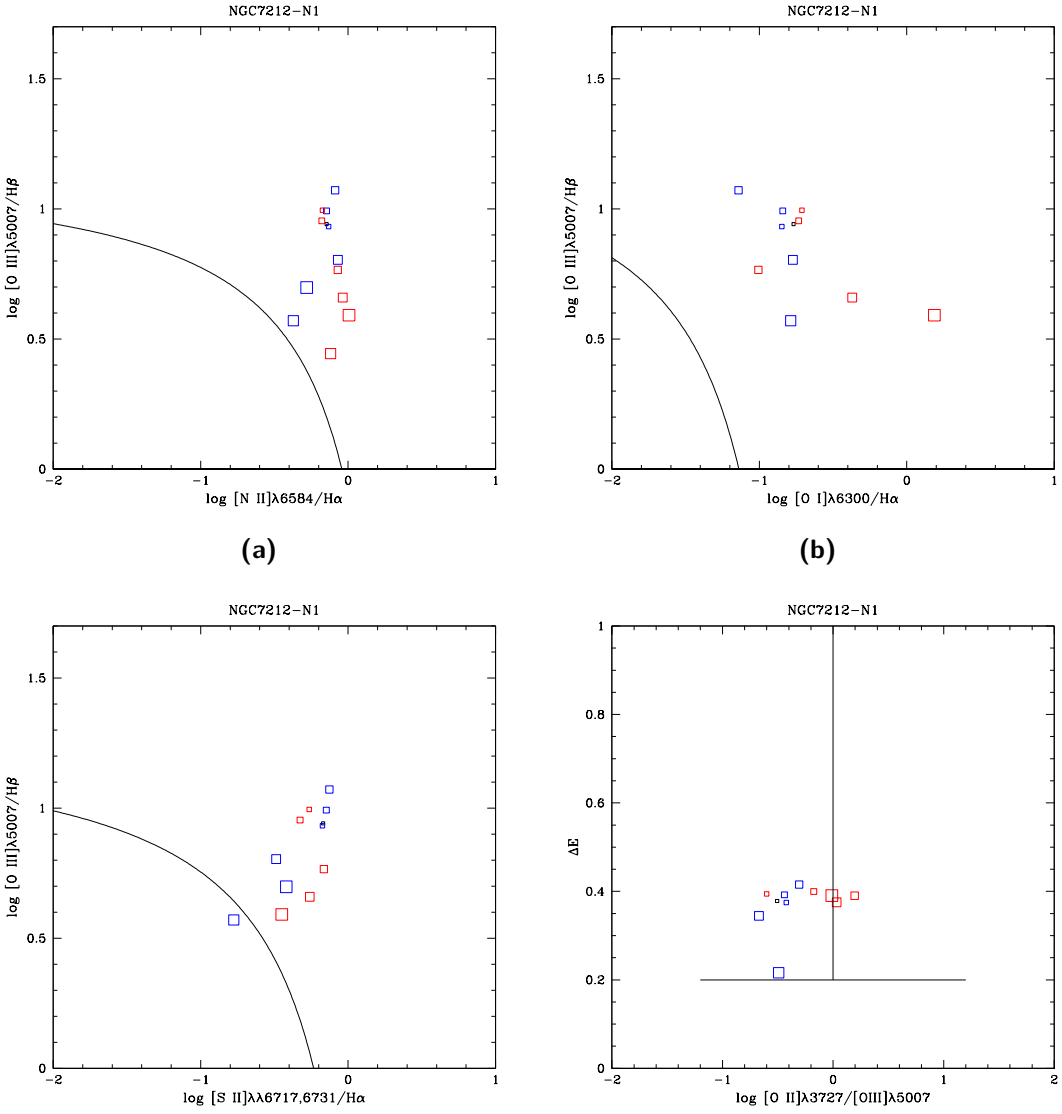

Figure 5.35: (a)[N II]λ6584/Hα vs [O III]λ5007/Hβ (b) [O I]λ6300/Hα vs [O III]λ5007/Hβ (c) [S II]$\lambda\lambda$6717, 6731/Hα vs [O III]λ5007/Hβ diagnostic diagrams for the N1 region of NGC7212. The black lines are the empirical separation between H II regions and other regions from Kewley et al. (2001). (d) ΔE vs [O II]λ3727/[O III]λ5007 diagnostic diagram for the same region. The vertical line divides the power-law ionized regions (on the left) and the shock ionized ones (on the right). The horizontal line divides the H II regions from the others. In all diagrams, red squares represent bins with $v > 0$, blue squares data with $v < 0$ and the black ones are for $v = 0$. Bigger squares correspond to higher velocities.

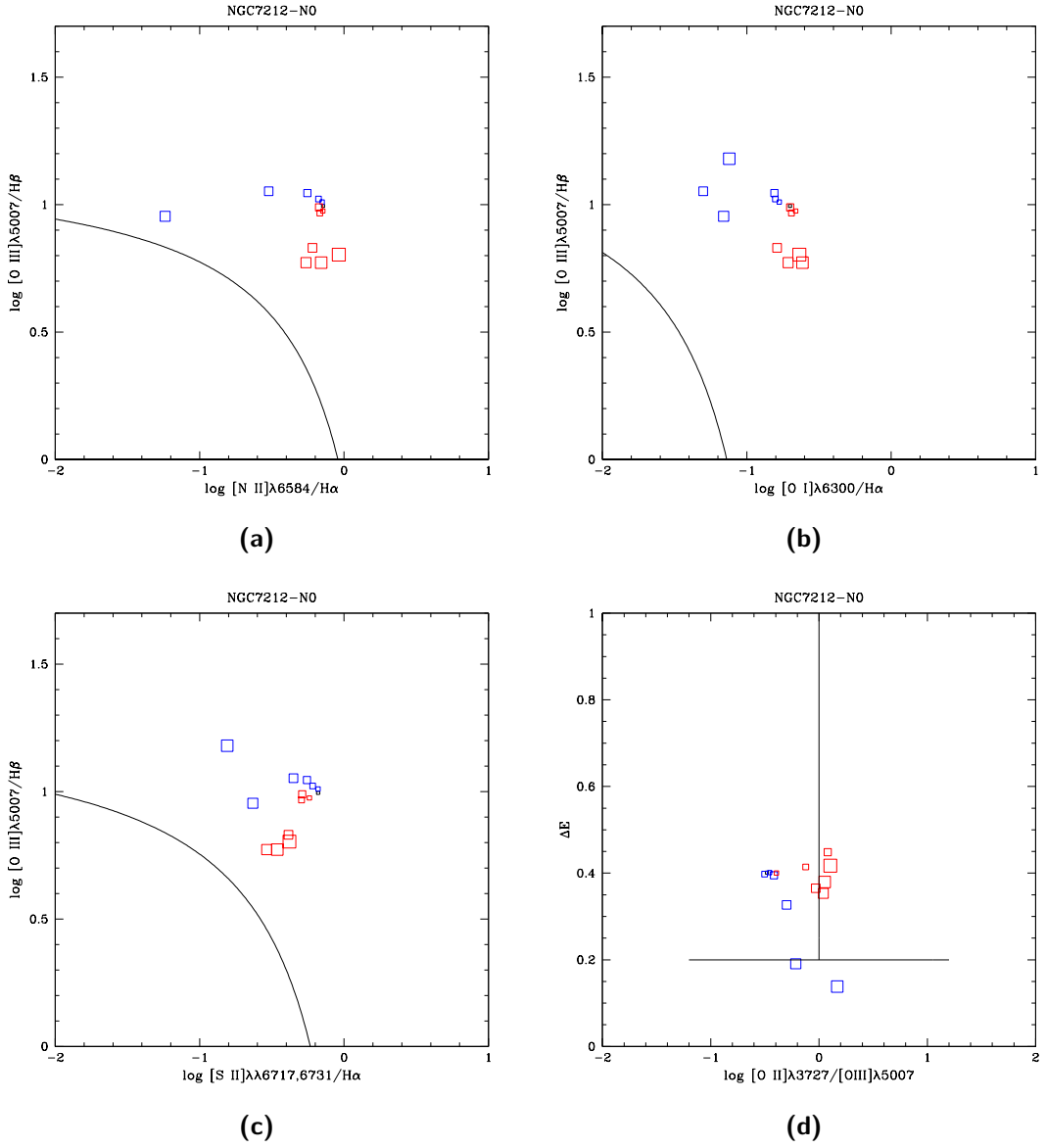

Figure 5.36: (a)[N II]λ6584/Hα vs [O III]λ5007/Hβ (b) [O I]λ6300/Hα vs [O III]λ5007/Hβ (c) [S II]$\lambda\lambda$6717, 6731/Hα vs [O III]λ5007/Hβ diagnostic diagrams for the N0 region of NGC7212. The black lines are the empirical separation between H II regions and other regions from Kewley et al. (2001). (d) ΔE vs [O II]λ3727/[O III]λ5007 diagnostic diagram for the same region. The vertical line divides the power-law ionized regions (on the left) and the shock ionized ones (on the right). The horizontal line divides the H II regions from the others. In all diagrams, red squares represent bins with $v > 0$, blue squares data with $v < 0$ and the black ones are for $v = 0$. Bigger squares correspond to higher velocities.

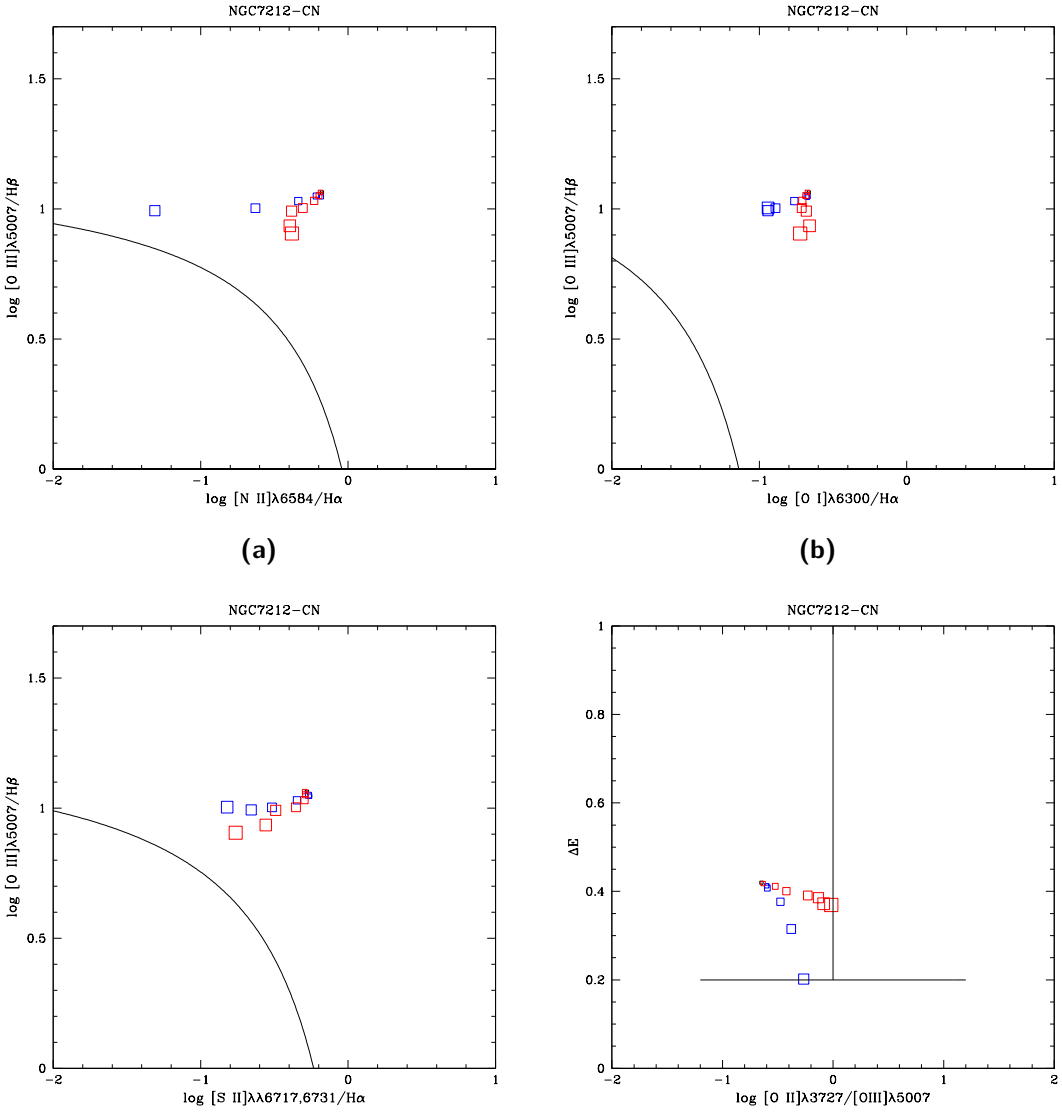

Figure 5.37: (a)[N II]λ6584/Hα vs [O III]λ5007/Hβ (b) [O I]λ6300/Hα vs [O III]λ5007/Hβ (c) [S II]$\lambda\lambda$6717, 6731/Hα vs [O III]λ5007/Hβ diagnostic diagrams for the CN region of NGC7212. The black lines are the empirical separation between H II regions and other regions from Kewley et al. (2001). (d) ΔE vs [O II]λ3727/[O III]λ5007 diagnostic diagram for the same region. The vertical line divides the power-law ionized regions (on the left) and the shock ionized ones (on the right). The horizontal line divides the H II regions from the others. In all diagrams, red squares represent bins with $v > 0$, blue squares data with $v < 0$ and the black ones are for $v = 0$. Bigger squares correspond to higher velocities.

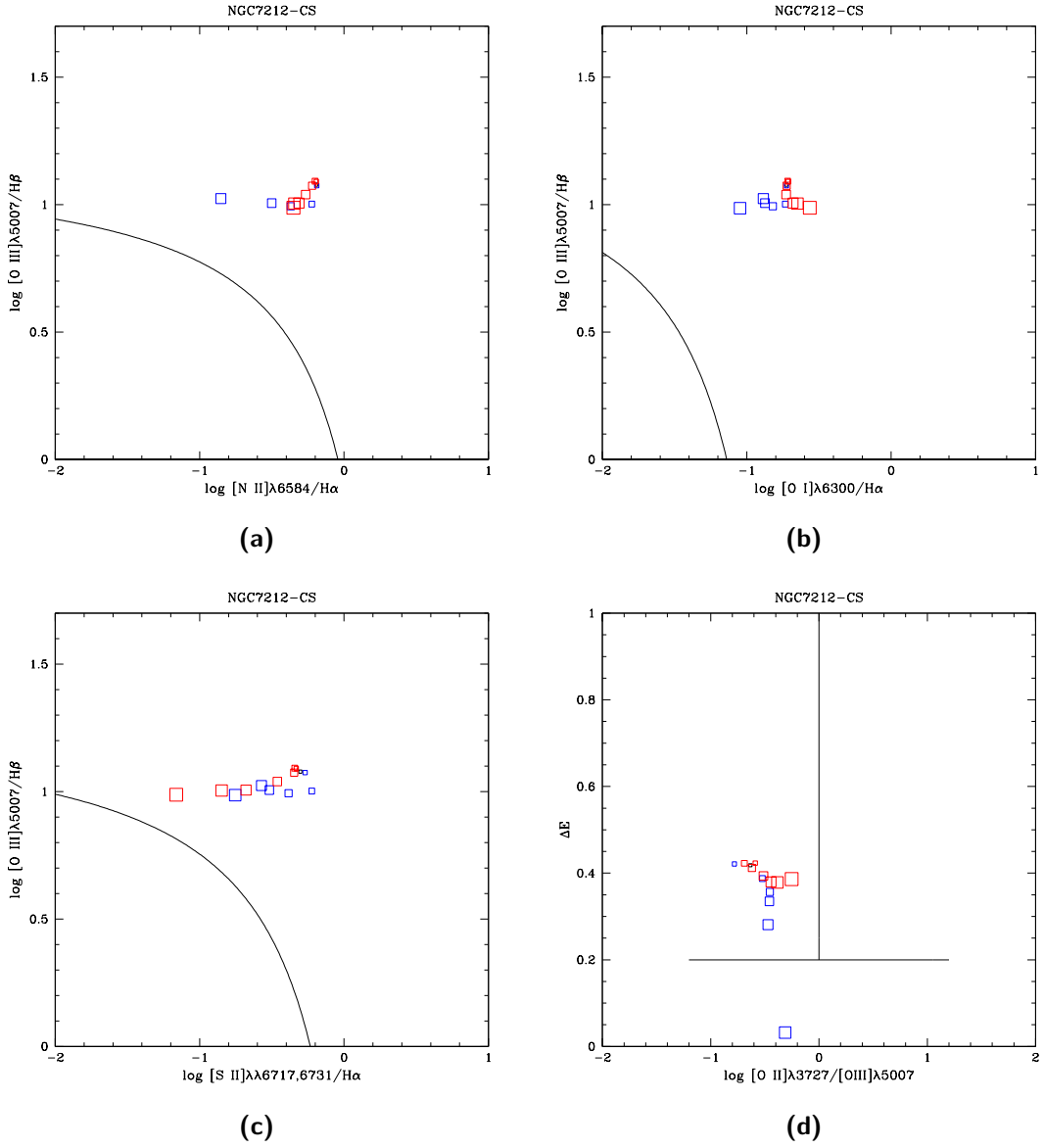

Figure 5.38: (a)[N II]λ6584/Hα vs [O III]λ5007/Hβ (b) [O I]λ6300/Hα vs [O III]λ5007/Hβ (c) [S II]$\lambda\lambda$6717, 6731/Hα vs [O III]λ5007/Hβ diagnostic diagrams for the CN region of NGC7212. The black lines are the empirical separation between H II regions and other regions from Kewley et al. (2001). (d) ΔE vs [O II]λ3727/[O III]λ5007 diagnostic diagram for the same region. The vertical line divides the power-law ionized regions (on the left) and the shock ionized ones (on the right). The horizontal line divides the H II regions from the others. In all diagrams, red squares represent bins with $v > 0$, blue squares data with $v < 0$ and the black ones are for $v = 0$. Bigger squares correspond to higher velocities.

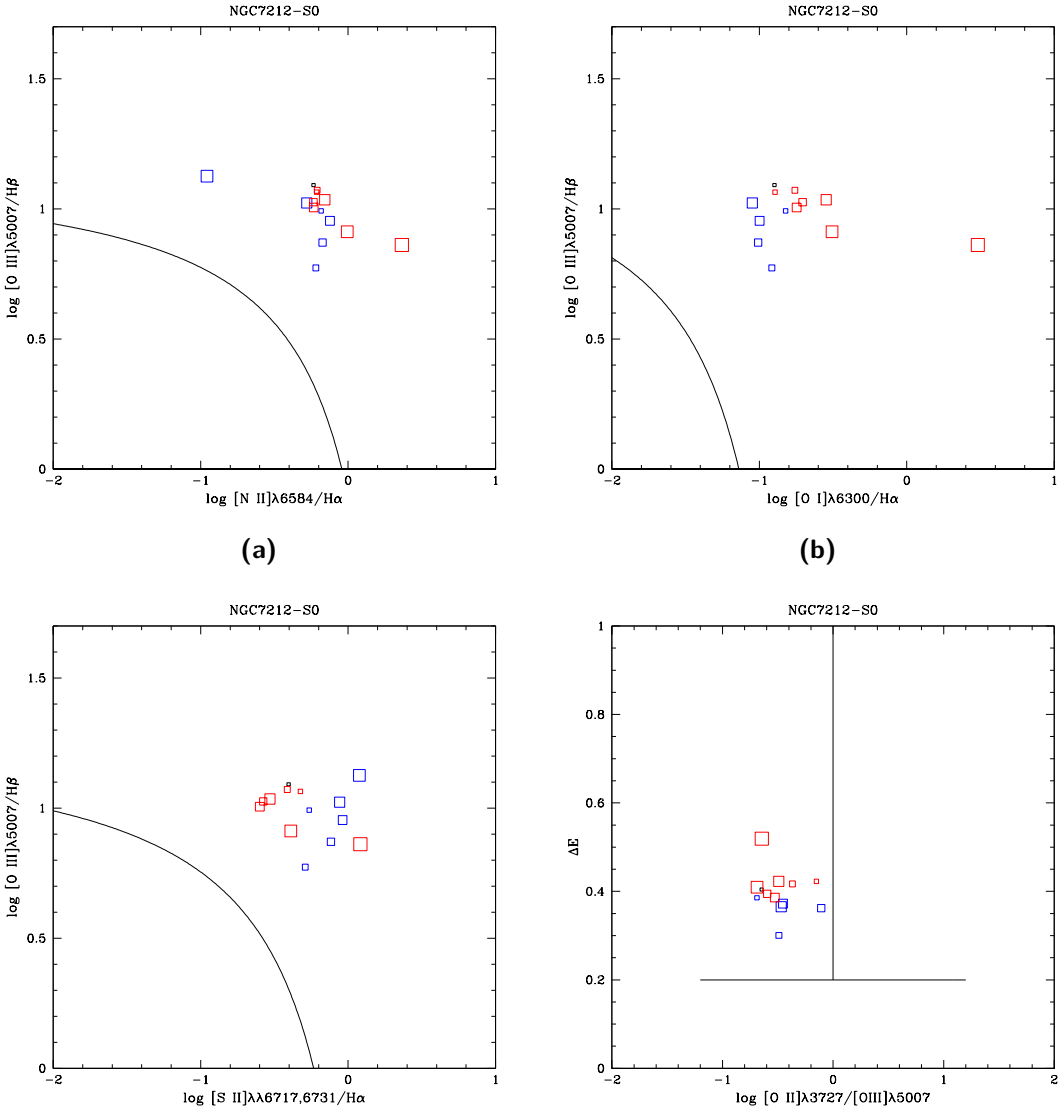

Figure 5.39: (a)[N II]λ6584/Hα vs [O III]λ5007/Hβ (b) [O I]λ6300/Hα vs [O III]λ5007/Hβ (c) [S II]$\lambda\lambda$6717, 6731/Hα vs [O III]λ5007/Hβ diagnostic diagrams for the CN region of NGC7212. The black lines are the empirical separation between H II regions and other regions from Kewley et al. (2001). (d) ΔE vs [O II]λ3727/[O III]λ5007 diagnostic diagram for the same region. The vertical line divides the power-law ionized regions (on the left) and the shock ionized ones (on the right). The horizontal line divides the H II regions from the others. In all diagrams, red squares represent bins with $v > 0$, blue squares data with $v < 0$ and the black ones are for $v = 0$. Bigger squares correspond to higher velocities.

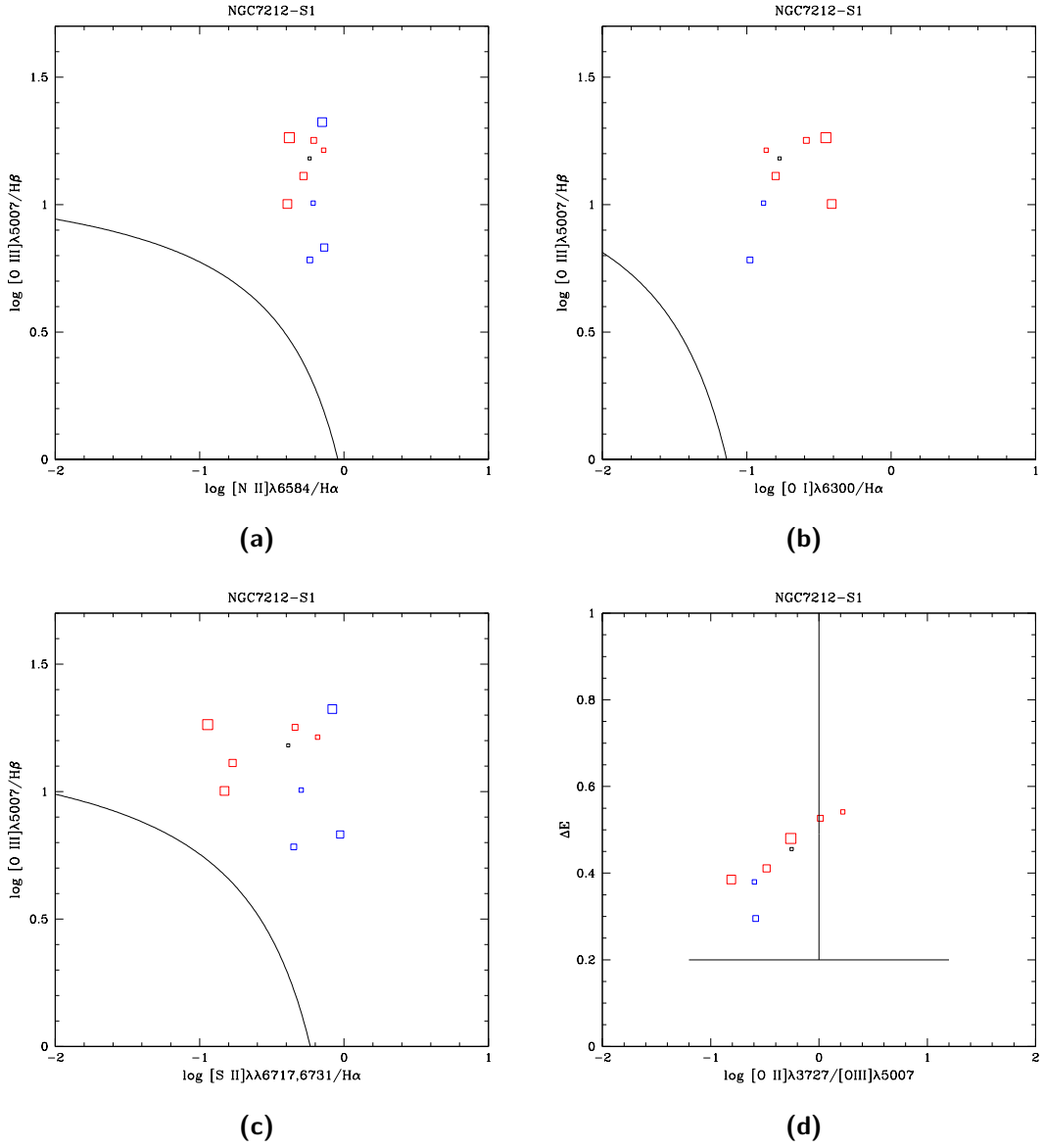

Figure 5.40: (a)[N II]λ6584/Hα vs [O III]λ5007/Hβ (b) [O I]λ6300/Hα vs [O III]λ5007/Hβ (c) [S II]$\lambda\lambda$6717, 6731/Hα vs [O III]λ5007/Hβ diagnostic diagrams for the CN region of NGC7212. The black lines are the empirical separation between H II regions and other regions from Kewley et al. (2001). (d) ΔE vs [O II]λ3727/[O III]λ5007 diagnostic diagram for the same region. The vertical line divides the power-law ionized regions (on the left) and the shock ionized ones (on the right). The horizontal line divides the H II regions from the others. In all diagrams, red squares represent bins with $v > 0$, blue squares data with $v < 0$ and the black ones are for $v = 0$. Bigger squares correspond to higher velocities.

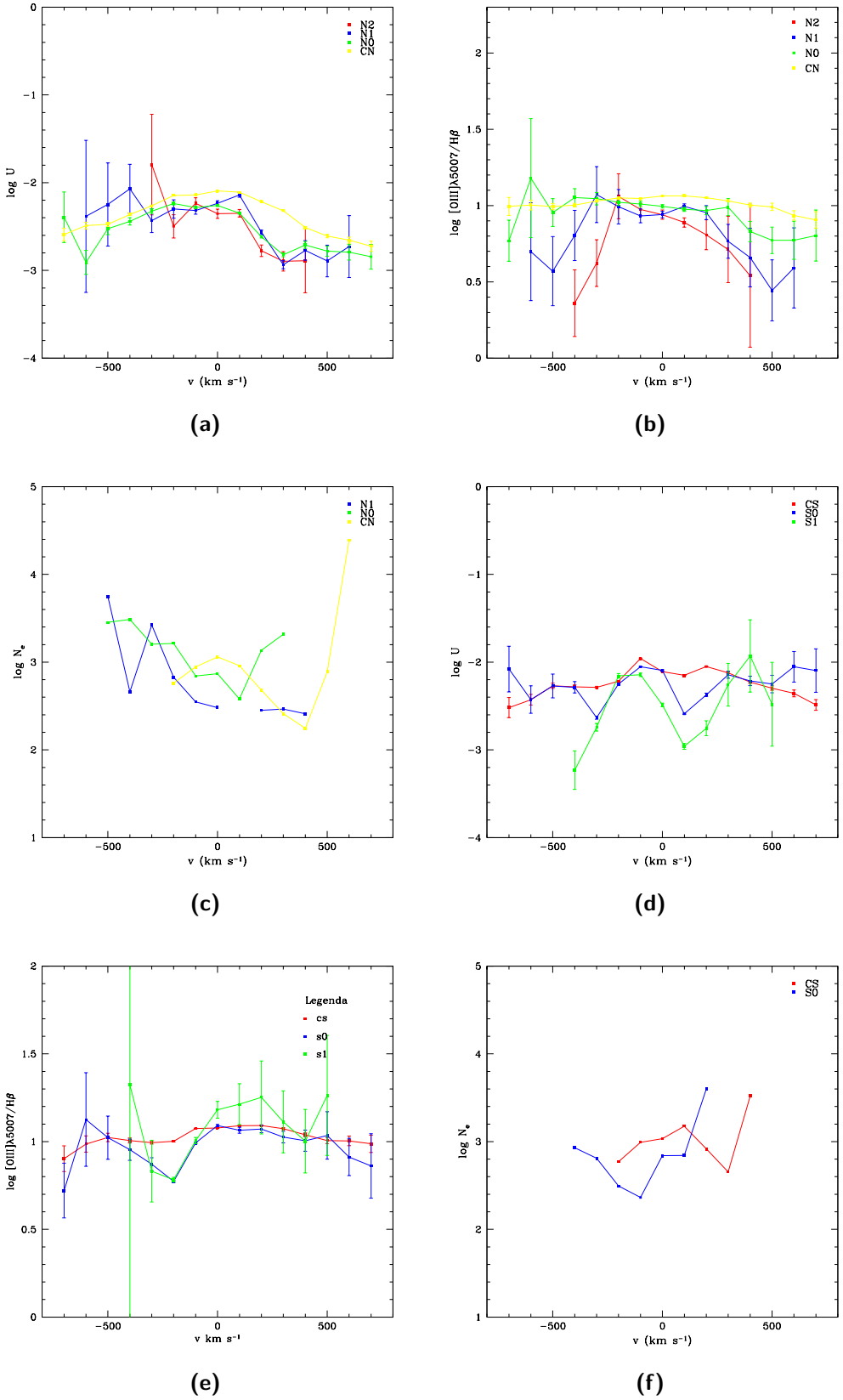

Figure 5.41: U vs v,[O III]λ5007/Hβ vs v and N_e vs v diagrams for the northern regions (in the first three graphics) and southern regions (in the last three).

Also in this galaxy it was difficult to measure temperature and density of the highly ionized gas. The problem was that the [Ar IV] lines are too faint in most of the regions and, if they were clearly present, their ratio was too high to measure the electron density. Looking at the temperatures and densities in Tab. 5.7 it is possible to notice that there are three regions with temperature of about 15000 K, one with T= 12000 K and one, clearly colder, at 9000 K. It must be also noticed that some of the values are very high, about 15000 K, and this could means that the heating process is very efficient in those regions or, on the contrary, than the cooling process is less efficient that in the other galaxies. I also measured some of the densities in the velocity bins with the [S II] doublet. In the southern regions I could measure the density only in the regions nearest to the nucleus and there are not enough measurement to say something about the trend with velocity. It is only possible to notice that there is a high data dispersion. In the northern regions I could measure the electron density in some more regions and velocity bins. The electron density increases for $v < 0\,\mathrm{kms}^{-1}$ in the external region, while I could measure only a small number of density values in CN for the same v. It seems that the general trend of the density is to decrease when the velocity is increasing, but there are not enough data to have a reliable result. A similar behaviour can be seen also for $v > 0\,\mathrm{kms}^{-1}$ but at higher velocity it quickly increases. Also in the N0 region the density increases for $v > 0\,\mathrm{kms}^{-1}$ but without the first drop which can be seen in the central region.

In Fig. 5.42 and 5.43 there are the graphs used to estimate the metallicity of the galaxy. Also here the results are quite complex. In most of the plots the data associated to the low velocity bins are in good agreement with the models and they seem to be located in the section of the diagram between the models with metallicity in the range $1 - 1.5\,\mathrm{Z}_{\odot}$. There is an exception in Fig. 5.43 (c), where not even those points are comparable to the models. In almost all of the other panels, it seems that there is a huge $A(V)$ overestimation. In fact, only the data corresponding to the velocity bins with lowest absorption values are near the models and the main data dispersion is in the [N II]λ6584/[O II]λ3727 direction. For example, in the CN region (Fig. 5.42 (d)) the points are distributed in a vertical line and higher velocity bins have lower values of the [N II]λ6584/[O II]λ3727 ratio. This could mean that there is an overestimation of the absorption value that increases at increasing velocity, in spite of the regular $A(V)$ profile in Fig. 5.33 (a).

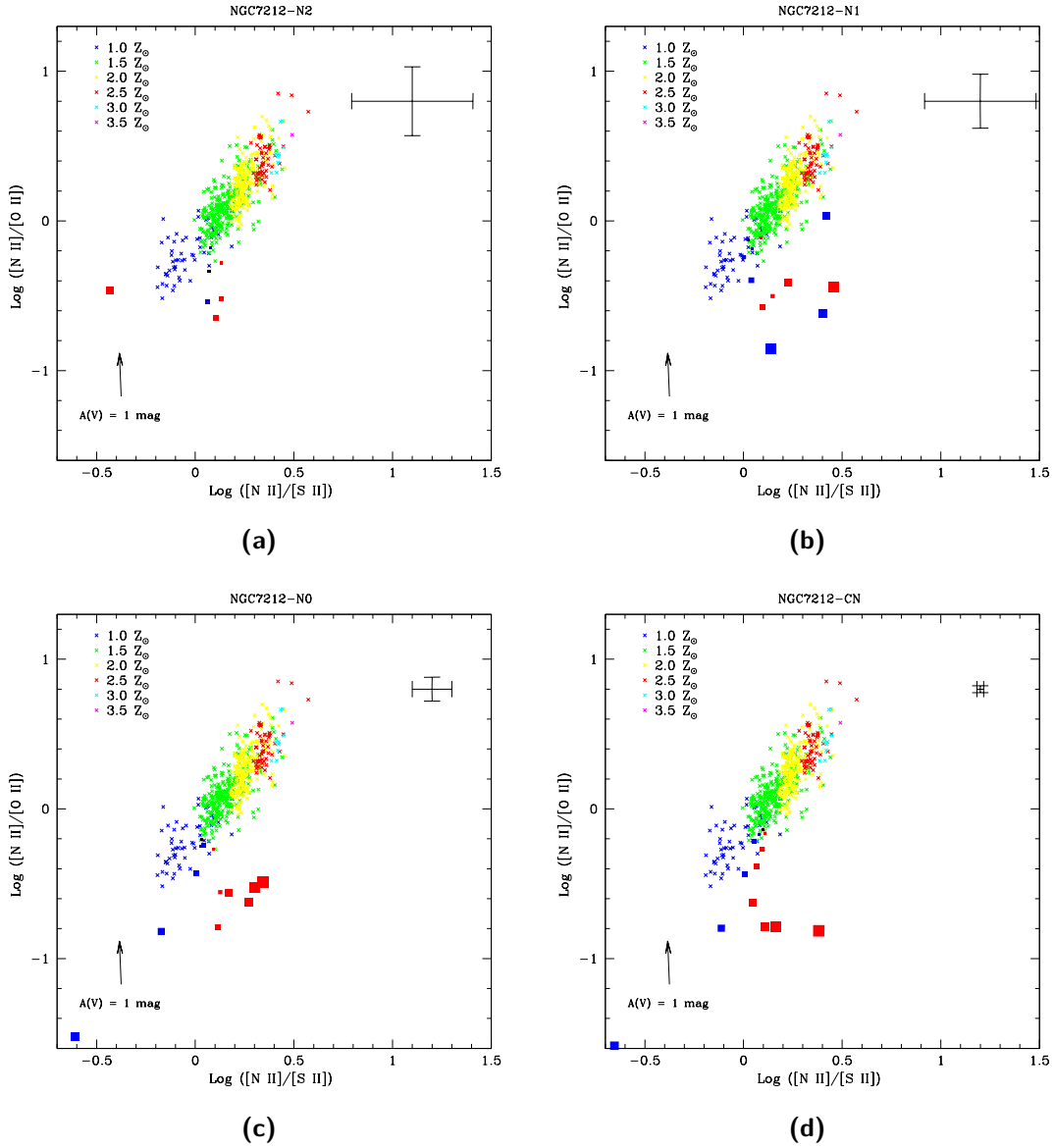

Figure 5.42: [N II]λ6584/[S II]$\lambda\lambda$6717, 6731 vs [N II]λ6584/[O II]λ3727 diagrams of NGC7212 northern regions. The coloured cross are the points from the simulation by Vaona (2010). The red squares are the measurements in the $v > 0\,\mathrm{kms}^{-1}$ bins, the blue squares are the $v < 0$ bins, the black one is the $v = 0$ bin. Bigger squares correspond to higher velocities. The arrow shows the effect of the extinction for $A(V) = 1\,\mathrm{mag}$. The error bars in the up right corner of the diagrams represent the median error of the data.

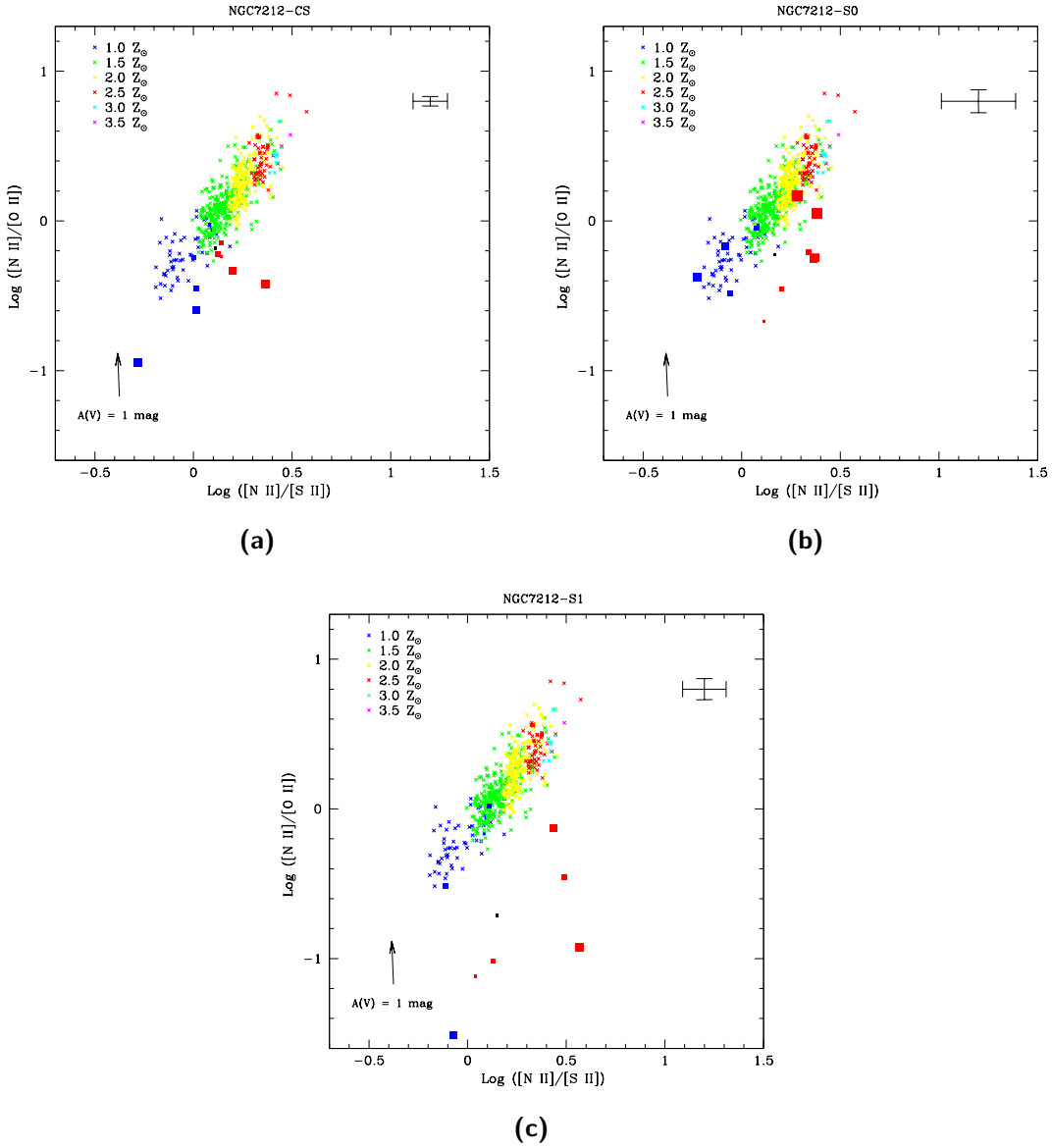

Figure 5.43: [N II]λ6584/[S II]$\lambda\lambda$6717, 6731 vs [N II]λ6584/[O II]λ3727 diagrams of NGC7212 southern regions. The coloured cross are the points from the simulation by Vaona (2010). The red squares are the measurements in the $v > 0\,\mathrm{kms}^{-1}$ bins, the blue squares are the $v < 0$ bins, the black one is the $v = 0$ bin. Bigger squares correspond to higher velocities. The arrow shows the effect of the extinction for $A(V) = 1$ mag. The error bars in the up right corner of the diagrams represent the median error of the data.

Conclusions

The aim of this work is to study the physical properties of the ENLR of nearby AGN as a function of velocity. With this kind of study, it is, in principle, possible to use the velocity to distinguish the emission coming from structures that are not spatially resolved. The main questions to answer are two: do these structures have different properties as a function of velocity? If radial motions are observed in the gas, which mechanism drives those motions? Radiation pressure from the center or gravitational attraction from outside?

In order to perform the analysis, I divided each emission line in velocity bins with constant width and I used the flux measurements inside these bins to calculate line ratios. By means of these ratios it was possible to measure temperature, density and ionization parameter as a function of velocity, to investigate the ionization mechanism of the gas in each velocity bin, and also to compare the data to theoretical ratios, in order to measure the metallicity of the gas. This method is a combination of those developed by Ozaki (2009) and Bisigello (2012). Ozaki's method consists in dividing the profile of some emission lines (Hβ, [O III]$\lambda\lambda$5007, 4959, [O I]λ6300, [Fe VII]λ6087) in velocity bins, and then studing their fluxes. The Bisigello's one consists in trying to separate the components by fitting every single emission lines ([O II]λ3727, [O III]λ4363, Hβ, [O III]$\lambda\lambda$4959, 5007, [O I]λ6300,[O I]λ6363, [N II]$\lambda\lambda$6548, 6584, [S II]$\lambda\lambda$6717, 6731) with the same number of Gaussians, in order to measure quantities like temperature and density from emission line ratios, assuming that each Gaussian represent the same component in each measured line.

In this work, I studied three nearby Seyfert 2 galaxies with known ionization cones: IC5063, NGC5643 and NGC7212. In order to resolve the principal features of the lines profiles, I needed spectra with medium resolution (R $\sim$ 10000). In particular, I used data acquired with MagE, the echelle spectrograph of the Magellan telescopes, which has a maximum resolution R $\simeq$ 8000.

I reduced the data with the following steps: bias subtraction, order extraction, wavelenght calibration, flat-field correction, sky subtraction, flux calibration and exposure combination. I wanted to analyse different regions of the galaxies separately, so I needed to extract the one-dimensional (1D) spectrum of each region. Then, to be sure that the extracted 1D spectrum of a region contained all and only the emission of that region, I straighten and aligned the spectra before the extraction. In order to better measure the fluxes, I fitted and subtracted the stellar continuum from the spectra, by means of STARLIGHT. Some important emission lines were blended together: Hα and the [N II]$\lambda\lambda$6548, 6584 doublet, the [S II]$\lambda\lambda$6717, 6731 doublet. Since sometimes these lines were severely blended, I had to develop and apply a special procedure to recover the profile of eah single component.

There are several advantages in using this method. The first one is that, using a medium resolution echelle spectrograph like MagE, it is possible to acquire the whole optical spectral range in a single observation and in a fair amount of time, while high resolution echelle spectrographs require longer exposure times and classical long slit spectrographs require multiple observations, in order to cover the complete spectral range. However, such a resolution is enough to highlight the profile features due to kinematically complex structures. Moreover it is possible to observe radial motions, superimposed to turbulent motions, confirming that the ENLR is composed by gas clouds with different kinematical properties. To divide the emission lines in fixed velocity bins is, also, a less arbitrary way to study the lines profiles than fitting them with Gaussian functions.

Nevertheless, there are also some limitations. The main problem is that spectra with high S/N ratios are needed, especially in the lines wings and in the weak lines, like [O III]λ4363, in order to divide them in velocity bins and measure quantities like temperature and density inside them, and this means long exposure times, also with large telescopes, because of the resolution. In addiction, the lines are intrinsecally broad, therefore increasing the resolution is not useful (R> 10000 means to have velocity resolution smaller than the thermal Doppler broadening). A big limitation is that the blended lines cause a loss of information in the lines wings (the high velocity bins). This has a serious consequence on the Hα/Hβ ratio, and so on the estimate of dust extinction, which alters the ratios between distant lines.

Now I summarize some important results obtained in this work. I found that the main ionization mechanism of the gas, in most cases, is the photoionization by a power-law continuum, which means that the clouds are directly ionized by the AGN. However, in some cases, it seems that shock-waves are important in ionizing the gas, as in the S1 region of IC5063 (see Fig. 5.11 (d)). This region is peculiar also because it shows a certain dependence of the [O II]λ3727/[O III]λ5007 diagnostic ratio on the velocity. In general, the diagnostic ratios do not seem to depend on the velocity. In NGC5643, I found, by means of the diagnostic diagrams, that the AGN is the main ionizing radiation source in both sides of the galaxy nucleus, proving the existance of two ionization cones, while Simpson et al. (1997) observed a single cone on the east side of the nucleus.

I also found that, in general, the gas density tends to increase when $|v|$ increases, the northern region of IC5063 in Fig. 5.13 (c) is an example. However, in few cases like in some regions of NGC5643 (see Fig. 5.27 (c)) N_e tends to decrease with $|v|$. In fact, in these regions, there are too few data to have a reliable information about the real N_e behaviour.

The ionization parameter U is not costant as it is possible to see in Fig. 5.13 (a) (d), 5.27 (a) (d) and 5.41 (a) (d), but it often depends on v. However, this happens almost always when N_e depend on v, because U is proportional to N_e^{-1} (see eq. 4.11).

I could not calculate temperature and density of the gas in all of the velocity bins, because the needed lines were too weak. Therefore, I measured the average temperature and density of the highly ionized and the lowly ionized gas in all of the regions where I could detect the lines. Only the [S II]$\lambda\lambda$6717, 6731 doublet was strong enough to be divided in velocity bins and it was possible to measure the density of the lowly ionized gas as a function of velocity. However, it is possible to see in Fig. 5.13 (c) (f), 5.27 (c) (f) and 5.41 (c) (f), that in many cases I could not measure the density, because the

deblending process altered the value of the [S II] ratio.

Finally I compared some observed ratios to models which allow to estimate the metallicity value of the gas. In IC5063 and NGC7212 (Fig. 5.14, 5.15, 5.42, 5.43) the data corresponding to the low velocity bins show values of metallicity from 1.0 to 1.5 $Z_{\odot}$, while in NGC5643 (Fig. 5.28, 5.29) the metallicity values are between 1.5 and 2.5 $Z_{\odot}$. On the other hand, lines ratios corresponding to high velocity clouds, do not agree with models, maybe because of the extinction correction or of the presence of shock-waves.

Possible future developments of this work consist in observing new objects with known ENLR, acquiring their spectra with the highest possible S/N ratio, in order to improve the analysis on the wings of the bright emission lines and on the weak lines and to develop new photoionization and shock models in order to compare them to data from observation.

Bibliography

A. Kramida et al. (2014). NIST Atomic Spectra Database (ver. 5.2), [Online]. Available: `http://physics.nist.gov/asd` [2015, September 12]. National Institute of Standards and Technology, Gaithersburg, MD.

Antonucci, R. (1993). "Unified models for active galactic nuclei and quasars". In: ARA&A 31, pp. 473–521.

Antonucci, R. R. J. and J. S. Miller (1985). "Spectropolarimetry and the nature of NGC 1068". In: ApJ 297, pp. 621–632.

Baldwin, J. A., M. M. Phillips, and R. Terlevich (1981). "Classification parameters for the emission-line spectra of extragalactic objects". In: PASP 93, pp. 5–19.

Baldwin, J. A., A. S. Wilson, and M. Whittle (1987). "Kinematics and ionization of extended gas in active galaxies. III - The extranuclear properties of NGC 1068". In: ApJ 319, pp. 84–104.

Beckmann, V. and C. R. Shrader (2012). *Active Galactic Nuclei*.

Bicknell, G. V. et al. (1998). "Are Seyfert Narrow-Line Regions Powered by Radio Jets?" In: ApJ 495, pp. 680–690.

Bisigello, L. (2012). "Proprietà Fisiche e Cinematiche della Narrow Line Region in NGC7212". Msc thesis. Università di Padova, Dipartimento di Fisica e Astronomia Galileo Galilei.

Bochanski, J. J. et al. (2009). "MASE: A New Data-Reduction Pipeline for the Magellan Echellette Spectrograph". In: PASP 121, pp. 1409–1418.

Capetti, A. et al. (1995). "The Morphology of the Narrow-Line Region of Markarian 3". In: ApJ 448, p. 600.

Cardelli, J. A., G. C. Clayton, and J. S. Mathis (1989). "The relationship between infrared, optical, and ultraviolet extinction". In: ApJ 345, pp. 245–256.

Cid Fernandes, R. et al. (2005). "Semi-empirical analysis of Sloan Digital Sky Survey galaxies - I. Spectral synthesis method". In: MNRAS 358, pp. 363–378.

Cid Fernandes, R. et al. (2007). "Uncovering the chemical enrichment and mass-assembly histories of star-forming galaxies". In: MNRAS 375, pp. L16–L20.

Ciroi, S. et al. (2003). "2-D spectroscopy and modeling of the biconical ionized gas in NGC 4388". In: A&A 400, pp. 859–870.

Ciroi, S. et al. (2005). "New photometric and spectroscopic observations of the Seyfert galaxy Mrk 315". In: MNRAS 360, pp. 253–271.

Colina, L., W. B. Sparks, and F. Macchetto (1991). "IC 5063 - A merger remnant with a hidden luminous active nucleus". In: ApJ 370, pp. 102–117.

Cracco, V. et al. (2011). "The origin of gas in extended narrow-line regions of nearby Seyfert galaxies - I. NGC 7212". In: MNRAS 418, pp. 2630–2641.

De Robertis, M. M., R. J. Dufour, and R. W. Hunt (1987). "A five-level program for ions of astrophysical interest". In: JRASC 81, pp. 195–220.

Di Mille, F. (2007). "Spectrophotometric Study of the Central Regions inSeyfert Galaxies with 3D Spectroscopy". PhD thesis. Università di Padova, Dipartimento di Fisica e Astronomia Galileo Galilei.

ESO standard stars catalogue (2015). URL: `http://www.eso.org/sci/observing/tools/standards/spectra/hr5501.html`.

Evans, I. N. et al. (1993). "Hubble Space Telescope Imaging of the Narrow-Line Region of NGC 4151". In: ApJ 417, p. 82.

Falcke, H., A. S. Wilson, and C. Simpson (1998). "Hubble Space Telescope and VLA Observations of Seyfert 2 Galaxies: The Relationship between Radio Ejecta and the Narrow-Line Region". In: ApJ 502, pp. 199–217.

Ferland, G. J. et al. (2013). "The 2013 Release of Cloudy". In: Rev. Mexicana Astron. Astrofis. 49, pp. 137–163.

Fu, H. and A. Stockton (2007). "Integral Field Spectroscopy of the Extended Emission-Line Region of 4C 37.43". In: ApJ 666, pp. 794–805.

Groves, B. A., T. M. Heckman, and G. Kauffmann (2006). "Emission-line diagnostics of low-metallicity active galactic nuclei". In: MNRAS 371, pp. 1559–1569.

Harrison, B. et al. (1986). "The parsec-scale structure of the radio nucleus of NGC 4151". In: MNRAS 218, pp. 775–784.

Heckman, T. M. (1980). "An optical and radio survey of the nuclei of bright galaxies - Activity in normal galactic nuclei". In: A&A 87, pp. 152–164.

Ho, L. C., A. V. Filippenko, and W. L. W. Sargent (1997). "A Search for "Dwarf" Seyfert Nuclei. V. Demographics of Nuclear Activity in Nearby Galaxies". In: ApJ 487, pp. 568–578.

Hough, J. H. et al. (1987). "Infrared and optical polarimetry of the radio elliptical IC 5063 (PKS2048-57) - Discovery of a highly polarized non-thermal nucleus". In: MNRAS 224, pp. 1013–1018.

Inglis, M. D. et al. (1993). "Evidence for an Obscured Broadline Region in the Early Type Radio Galaxy IC5063". In: MNRAS 263, p. 895.

Kellermann, K. I. et al. (1989). "VLA observations of objects in the Palomar Bright Quasar Survey". In: AJ 98, pp. 1195–1207.

Kewley, L. J. et al. (2001). "Theoretical Modeling of Starburst Galaxies". In: ApJ 556, pp. 121–140.

Komossa, S. and H. Schulz (1997). "Interpretation of the emission line spectra of Seyfert 2 galaxies by multi-component photoionization models." In: A&A 323, pp. 31–46.

Marshall, J. L. et al. (2008). "The MagE spectrograph". In: Society of Photo-Optical Instrumentation Engineers (SPIE) Conference Series 7014, 701454, p. 54.

Mateus, A. et al. (2006). "Semi-empirical analysis of Sloan Digital Sky Survey galaxies - II. The bimodality of the galaxy population revisited". In: MNRAS 370, pp. 721–737.

Morganti, R. et al. (2007). "IC 5063: AGN driven outflow of warm and cold gas". In: A&A 476, pp. 735–743.

Morris, S. et al. (1985). "The velocity fields and radio structures of the active galaxies NGC 5643 and NGC 7582". In: MNRAS 216, pp. 193–217.

Morse, J. A. et al. (1998). "Inclined Gas Disks in the Lenticular Seyfert Galaxy NGC 5252". In: ApJ 505, pp. 159–173.

Mulchaey, J. S., A. S. Wilson, and Z. Tsvetanov (1996). "An Emission-Line Imaging Survey of Early-Type Seyfert Galaxies. II. Implications for Unified Schemes". In: ApJ 467, p. 197.

Muñoz Marı/n, V. M. et al. (2007). "An Atlas of the Circumnuclear Regions of 75 Seyfert Galaxies in the Near-Ultraviolet with the Hubble Space Telescope Advanced Camera for Surveys". In: AJ 134, pp. 648–667.

Osterbrock, D.E. and G.J. Ferland (2006). *Astrophysics of Gaseous Nebulae and Active Galactic Nuclei*. University Science Books. ISBN: 9781891389344. URL: `https://books.google.it/books?id=HgfrkDjBD98C`.

Ozaki, S. (2009). "Kinematic and Excitation Structure of the NGC 1068 Narrow-Line Region". In: PASJ 61, pp. 259–.

Penston, M. V. et al. (1990). "The extended narrow line region of NGC 4151. I - Emission line ratios and their implications". In: A&A 236, pp. 53–62.

Schirmer, M. et al. (2013). "A Sample of Seyfert-2 Galaxies with Ultraluminous Galaxy-wide Narrow-line Regions: Quasar Light Echoes?" In: ApJ 763, 60, p. 60.

Schlafly, E. F. and D. P. Finkbeiner (2011). "Measuring Reddening with Sloan Digital Sky Survey Stellar Spectra and Recalibrating SFD". In: ApJ 737, 103, p. 103.

Schlegel, D. J., D. P. Finkbeiner, and M. Davis (1998). "Maps of Dust Infrared Emission for Use in Estimation of Reddening and Cosmic Microwave Background Radiation Foregrounds". In: ApJ 500, pp. 525–553.

Schmitt, H. R., T. Storchi-Bergmann, and J. A. Baldwin (1994). "Anisotropic high-excitation emission and chemical abundances in the Seyfert 2 galaxy NGC 5643". In: ApJ 423, pp. 237–247.

Schmitt, H. R. et al. (2003). "A Hubble Space Telescope Survey of Extended [O III] λ5007 Å Emission in a Far-Infrared-Selected Sample of Seyfert Galaxies: Results". In: ApJ 597, pp. 768–779.

Shaw, R. A. and R. J. Dufour (1995). "Software for the Analysis of Emission Line Nebulae". In: PASP 107, p. 896.

Simpson, C. et al. (1997). "A One-sided Ionization Cone in the Seyfert 2 Galaxy NGC 5643". In: ApJ 474, pp. 121–128.

Smirnova, A. A. et al. (2007). "The gas kinematics in the Mrk 533 nucleus and circumnuclear region: a gaseous outflow". In: MNRAS 377, pp. 480–490.

Storchi Bergmann, T. and M. G. Pastoriza (1989). "On the metal abundance of low-activity galactic nuclei". In: ApJ 347, pp. 195–200.

Storchi-Bergmann, T. and M. G. Pastoriza (1990). "On the sulfur and nitrogen abundances in the nucleus of Seyfert 2 and LINER galaxies". In: PASP 102, pp. 1359–1365.

Tadhunter, C. and Z. Tsvetanov (1989). "Anisotropic ionizing radiation in NGC5252". In: Nature 341, pp. 422–424.

Tadhunter, C. et al. (2014). "Jet acceleration of the fast molecular outflows in the Seyfert galaxy IC 5063". In: Nature 511, pp. 440–443.

Tran, H. D. (1995). "The Nature of Seyfert 2 Galaxies with Obscured Broad-Line Regions. II. Individual Objects". In: ApJ 440, p. 578.

Unger, S. W. et al. (1987). "The extended narrow-line region in radio Seyferts - Evidence for a collimated nuclear UV field?" In: MNRAS 228, pp. 671–679.

Vaona, L. (2010). “Spectral Properties and Photoionization Models of the NLR in Seyfert Galaxies”. PhD thesis. Università di Padova, Dipartimento di Fisica e Astronomia Galileo Galilei.

Veilleux, S., J. Bland-Hawthorn, and G. Cecil (1999). “A Kinematic Link Between Boxy Bulges, Stellar Bars, and Nuclear Activity in NGC 3079 and NGC 4388”. In: AJ 118, pp. 2108–2122.

Veilleux, S. and D. E. Osterbrock (1987). “Spectral classification of emission-line galaxies”. In: *NASA Conference Publication*. Ed. by C. J. Lonsdale Persson. Vol. 2466. NASA Conference Publication, pp. 737–740.

Wasilewski, A. J. (1981). “A new Seyfert galaxy with asymmetric forbidden-line profiles in an interacting system”. In: PASP 93, pp. 560–563.

Whittle, M. (1985). “The narrow line region of active galaxies. I - Nuclear forbidden line profiles. II - Relations between forbidden line profile shape and other properties”. In: MNRAS 213, pp. 1–31.

— (1992). “Virial and Jet-induced Velocities in Seyfert Galaxies. III. Galaxy Luminosity as Virial Parameter”. In: ApJ 387, p. 121.

Wilson, A. S. (1988). “Star formation and nuclear activity in Seyfert galaxies”. In: A&A 206, pp. 41–16.

Wilson, A. S. and Z. I. Tsvetanov (1994). “Ionization cones and radio ejecta in active galaxies”. In: AJ 107, pp. 1227–1234.

Wilson, A. S. and A. G. Willis (1980). “Radio structures of Seyfert galaxies. I”. In: ApJ 240, pp. 429–441.

Ringraziamenti

Per primi vorrei ringraziare i miei genitori, i miei zii e i miei cugini che mi hanno supportato durante questi anni di studio. Vorrei anche ringraziare Silvia, Marta, Bianca, Chiara e Marco per l'aiuto che mi hanno dato nella preparazione e nella scrittura di questo lavoro. Un grazie va anche a tutti i miei amici che mi hanno sopportato, nonostante tutto, in questi cinque lunghi anni. Ultimi, ma non per importanza, vorrei ringraziare il mio relatore e la mia relatrice che, oltre ad avermi seguito durante tutto il lavoro, mi hanno anche ospitato nel loro ufficio in seguito alla perdita del mio computer.